Physical processes leading to export of fixed carbon out of the surface ocean

Thesis by
Zachary K Erickson

In Partial Fulfillment of the Requirements for the
Degree of
Doctor of Philosophy

CALIFORNIA INSTITUTE OF TECHNOLOGY
Pasadena, California

2019
Defended 29 May 2019

Zachary K Erickson
ORCID: 0000-0002-9936-9881

Two roads diverged in a yellow wood
And sorry that I could not travel both
And be one traveler, long I stood
And looked down one as far as I could
To where it bent in the undergrowth.

Robert Frost, 1916

ACKNOWLEDGEMENTS

Thanks to Kim and Kevin Erickson, my parents, for supporting me at all stages of my life's journey, believing in me at every step of the way, and encouraging me to pursue opportunities that would help me grow;

To Andy Thompson, my Ph.D. advisor, for his excitement and passion for science, his unwavering support of my development as a scientist throughout the past six years, his encouragement of my taking on research projects not directly related to my thesis, his willingness to take on projects that stretched his own area of expertise, his thoughtful advice on a variety of topics throughout my graduate school tenure, and for always treating me as a scientific collaborator;

To Giuliana Viglione, for being a constant sounding board, for helping me tell more cohesive and coherent stories, and for always encouraging me to expand my boundaries;

To Xiaozhou Ruan, for always being willing to help me through fluid dynamics problems and for being a constant supportive presence throughout our time in the Thompson group;

To the entire Thompson group at Caltech, past and present, for a welcoming and invigorating research atmosphere;

To Jess Adkins, for chairing my thesis advisory committee and for first introducing me to oceanography, and especially for showing me how exciting and interconnected all of the different sciences are when applied to the oceans;

To Christian Frankenberg, for being a member of my thesis advisory committee and for spending so much time helping me understand remote sensing and inverse modeling;

To Michelle Gierach, for being a member of my thesis advisory committee and inviting me up to JPL on numerous occasions to give seminars or to talk about ongoing research projects;

To Nicolas Cassar, for helping me to understand biological oceanography concepts and feel like I could make a contribution to the field;

To Kevin Arrigo, for taking me on my first research cruise and treating me like an independent scientist from the very beginning;

To Janet Sprintall, and everyone on the NBP14-09 and LMG14-11 cruises, for making research vessels feel like home;

To all of my co-authors — Andy Thompson, David Thompson, Christian Frankenberg, Michelle Gierach, Nicolas Cassar, Kevin Arrigo, Jörn Callies, Patrice Klein, Xiaolong Yu, Matt Mazloff, Janet Sprintall, and Alberto Naveira Garabato — for putting some of themselves into my scientific writing;

To Hannah Allen, for always being willing to give helpful advice or support me during rough patches along the way;

To the many people, and especially Mara Freilich and Erin Dillon, whose infectious enthusiasm about science has helped me throughout; and

To Hannah Joy-Warren, Ivona Cetinić, Anna Ho, Hall Daily, Dave Siegel, and the many other people who gave me encouragement along the way.

ABSTRACT

The ocean sequesters carbon on long time scales by depositing it deep in the ocean, where it is no longer in contact with the atmosphere. This sequestration is also termed "carbon export", and is accomplished via a vertical flux of carbon into the interior of the ocean. Marine photosynthesis by phytoplankton, which consume carbon dioxide dissolved in the surface ocean and are transported to depth to be eventually remineralized or form sediments at the ocean surface, is a key component of this flux (the biological pump). This mechanism is primarily thought to occur via sinking of particulates. However, research over the past few decades has highlighted the role of instabilities at the "submesoscale", or 0.1–20 km, to induce large, $O(100\text{ m day}^{-1})$ vertical velocities in the ocean. These vertical velocities can potentially subduct carbon from the surface ocean into the interior, where it would contribute to export. Observations of the ocean are, however, rarely made at scales which would detect these submesoscale instabilities. In this thesis, I use *in situ* observations from autonomous underwater vehicles, Seagliders, which make measurements in the upper 1000 m of the water column at horizontal scales of 1–3 km, to understand when and where submesoscale instabilities are present, and the extent to which they act to transport biologically fixed carbon out of the surface ocean. Three different types of instabilities are active in the surface mixed layer: baroclinic, gravitational, and symmetric. Each of these has potential to subduct material below the mixed layer; however, these instabilities are generally strongest during the winter, when biological production is at its minimum. An interesting exception is in southern Drake Passage, where interactions between the intense frontal system and the continental shelf result in subduction of water masses off the continental shelf during summer, when phytoplankton are photosynthesizing. In general, however, carbon export via submesoscale instabilities is expected to be largest during spring, when phytoplankton become more productive but conditions can still be ripe for submesoscale subduction. Scaling up these observations to the global ocean system is difficult because *in situ* observations at submesoscales are sparse. This thesis explores the ability of surface flux measurements, from reanalysis products and remote sensing measurements, to accurately depict carbon export via subduction processes by modeling the water profile in a one-dimensional model following Lagrangian floats in the ocean. This approach holds promise to advance the ultimate goal of determining the global effect of submesoscale-driven carbon export.

PUBLISHED CONTENT AND CONTRIBUTIONS

Erickson, ZK, AF Thompson, J Callies, X Yu, A Naveira Garabato, and P Klein (in review). "The vertical structure of open-ocean submesoscale variability during a full seasonal cycle". In: *Journal Phys. Oceanogr.*
Z.K.E. conceived the project, analyzed the data, and wrote the manuscript.

Thompson, DR et al. (in press). "A unified approach to estimate land and water reflectances with uncertainties for coastal imaging spectroscopy". In: *Rem. Sens. Environ.*
Z.K.E. assisted in the analysis.

Erickson, ZK, C Frankenberg, DR Thompson, AF Thompson, and M Gierach (2019). "Remote Sensing of Chlorophyll Fluorescence in the Ocean Using Imaging Spectrometry: Toward a Vertical Profile of Fluorescence". In: *Geophysical Research Letters* 46.3, pp. 1571–1579. DOI: 10.1029/2018GL081273.
Z.K.E. assisted in writing the proposal for this research, analyzed the data, and wrote the manuscript.

Erickson, ZK and AF Thompson (2018). "The seasonality of physically driven export at submesoscales in the Northeast Atlantic Ocean". In: *Global Biogeochemical Cycles* 32.8, pp. 1144–1162. DOI: 10.1029/2018GB005927.
Z.K.E. conceived the project, analyzed the data, and wrote the manuscript.

Arrigo, KR et al. (2017). "Early spring phytoplankton dynamics in the Western Antarctic Peninsula". In: *Journal of Geophysical Research: Oceans* 122.12, pp. 9350–9369. DOI: 10.1002/2017JC013281.
Z.K.E. assisted in the collection of the data, processed the CTD data, calibrated the salinity and oxygen measurements, analyzed the ADCP data, wrote Section 3.2 (Hydrography), and made Figures 1,4–6.

Thompson, AF et al. (2017). "Satellites to seafloor: Toward fully autonomous ocean sampling". In: *Oceanography* 30.2, pp. 160–168. DOI: 10.5670/oceanog.2017.238.
Z.K.E. assisted in the collection of the data and the analysis of the data.

Erickson, ZK, AF Thompson, N Cassar, J Sprintall, and MR Mazloff (2016). "An advective mechanism for deep chlorophyll maxima formation in southern Drake Passage". In: *Geophysical Research Letters* 43.20, pp. 10–846. DOI: 10.1002/2016GL070565.
Z.K.E. conceived the paper idea, analyzed the data, and wrote the manuscript.

TABLE OF CONTENTS

LIST OF ILLUSTRATIONS

LIST OF TABLES

Chapter 1

INTRODUCTION

1.1 Motivation

The ocean plays a major role in the global carbon cycle (Field et al., 1998). As the largest reservoir of carbon in the Earth system (besides the solid earth), air-sea gas transfer plays a key role in modulating the atmospheric carbon dioxide content over geologic time (Sarmiento and Toggweiler, 1984). On shorter, yearly and decadal timescales, the ocean acts to absorb roughly one quarter of anthropogenic carbon dioxide emissions, limiting the rise of carbon dioxide in the atmosphere (le Quéré et al., 2018).

This absorption of carbon dioxide is strongly time- and region-dependent, and proceeds by a variety of mechanisms. The total uptake of carbon dioxide is dominated by gas transfer across the air-sea interface into the surface ocean (a small amount is also present from river inflow), estimated at 80 Pg C/yr, or roughly ten-fold greater then the total anthropogenic emissions. However, most of this carbon (estimated at 78 Pg C/yr) is ultimately fluxed back through the air-sea interface, and the net build-up within the ocean is small, on the order of 2 Pg C/yr (IPCC, 2013).

This small build-up of carbon in the oceans is a consequence of longer-term carbon sequestration, which occurs when carbon is vertically advected out of the surface mixed layer of the ocean, which is in contact with the atmosphere. The vertical flux of carbon is related to either the sinking speed of particulate organic carbon or to vertical subduction of water masses containing fixed carbon. This thesis is primarily concerned with the second term, and especially the impact of submesoscale instabilities on the subduction of water masses out of the surface ocean.

1.2 Introduction to submesoscales

At scales of $O(100 - 1000$ km) the ocean is approximately in geostrophic balance, meaning horizontal pressure gradients are balanced by the Coriolis force, vertical shear in the horizontal flow is small, and vertical motions are negligible. Geostrophy is characterized by small Rossby numbers $Ro = \frac{U}{fL}$, where U, L are characteristic velocity and length scales and f is the planetary vorticity, and large Richardson numbers $Ri = \frac{N^2}{U_z^2}$, where $N^2 = b_z$ is the vertical buoyancy frequency and subscripts

denote partial differentiation. Other appropriate definitions for the Rossby number are $Ro = \frac{NH}{fL}$ and $Ro = \frac{\zeta}{f}$, where $\zeta = \nabla_h \times \mathbf{u}$ is the relative vorticity, ∇_h is the horizontal gradient operator, and $\mathbf{u} = (u, v, w)$. For typical ocean conditions, the geostrophic approximation is justified for scales $L \sim O(100 + \text{ km})$. At much smaller scales, $L < O(100 \text{ m})$ the pressure gradient force dominates and the ocean is approximately isotropic which is represented by large Ro and small Ri.

Submesoscales occupy an intermediate range, where the effects of planetary rotation are approximately equal in importance to horizontal pressure gradients. Dynamically, this occurs when $Ro \sim Ri \sim 1$; operationally, however, submesoscales are often taken as occurring at length scales $L \sim O(0.1 - 20 \text{ km})$.

Vertical motion at submesoscales occurs via instabilities that are generally caused by surface forcing. We return to these in a later chapter, but at the moment it is useful to define a crucial variable in the ocean: potential vorticity (PV), defined as

$$PV = (f + \nabla \times \mathbf{u}) \cdot \nabla b, \tag{1.1}$$

where ∇ is the full three-dimensional gradient operator and b is the buoyancy. (We also make the "traditional approximation" the planetary vorticity only exists along the vertical axis.) Decomposing,

$$PV = b_x(w_y - v_z) + b_y(u_z - w_x) + b_z(f + v_x - u_y). \tag{1.2}$$

A common approximation is to assume that gradients associated with the vertical velocity w are small. If we also assume the ocean is in geostrophic and hydrostatic balance,

$$u_z, v_z = \frac{b_x}{f}, -\frac{b_y}{f}, \tag{1.3}$$

and

$$PV = fN^2 + \zeta N^2 - f^{-1}M^4, \tag{1.4}$$

where $M^2 = \nabla_h b$. We assume in the following (short) discussion that $f > 0$ (true for the northern hemisphere); in the southern hemisphere $f < 0$ and some signs change, but the same qualitative observations hold. In a non-convecting ocean where $N^2 > 0$, the first term always contributes to positive PV, the third term is always negative, and the second term varies depending on the sign of ζ. Here positive PV is stabilizing and negative PV destabilizing, so horizontal buoyancy gradients (M^2) are always destabilizing. We can substitute (1.3) into our previous equation for Ri to obtain a so-called "balanced" Richardson number

$$Ri_b = \frac{f^2N^2}{M^4}. \tag{1.5}$$

Then, using $Ro = \frac{\zeta}{f}$, our PV equation becomes

$$PV = fN^2(1 + Ro - Ri_b^{-1}), \tag{1.6}$$

and we see that large negative (or at least order-unity) Rossby and small (or at least order-unity) Richardson numbers lead to negative, or destabilizing, PV.

1.3 Carbon export

This thesis is focused on understanding how biologically-generated marine carbon is sequestered in the ocean beneath the surface ocean layers. For the purpose of this thesis, this quantity will be defined as "carbon export" (Passow and Carlson, 2012). However, the term "export" is nebulous without a clear associated timescale. For example, carbon which is subducted below the mixed layer during summer may be re-entrained as the mixed layer deepens in winter. Therefore, many studies, including Chapter 3 in this thesis, focus on export during the winter and spring months. Another complication is that in up-welling favorable regions biological carbon may also be remineralized at depth and then transported to the surface, where the carbon dioxide out-gasses into the atmosphere; this thesis does not address this issue except in a one-dimensional sense in Chapter 6.

A useful metric of export is the e-ratio, which is the ratio between primary production within the surface euphotic layer, bounded by z_{eu}, and the amount of fixed carbon which descends below the z_{eu}. For convenience, a fixed depth, such as 100 m, is sometimes taken for z_{eu}. Deeper than this depth, fixed carbon is subject to remineralization but not growth. In a landmark study, J. Martin et al. (1987) used conical traps at different depths at nine stations in the northeast Pacific ocean to calculate a best-fit remineralization curve,

$$F(z) = F_{100}\left(\frac{z}{100}\right)^{-b}, \tag{1.7}$$

where F is the flux at depth z, F_{100} is the flux at $z_{eu} = 100$ m, and the exponent b is fit to available data. They found a remarkably constant fit for $b = 0.86$, suggesting that remineralization rates were roughly constant in the ocean. In a later study, (Berelson, 2001) challenged this idea, finding b from 0.6 to 1.3. The concept of an exponential power law is largely empirical, and some evidence has suggested more complex forms, such as including two power laws for labile and ballast material (Armstrong et al., 2001).

What processes control the e-ratio and Martin's b exponent? Simple food-web models typically decompose biomass into phytoplankton, zooplankton, and detritus.

The important components to the carbon export flux are detritus, in the form of either fecal pellets, dead phytoplankton aggregates, or remnants of phytoplankton or zooplankton from 'sloppy eating' (Siegel et al., 2014). Different types and sizes of organisms are also important – larger and denser phytoplankton generally grow and sink faster than smaller phytoplankton, and therefore contribute more to carbon export flux.

There are many ways to measure biological production and carbon export. Historically, carbon export was measured by floating traps in the ocean, although there are issues with selection bias in this method. For production and export simply out of the surface ocean, *in situ* measurements of variables such as chlorophyll, particulate backscatter, nitrate, phosphate, oxygen, and solar radiation can be used. Generally, these measurements must be made in a Lagrangian sense, meaning following a parcel of water (rather than at a single latitude/longitude location) over a period of days to months. In one observational study in the west Antactic Peninsula region, Stukel et al. (2015) calculated net production based on nitrate uptake in incubation experiments from water samples, net nitrate drawdown in the water column, and oxygen production (relative to argon, a gas that has similar air-sea transfer coefficients), and found good agreement between each of these three methodologies. However, their estimates of net carbon flux, from sediment traps and thorium isotopes, were significantly lower than the net estimated production, suggesting that other processes, such as diapycnal diffusion of nitrate and transport of particles across the base of the mixed layer, also had a substantial effect. In another example, (Alkire et al., 2012) used data collected from the North Atlantic during the spring bloom to compute net community production within the surface ocean using changes in nitrate, oxygen, and particulate organic carbon (POC) concentrations. They tracked an entire spring bloom cycle from initiation to termination, and found that export was highest during the time period of the main bloom. In this thesis we return to this issue of Lagrangian bloom measurements in Chapter 5, where we use a simple model to estimate export using only surface properties.

Export on larger scales can be estimated via surface measurements, which typically combine a productivity model (e.g. Eppley et al. (1985), Morel and Berthon (1989), Behrenfeld and Falkowski (1997), and Behrenfeld et al. (2005)) with an estimate of the e-ratio. Laws et al. (2000) uses a simple food web model to show a strong dependence on e with total net primary production and temperature, with the highest values for highly productive ecosystems and cold temperatures — the former is

characterized by large, quickly-growing and fast-sinking particles, and the latter is due to lower respiration rates at colder temperatures. Separating phytoplankton into two size classes (i.e. fast-growing, fast-sinking and slow-growing, neutrally-buoyant) was found to increase the skill of an empirical model at predicting e at different global sites (Dunne et al., 2005; Siegel et al., 2014). The dominance of these fast-growing size classes in high latitudes leads to an increase in e in polar regions (Henson et al., 2012).

However, the b exponent also varies greatly, including with latitude. Specifically, large, fast-growing, polar phytoplankton tend to be highly labile with respect to the more refractory slow-growing phytoplankton in low latitudes, causing their vertical transmission to be low (e.g., large b value) (Henson et al., 2012). Importantly, these characteristics of a phytoplankton bloom can change temporally as well as spatially. Buesseler and Boyd (2009) showed that from spring to summer many phytoplankton blooms evolve to have less export but higher transmission within the ocean interior as a result of a temporal shift in ecosystem composition (see also Siegel et al. (2016)).

1.4 Marine biology observations from Seagliders

Seagliders (or, "gliders") are autonomous underwater vehicles that can be deployed for months at a time, making them an attractive and (comparatively) cheap alternative to traditional ship-based ocean measurements (Rudnick, 2016). They are buoyancy-driven vehicles that can travel at a horizontal speed of about 1 km hour^{-1} and complete a dive to their maximum rated depth of 1000 m in about 5 hours.

Typical physical measurements include temperature, salinity, pressure, and oxygen concentration. In this thesis we also use biological measurements of chlorophyll fluorescence and backscatter, which give information on chlorophyll and particulate organic carbon (POC) concentrations, respectively.

Chlorophyll fluorescence

Chlorophyll molecules fluorescence when exposed to sunlight (Kautsky and Hirsch, 1931), and measurements of chlorophyll fluorescence give information on chlorophyll concentration and organism physiology (e.g., whether or not the organism is nutrient stressed). Fluorescence measurements are made by exciting the water column with light in a specific wavelength range, and then measuring emitted light (fluorescence) at a different wavelength. The chlorophyll fluoremeter used in this thesis has an excitation wavelength of 470 nm and a retrieved fluorescence

wavelength of 695 nm.

Fluorescence is emitted primarily from photosystem II of the chlorophyll complex (Behrenfeld and Milligan, 2013). The ratio of chlorophyll fluorescence to chlorophyll concentrations varies widely depending on the ambient light conditions. This variation in fact forms a core component of many biological analyses, since it can be used as a proxy for health and physiological state of the organism.

In situ measurements, however, are made in the ambient light regime. Thus, the variation of the chlorophyll fluorescence to chlorophyll concentration ratio with light plays a major role in limiting the usefulness of these measurements. In particular, under high light regimes where photosynthesis is not limited by photon availability, a variety of mechanisms exist to "quench", or use up, radiation. These are collectively known as non-photochemical quenching (NPQ) processes, and typically act to draw down chlorophyll fluorescence in the upper part of the water column.

The most common method to deal with NPQ is to disregard any fluorescence measurements made during the daytime or, if there is information on PAR, above a certain PAR threshold. This is the method used in Chapter 3. However, often disregarding all daytime measurements too drastically limits the amount of useful data. A variety of schemes have been developed to correct for NPQ effects. If the mixed layers are deeper than the effects of NPQ (determined by whether or not the profile of fluorescence starts to decrease within the mixed layer), one method is simply to extrapolate the maximum fluorescence within the mixed layer to the surface. However, this obviously is not an ideal solution, as it prohibits knowledge of any type of chlorophyll increase within the mixed layer, which may be present if the mixed layer is substantially different from the layer of active mixing (Brainerd and Gregg, 1995; Taylor and Ferrari, 2011; Ferrari et al., 2015). This method also does not effectively correct for NPQ effects if these extend throughout the mixed layer. Another alternative is to rely on other measurements. For example, if backscattering measurements were also made, they can be used as a proxy for fluorescence during the day by being scaled with the average nighttime mixed layer backscatter:fluorescence ratio. This is the method used in Chapter 4. In these above examples, fluorescence data are simply discarded (and replaced with some other source of information) when they are determined to be affected by NPQ. Alternatively, one can attempt to model the effect of NPQ on fluorescence and come up with a scaling factor based on PAR. This was done, for example, in a recent study by Xing et al. (2018), where they assumed a sigmoidal effect of NPQ with respect

to PAR.

Backscatter

Another biological measurement available on autonomous underwater vehicles such as Seagliders is backscatter, which measures the amount of emitted light scattered back to the sensor at a given wavelength by the seawater. Backscattering is strongly dependent on particle size and composition, but has been found to be linearly proportional to phytoplankton concentrations and, more generally, to particulate organic carbon (POC) in the ocean (Baker et al., 2001; Stramski et al., 2008; Boss et al., 2008). Analyses that seek to determine actual concentrations of phytoplankton or POC require additional, and labor-intensive, particle-counting measurements to find these region-specific parameters. These are typically not possible for Seaglider deployents, and accordingly in this thesis (Chapters 3 and 4) we simply use backscatter as a measurement which is understood to be proportional to POC.

1.5 Impact

This thesis focuses on the role of submesoscale instabilities in subducting carbon out of the surface ocean and into the interior, thus contributing to carbon export. In the open ocean there is likely a small window of time, particularly during spring, where this effect may contribute significantly to carbon export. Most of the results in this thesis are based on data from Seagliders, and accordingly do not have the ability to constrain fluxes to the degree that ship-based measurements involving water sampling would allow. However, within the time span during which this thesis was prepared, three major initiatives have begun that should allow the effect of submesoscale dynamics on carbon export to be much better quantified: EXPORTS (EXport Processes in Ocean from RemoTe Sensing) in the Pacific and Atlantic Oceans, S-MODE (Sub-Mesoscale Ocean Dynamics Experiment) in the California Current System, and Bio-Argo. This last project is an ongoing observational campaign that was initiated near the start of this thesis, and data from which was used in the last chapter. The goal of at least one of these campaigns, EXPORTS, is to quantify carbon export from surface measurements, which aligns very closely to the goals of this thesis, and especially the last chapter, which aims to quantify carbon export following a Lagrangian parcel (as will be done in EXPORTS).

The observational results presented in this thesis come from two very different areas. Carbon export via submesoscale subduction in the open Atlantic ocean, presented in Chapter 3, is limited due to the low temporal overlap between large submesoscale

vertical velocities (in the winter) and primary production (in late spring and summer). A roughly contemporary work by Lacour et al. (2017) suggested that wintertime submesoscale instabilities may contribute to wintertime production by stratifying the upper ocean, but also did not show that this would lead to substantially increased wintertime export. Although the observations in Chapter 3 only come from a single site in the northeast Atlantic Ocean, the same limitation is likely present in most open ocean locations.

This is in contrast to carbon export via submesoscale dynamics in southern Drake Passage, presented in Chapter 4. In this region submesoscale-driven export is driven by a thickness gradient in isopycnal layers caused by summertime surface heating, and is contemporaneous with a phytoplankton bloom, leading for a much higher potential for total carbon export. However, it is unclear to what extent these dynamics prevail in other regions of the ocean.

The ultimate goal of this thesis is to both mechanistically determine which submesoscale instabilities lead to carbon export, and understand how important they are in contributing to total export. This dissertation can be compared to a recent study by Omand et al. (2015), which estimated carbon export due to submesoscale baroclinic mixed layer instability (BMLI). This study concluded that springtime carbon export caused by this single instability could in certain regions of the ocean contribute nearly half of all carbon export. However, this prediction was a result of a simplified version of BMLI which does not accurately portray the vertical profile of subduction. In Chapter 5 of this thesis, we apply BMLI to a simple, 1-D model of the ocean, and show that it can in fact contribute much more to carbon export than predicted by Omand et al. (2015). We also analytically show that the prediction given by Omand et al. (2015) is generally accurate under conditions of strong BMLI, but that the simplified prediction can be up to four times too small under conditions of weaker BMLI, indicating that regions with low predicted submesoscale-induced carbon export may be under-estimated.

However, this thesis also points to other submesoscale instabilities, particularly symmetric (Chapter 3) and wind-driven gravitational (Chapter 5) as also contributing substantially to carbon export through subducting fixed carbon below the mixed layer and deepening the mixed layer leading to an increase in carbon export following restratification, respectively. While there are major limitations to including a representation of symmetric instability in a 1-D, surface-forced model such as is developed in Chapter 5, this model does permit understanding the spatial and

temporal signatures of both BMLI and wind-driven gravitational instabilities. In this chapter carbon export following two Bio-Argo floats in the north Atlantic Ocean is presented. Despite being in similar locations, there is a large difference both in total carbon export and relative influence of submesoscales between the different floats. This suggests substantial heterogeneity in the importance of submesoscale dynamics in carbon export, which could be further pursued by expanding the results in Chapter 5 to a greater range of data sources.

1.6 Overview of individual chapters

Chapter 2: Seasonality in the vertical structure of submesoscale variability

Variability in the ocean at scales of under 10 km is prevalent throughout the ocean, but not necessarily captured in larger scale models. Variability at these scales is also not always captured from *in situ* measurements, with the exception of surface variables, captured by remote sensing, or a few small-time-scale projects with high spatial resolution in the upper few hundreds of meters. In this chapter I consider small-scale variability in the upper 1000 m of the ocean using differences in temperature and salinity measurements made at the same time but spatially removed from each other at distances from 1–20 km. These measurements are made either from concurrently-deployed Seagliders or from an array of nine moorings that was arranged in a 20×20 km area of the north Atlantic Ocean. I show that variability in passive tracers can exist at large magnitudes but small scales even very deep in the ocean. I also use the difference in variance with separation distance to understand the underlying dynamics in the region, and find that the underlying dynamics (illustrated by the slope of the variance with respect to separation) does not meaningfully change seasonally, even though the magnitude of the changes do. In other words, the same submesoscale dynamics that give rise to small-scale variations are at play throughout the year, even though they may be more dominant during some seasons.

As of the publication of this thesis, this chapter is under review for publication in the *Journal of Physical Oceanography*.

Chapter 3: The seasonality of physically-driven export at submesoscales in the northeast Atlantic Ocean

Carbon export in the ocean is commonly defined by the sinking or subduction of carbon out of the surface, mixed layer and into the ocean interior. This presupposes that there exists a clear barrier at the base of the mixed layer. In this chapter I show that during winter this barrier becomes much less pronounced, making it

more likely that water will be able to be subducted across this boundary. I use Seaglider data to evaluate the extent to which various submesoscale instabilities – gravitational, baroclinic, and symmetric – can act to subduct material below the mixed layer. I find that baroclinic instabilities may subduct material below the mixed layer, but mainly point to symmetric instabilities, which are much more sporadic, at effectively conducting mixed layer water masses below the surface mixed layer. However, this effect has a strong seasonal cycle, which is related to the fact that the barrier at the base of the mixed layer is less pronounced during winter. Here I introduce the idea that there is an important seasonality in both submesoscale instabilities and biological production, with the former stronger in winter and the latter larger in summer. Since carbon export through physical subduction of water masses requires contributions from each of these processes, spring and fall would be potential seasons to look for carbon export in the ocean. However, I show that asymmetries in the strength of the mixed layer barrier with the interior ocean result in springtime being a more likely candidate for carbon export via subduction from these submesoscale instabilities.

This chapter is also published in *Global Biogeochemical Cycles* (Erickson and Thompson, 2018).

Chapter 4: Advective generation of deep chlorophyll maxima (DCMs) in southern Drake Passage

The previous chapter predicts that the spring season will be the most conducive to carbon export because biological production and submesoscale instabilities will both be active. This is likely the case for many open ocean regions. However, near the coast or in other regions with strong currents, other dynamics make the relationship between season and subductive export more complicated. In this chapter, I use Seaglider data to show that a phytoplankton bloom near the coast of Antarctica, in southern Drake Passage, is coincident with large horizontal buoyancy gradients that lead to a subductive flux from the continental shelf into the open ocean. This flux transports water properties, such as phytoplankton concentration, along sloping isopycnals and into the ocean interior, contributing to carbon export in this region.

This chapter is also published in *Geophysical Research Letters* (Erickson et al., 2016).

Chapter 5: Subduction from submesoscale instabilities in a simple physical model

Most biological studies to understand carbon export are Lagrangian; i.e., they follow a parcel of water over time to see how its biological properties, including carbon export, develop over time. A Lagrangian study allows the researcher to directly monitor the cycle of biological production and either sinking or subduction. In contrast, many physical oceanography studies, including the ones in the earlier chapters in this thesis, are Eulerian; i.e., they involve measurements only within a region defined by latitude and longitude bounds. This is problematic because these studies alias horizontal motions into their results, meaning they are not useful for calculating how much export is achieved for a given water mass over time. In this chapter, we develop a simple one-dimensional model of the ocean that assumes a Lagrangian reference frame and only requires surface inputs of buoyancy, momentum, and radiation fluxes. We use this model, which includes a simple biological scheme, to assess the impact of submesoscale instabilities on carbon export. We also use our model with data following a Bio-Argo float, which is a common type of Lagrangian platform.

Chapter 2

SEASONALITY IN THE VERTICAL STRUCTURE OF SUBMESOSCALE VARIABILITY

2.1 Abstract

Submesoscale dynamics are intensified at boundaries and are generally presumed to be weak in the open ocean below the mixed layer. Here we use submesoscale-resolving measurements in an open ocean region of the northeast Atlantic from Seagliders and moorings, as well as a 1/48° numerical ocean model, to probe the seasonality and vertical distribution of submesoscales using second-order structure functions, or variance in properties separated by distance. These observations are novel because of their duration for a full seasonal cycle, their ability to query horizontal spatial scales as small as 1 km, and their coverage over the upper 1000 m. Kinetic and potential energies show a clear seasonal cycle and are largest during winter. However, the dynamical features of these submesoscale motions, represented here as the slopes of their structure functions, do not exhibit seasonality. An important seasonal progression occurs during spring, when observations indicate an abrupt decrease in small-scale kinetic energy throughout the water column associated with spring mixed layer restratification. Model results do not correctly represent superinertial dynamics or the reduction of submesoscale energy during spring. Overall, these results suggest that submsesoscale motions can be important over much greater depths than the diagnosed mixed layer, especially in the weakly stratified subpolar mode waters.

2.2 Introduction

Most of the energy in the ocean is at scales of hundreds to thousands of kilometers, where the ocean is primarily in geostrophic balance (the mesoscale) (Ferrari and Wunsch, 2009). However, much of the vertical transport of oceanic tracers such as heat, carbon, and nutrients is accomplished by submesoscale motions, where the rotation and advection components of the momentum budget are of equal importance (Lévy et al., 2012). Dynamically, submesoscale motions are associated with a Rossby number $Ro \sim 1$, which in the open ocean typically occurs at spatial scales of 0.1–20 km. Submesoscale motions are largely driven via a transfer of energy from the mesoscale through mixed layer instabilities (McWilliams, 2016; Callies

et al., 2016). The strength of submesoscale dynamics and their effect on large-scale vertical exchange of passive tracers varies spatially, and we lack firm observational constraints on their prevalence.

A number of observational studies have identified seasonality in submesoscale dynamics driven by annual variation in the mixed layer depth (MLD) (Callies et al., 2015; Thompson et al., 2016; Buckingham et al., 2016; Erickson and Thompson, 2018). Deep mixed layers contain high potential energy (PE) that can be released at the submesoscale through instabilities that restratify the mixed layer (Haine and Marshall, 1998; Fox-Kemper et al., 2008). Modeling studies also show increased submesoscale activity during winter (Capet et al., 2008; Mensa et al., 2013; Su et al., 2018). Brannigan et al. (2015) find an enhancement in surface kinetic energy (KE) in the northeast Atlantic at submesoscales as model resolution is increased due to sharper fronts, stronger mixed layer baroclinic instabilities, and more frequent instances of symmetric instability. Sasaki et al. (2014) also find an increase in submesoscale activity in winter in the north Pacific, characterized by a flattening of the KE spectral slope from k^{-3} during summer to k^{-2} in winter. During the winter energy is transferred to larger scales, resulting in a temporal shift of about 100 days between the maximum KE at scales of 200–300 km compared with at scales of 10–100 km.

Under conditions where the mixed layer is bounded by a strong pycnocline, submesoscale motions within the mixed layer cannot penetrate into the interior (Boccaletti et al., 2007; Fox-Kemper et al., 2008). In general, submesoscale dynamics are assumed to be confined to the mixed layer and negligible deeper in the water column (Klein et al., 2008). However, in wintertime conditions, many parts of the ocean do not have a strong pycnocline at the base of the mixed layer, and in these locations submesoscale instabilities can extend beneath the traditionally-defined mixed layer (Erickson and Thompson, 2018). In addition, features within the ocean interior, such as subthermocline eddies (McWilliams, 1985), can also induce significant small-scale features at depth (Hua et al., 2013). Balwada et al. (2016) found that submesoscale fluxes across the base of the mixed layer increased with finer horizontal model resolution, even though the vertical stratification at the base of the mixed layer also increased, pointing to the enhancement of vertical velocities at the submesoscale.

The spatial pattern of tracers in the ocean is an important diagnostic for understanding ocean dynamics and the relative importance of submesoscales. Quasigeostrophic

(QG) theory predicts that KE will scale like k^{-3} far from boundaries (Charney, 1971). For KE spectra k^{-n}, a passive tracer scales as $k^{(n-5)/2}$ for $1 < k < 3$ (Vallis, 2006), leading to a prediction of passive tracer spectral slopes of k^{-1} in the interior. Near boundaries, sharp gradients in passive tracers can emerge, leading to slopes of k^{-2} (Klein et al., 1998). Therefore, passive tracer slopes are predicted to flatten from k^{-2} near the surface to k^{-1} at depth.

Although this relationship is obeyed in QG models (Smith and Ferrari, 2009), it is not always borne out in field studies. Cole and Rudnick (2012) found a k^{-2} structure of spice variability with minimal seasonality throughout the upper 1000 m of the water column in the subtropical North Pacific ocean. Schönau and Rudnick (2015) found a k^{-2} structure of spice variability irrespective of depth in the northern Pacific. Salinity gradient spectra along isopycnals in the California Current System were found to obey k^0, or k^{-2} for salinity variance, irrespective of season (Itoh and Rudnick, 2017). Kunze et al. (2015) also found a k^0 passive tracer gradient slope down to 100 m, and suggested non-QG stirring and internal wave/horizontal strain as possible mechanisms. Klymak et al. (2015) found an agreement with QG theory between passive and active tracers near the surface, but a reddening (steepening) of passive tracer spectra with depth, inconsistent with a surface-intensified frontal structure. Long probability distribution function tails of spice indicated sharp spice contrasts in this area down to 350 m depth. However, the exact mechanism leading to k^{-2} passive tracer slopes is unclear (Callies and Ferrari, 2013).

The propensity for passive tracer spectral slopes to steepen to k^{-2} in more quiescent open ocean regions, possibly indicative of localized stirring at these scales, points to submesoscale activity not predicted by standard theories. This submesoscale activity also has a clear seasonal cycle (see above references), and therefore observational studies spanning at least a full year are important to understand these phenomena, such as the Ocean Surface Mixing, Ocean Submesoscale Interaction Study (OSMOSIS) in the northeast Atlantic Ocean. We use glider and mooring observations from OSMOSIS to consider the seasonality of variance in active (KE and PE) and passive (spice) tracers, and compare our results to data from a high-resolution numerical model. The observations and modeling output are introduced in Section 2, where we also give an overview of the region. We use the framework of structure functions, or variance in properties binned by separation distance, as described in Section 3. The results of our structure function analysis are in Section 4, and in Section 5 we discuss differences between the model and observations, implications for theoretical

models of ocean mixing, seasonality, and mixing below the surface "mixed layer."

2.3 Data

Glider observations

Five Seagliders (gliders) were deployed in a 20×20 km region of the northeast Atlantic Ocean over a full year as part of the OSMOSIS project (Figure 3.1a,b) (Thompson et al., 2016; Damerell et al., 2016; Buckingham et al., 2016). Staggered glider deployments ensured that the region was always sampled by at least two gliders, although instrument issues for one glider during November–December 2012 rendered some of the data unusable (Figure 3.1c). Glider data processing, including thermal lag and salinity corrections, is described by Damerell et al. (2016). Glider CTD (conductivity-temperature-depth) measurements were made at approximately 1 m depth intervals. CTDs were calibrated with ship measurements made during deployment and recovery of each glider. A subsequent filter that removed any profile with an average salinity of less than 35.1 PSU or temperature less than 9°C was also found necessary to remove bad dives.

The gliders were piloted in bowtie patterns, with approximately five dives per leg, within the OSMOSIS region (Figure 2.1b). Each 'V'-shaped dive lasted approximately 5 hours and the horizontal spacing between dives was generally 2–4 km; each leg of the bowtie pattern lasted approximately one day. The glider location is transmitted before and after each dive, and the horizontal glider position during the dive is linearly interpolated with respect to time between these two points. Location error produced in this interpolation is small (see Appendix). Occasionally the gliders were advected out of the area shown in Figure 3.1c; these data were not used for the following analysis.

Mooring observations

In addition to gliders, nine moorings were arrayed in two concentric quadrilaterals with side lengths of 2–3 and ~13 km around a central mooring (Figure 3.1d). The moorings were instrumented with CTDs and Acoustic Current Meters (ACMs) at 20 to 200 m intervals within the upper 600 m (Figure 2.1e; see Buckingham et al. (2016) or Yu et al. (2019) for more details). ACMs recorded velocity data at 10 minute intervals and CTDs at 5 minute intervals; for this study CTD data were subsampled to ACM temporal resolution. Nine moorings resolve 36 different separation distances, which range from 1.2 to 18.8 km (Figure 2.1e, open circles).

The moorings were subject to currents in the area, and pressure sensors on each CTD

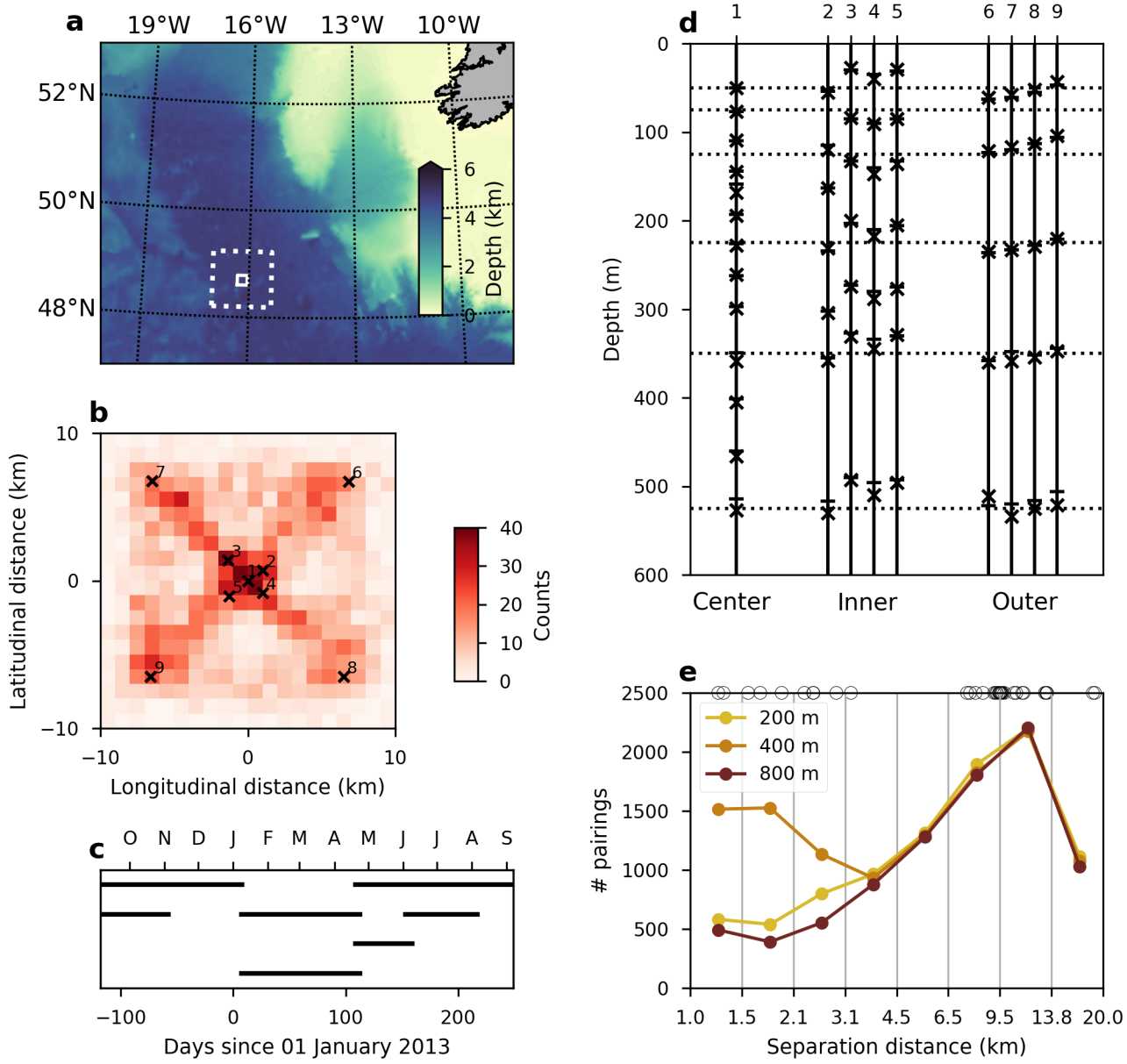

Figure 2.1: (a) Bathymetry from ETOPO in the northeast Atlantic. OSMOSIS region is shown in the white box at 16.2°W, 48.7°N. Larger region from the model is shown as the dotted white box. (b) Highlight on the OSMOSIS region, showing a histogram of glider surface locations (colors) and the positions of the nine moorings (x's). (c) Periods of time in which the gliders were active. (d) Depth placement of the ACMs (x's) and CTDs (-'s) for each mooring. Dotted horizontal lines denote the depths over which mooring structure functions were calculated. (e) Histogram of structure function pairings from glider measurements at 200, 400, and 800 m depth. Bins are equally spaced logarithmically. Circle markings at the top axis show the separations between moorings.

and ACM recorded deviations in depth of up to 150 m. These vertical deviations introduce error into the horizontal distance between moorings; however, in a separate analysis Buckingham et al., 2016 found that the buoyancy applied to the mooring cables restricts their lateral movement and creates an effective pivot point near 600 m depth; stochastic modeling predicted horizontal drifts rarely exceeding 500 m.

High-resolution model

We also analyze a region of the llc4320 model, a high-resolution 1/48° global MITgcm simulation. The model is initialized from ECCO2 (Estimating the Circulation & Climate of the Ocean, Phase II) output (Menemenlis et al., 2008), after which the resolution is increased sequentially to 1/12°, 1/24°, and finally 1/48° (Wang et al., 2018; Torres et al., 2018). The name represents the domain configuration (Latitude-Longitude-polar Cap) and the number of grid cells in the polar cap (4320×4320). The llc4320 is forced by 6-hourly ERA-Interim atmospheric reanalysis and 16 tidal components. Here we use one year (10 September 2011 to 09 September 2012) of model output from an approximately 120×120 km box centered on the OSMOSIS location (Figure 2.1a, dotted outline) and extending from the surface to 1 km depth, with a horizontal resolution of approximately 1.5 km and 52 vertical levels ranging in thickness from 1 m at the surface to almost 50 meters at 1 km depth. The model timestep is 60 seconds, and data are saved as snapshots every hour. The effective spatial resolution can be estimated as four times the grid spacing, or approximately 6 km.

The llc4320 output has previously been compared with Argo data in the Kuroshio extension, and showed reasonable vertical density stratification and seasonal variability (Rocha et al., 2016b). Globally, Qiu et al. (2018) found consistent surface eddy KE distributions between those inferred from AVISO and llc4320 sea surface height after the latter was coarse-grained to AVISO resolution. Comparisons with submesoscale-permitting observations are limited, but Viglione et al. (2018) found instances of surface instabilities at submesoscales that were temporally and spatially consistent with glider observations in Drake Passage.

Although previous work has validated a number of aspects of this model, care must be taken in making a comparison to *in situ* data. The model does not assimilate data, and in particular does not reproduce discrete events such as the occurrence of an eddy within a domain at a specific time. While the external forcing is from re-analysis data, the llc4320 output (Sep 2011–Sep 2012) does not match the timeframe of the

in situ data (Sep 2012–Sep 2013), and without observational constraints the model would decorrelate from reality even if forced by the same time period. However, statistics of ocean properties calculated over suitably large time intervals still permit a useful comparison between *in situ* observations and model results.

Site characterization

The OSMOSIS site was chosen because of the lack of major bathymetric features or mean geostrophic currents; the eddy PE and KE are moderate (Roullet et al., 2014; Rieck et al., 2015), and this study therefore provides a complement to recent manuscripts concerning submesoscale dynamics in more active boundary current regions (Rocha et al., 2016b; L. Thomas et al., 2016). The site experiences a strong seasonal cycle, which is primarily seen in annual variation of the MLD (Thompson et al., 2016; Damerell et al., 2016; Erickson and Thompson, 2018), calculated from gliders and model output as the depth at which the potential density reaches 0.03 kg m^{-3} above the potential density at 10 m (Figure 2.2a) (de Boyer Montégut et al., 2004). During autumn (October–December) the MLD steadily increases, with highly variable wintertime MLDs (January–March) reaching 400 m. These seasonally deep mixed layers lead to the production of Subpolar Mode Water in this region (McCartney and Talley, 1982). The model accurately captures the autumnal increase, wintertime variability (note that only domain-averaged values are shown), and shallow summertime values, but with a deeper mean depth during winter.

Average potential density profiles show a clear seasonality near the surface (Figure 2.2b), with a sharp pycnocline in the summer (green) absent during winter (blue). The pycnocline is also visible in vertical buoyancy stratification $b_z \equiv N^2$ of over 10^{-4} s^{-2} below the mixed layer in summer, but without a similar increase at the base of the wintertime mixed layer (Figure 2.2c). The main pycnocline, characterized by $N^2 \sim 10^{-5}$ s^{-2}, is located at about 800 m. We note that the model is lighter than the observations throughout the year, but this does not influence the structure function results below. The model also does not fully capture the strength of the summertime pycnocline (inset to Figure 2.2b).

We treat spice (Π), the component of temperature and salinity that does not contribute to density (Veronis, 1972; Munk, 1981), as a passive tracer. This approximation is valid in the absence of double-diffusive effects, which are small in this region (Damerell et al., 2016). Spice is calculated using the algorithm from McDougall and Krzysik (2015). Time series of spice during the winter–spring transition from

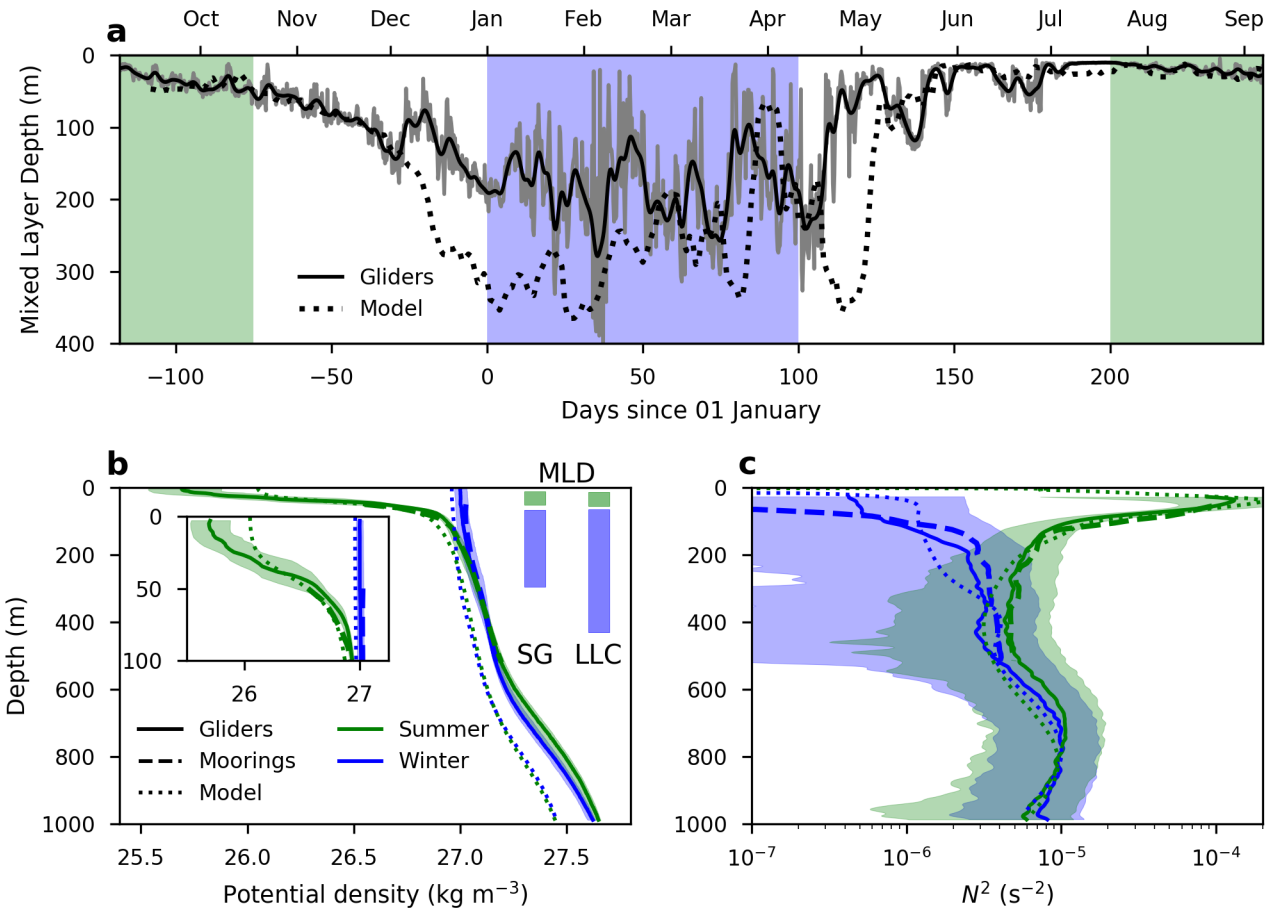

Figure 2.2: (a) MLD from glider (grey line; black line is filtered through a Gaussian window with standard deviation of 1 day) and model (black dotted line, as an average over the model region marked in Figure 3.1a). For the gliders, the date is in reference to 01 January 2013; the model reference is to 01 January 2012. Summer and winter times are indicated by green and blue shading, respectively. Average potential density (b) and vertical stratification $N^2 = b_z$ (c) for summer (green) and winter (blue) from glider measurements (solid line), moorings (dashed line), and the model (dotted line). Shading indicates the 50% confidence interval for glider measurements. Inset in panel (b) highlights the upper 100 m of the water column. Bars in panel (b) represent the mixed layer depth (MLD) of 90% of the measurements for winter (blue) and summer (green) from gliders (SG) and the model (LLC).

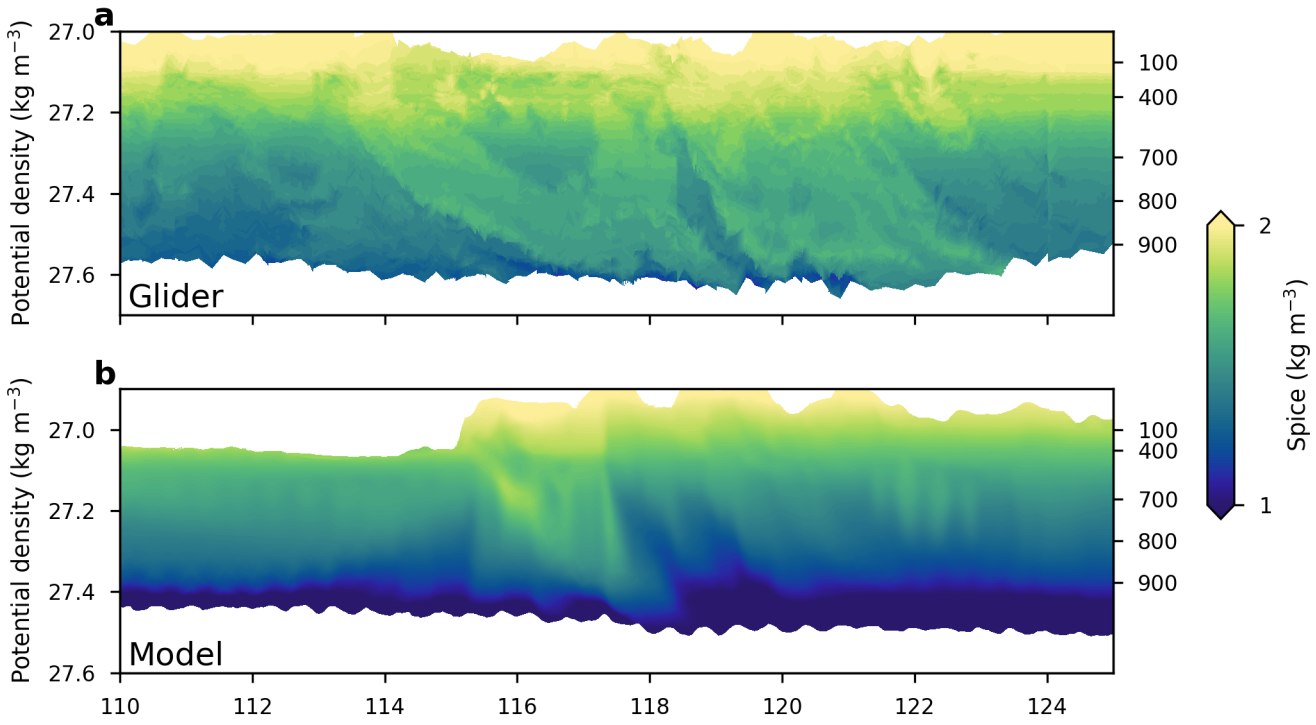

Figure 2.3: Spice along isopycnals for 15 days during April–May from a glider (a) and a single horizontal position in the model (b).

glider measurements show remarkable small-scale features extending to the very bottom of the glider measurements at 1000 m (Figure 2.3a,b). Here we eliminate the heaving effects of internal waves by considering spice along potential density rather than pressure surfaces. These features are consistent over many dives (roughly five per day) and over a range of potential density surfaces. The model also shows high spice variability at depth in coherent subductive events, such as one seen in day 115–118 (panel b; note that the alignment with an observed subductive event is coincidental).

Snapshots of spice at potential densities of 27.03, 27.07, and 27.31 kg m^{-3}, corresponding to average depths of 200, 400, and 800 m, respectively, showcase the processes captured by the model (Figure 2.4). A low-spice, mesoscale eddy in the north-west corner of the domain (dashed black boxes) stirs water masses into narrow, elongated filaments. A larger, anticyclonic eddy to the south-east of the domain has a high spice anomaly, and T-S characteristics suggest it is sourced from Mediterranean water outflow. A long filament stretches from this eddy into the center of the region studied here. The black boxes in panels e–g represent the size of the

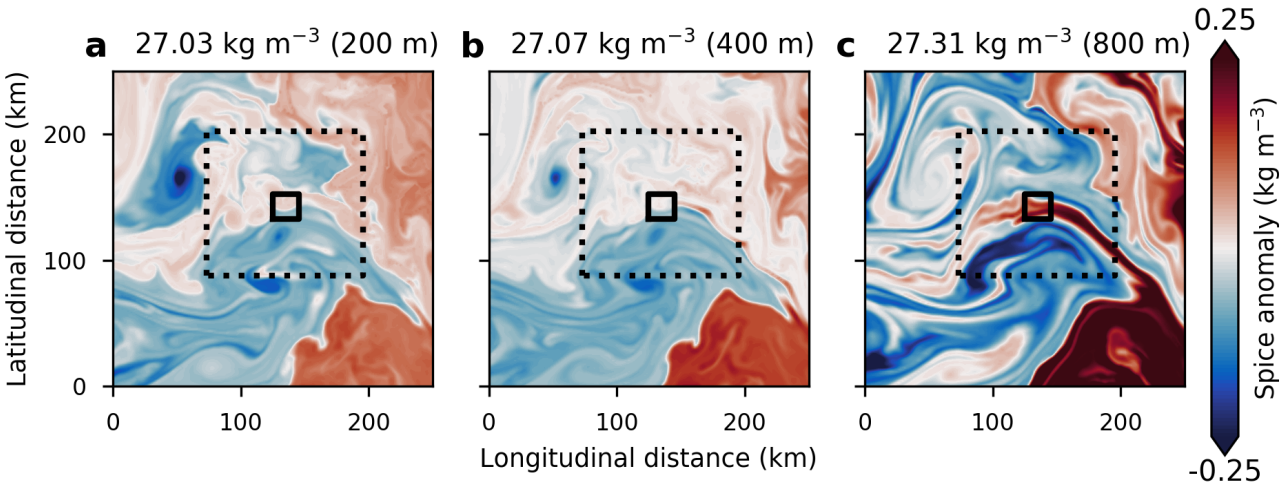

Figure 2.4: Model snapshots of spice on day 117 (April 28, 2012) for isopycnals 27.03, 27.07, and 27.31 kg m^{-3}, corresponding to average depths of 200, 400, and 800 m. Spice is shown as an anomaly from the average value in each panel domain. Black boxes give the size of OSMOSIS region (solid white box in Figure 3.1a), and the dashed black box is the domain over which the model SFs are calculated (the dashed white box in Figure 2.1a). Figure 2.3b is taken from the center of these boxes.

OSMOSIS *in situ* domain (Figure 3.1b). The high-spice anomaly associated with this filament is strongest at depth. However, although the filament width is narrow compared with the size of the eddy, it is large compared with the OSMOSIS domain and the separations resolved by *in situ* gliders and moorings. The exceptionally sharp features in the glider data are therefore not captured in the model.

Tidal influences, and especially the M2 tide, are pronounced in this region, as seen in the sharp peak at the M2 frequency in KE, PE, and spice power (Figure 2.5). The sub-inertial component of these variables agrees well between the moorings and the model; however, the model is missing considerable energy in the superinertial range of the spectra. In the mooring data, the superinertial range closely follows the Garrett and Munk (1975) (GM) spectrum for internal waves.

2.4 Structure Functions

Wavenumber spectra are traditionally used to assess tracer variance as a function of scale. However, not all datasets are amenable to spectral decomposition. Structure functions (SFs), defined below, are a useful technique when observations, such as from surface drifters (Balwada et al., 2016) or Argo floats (McCaffrey et al., 2015),

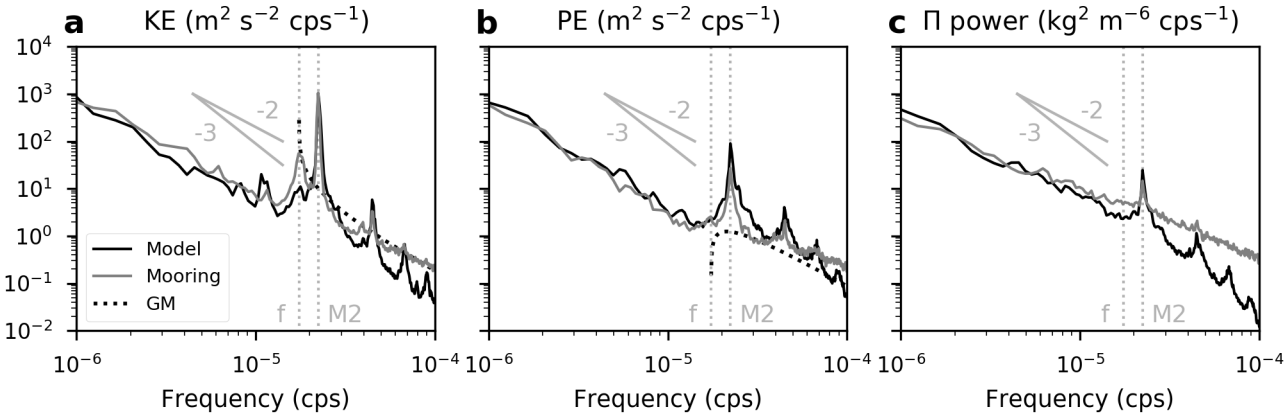

Figure 2.5: Frequency spectra of KE (a), PE (b), and spice power (c) at 350 m from the model (black) and the moorings (gray). Black dotted lines give the GM spectra, using the formula from Garrett and Munk (1975). Dashed vertical grey lines give the local planetary vorticity (f) and M2 tidal frequencies, and representative slopes of -2 and -3 are shown.

do not follow defined transects.

The nth-order SF of a scalar tracer θ is

$$D_\theta^n(\mathbf{s}) = \overline{[\theta(\mathbf{x}) - \theta(\mathbf{x}+\mathbf{s})]^n}, \tag{2.1}$$

where $\mathbf{x}$ is a position, $\mathbf{s}$ a separation distance, and boldface variables are vectors. In general $\mathbf{x}$ and $\mathbf{s}$ can be multi-dimensional, but for this study $\mathbf{x}$ represents a latitude/longitude position, $s \equiv |\mathbf{s}|$ denotes a horizontal distance and an implied temporal constraint on time differences between measurements (see below), and the overbar is an average over all $\mathbf{x}$ in a given time window.

SFs provide information on how variance (or skewness, kurtosis, et cet. for $n > 2$) changes as a function of separation distance, without requiring that all regions be sampled, as may be the case for power spectra decompositions. The second-order SF is related to the variance spectrum $E_\theta(k)$ as (Webb, 1964; Babiano et al., 1985)

$$D_\theta^2(s) = 2\int_0^\infty E_\theta(k)\,[1 - \cos(ks)]\,\mathrm{d}k. \tag{2.2}$$

Assuming $E_\theta(k)$ is represented by $ak^{-\lambda}$, for $1 < \lambda < 3$ the associated shape of $D_\theta^2(s)$ is αs^γ, where (McCaffrey et al., 2015)

$$\gamma = \lambda - 1. \tag{2.3}$$

In analogy to spectra of KE and PE, we define

$$D_{KE} = \frac{1}{2}\left(D_u^2 + D_v^2\right) \text{ and} \tag{2.4a}$$

$$D_{PE} = \frac{D_b^2}{2\overline{b_z}}, \tag{2.4b}$$

where b is buoyancy, u, v are the velocities in the x, y direction, and the z subscript denotes partial differentiation in the vertical. Although horizontal velocities from gliders can be estimated using depth-average current calculations and assumptions of thermal wind shear, there is no reliable way to estimate the vertical structure of along-track velocities. We therefore do not attempt a calculation of D_{KE} using glider data.

Applying the SF framework to different types of datasets in a consistent way is challenging due to differences between the different datasets. Due to their 'V'-shaped dives, gliders sample the same depth at time separations spanning seconds to hours. While multiple gliders were generally in the water at the same time, permitting in theory simultaneous measurements, to achieve the necessary number of measurement pairings at different separations (Figure 2.1e) it was necessary to allow measurement pairings with up to 3 hour temporal separation. For separations of 1 km motions at 10 cm/s and faster are therefore aliased into the results. However, modifying this threshold slightly does not meaningfully change the qualitative results in this paper, and shortening it significantly degrades the number of observations.

For the moorings, we allow only simultaneous (within 5 minutes) measurement pairings, but must contend with vertical movements of moorings through the water column due to internal wave activity. These were recorded by pressure sensors on each CTD and ACM instrument. We only calculate mooring SFs along 6 depths that are well-instrumented (Figure 2.1d, horizontal dotted lines), and only allow measurements that were taken within 10 m of these target depths (using the simultaneous pressure measurements).

For the model, we used the domain represented by the dashed black boxes in Figure 2.4, and only permitted pairings within the same model snapshot. This represented 80×80 pixels, or over 40 million possible pairings. We randomly selected 750 points throughout the domain, for over 500,000 pairings. Random sampling of other 750-point sets did not meaningfully change any of the calculated statistics.

Other details of computing the SFs using the *in situ* datasets are given in the Appendix.

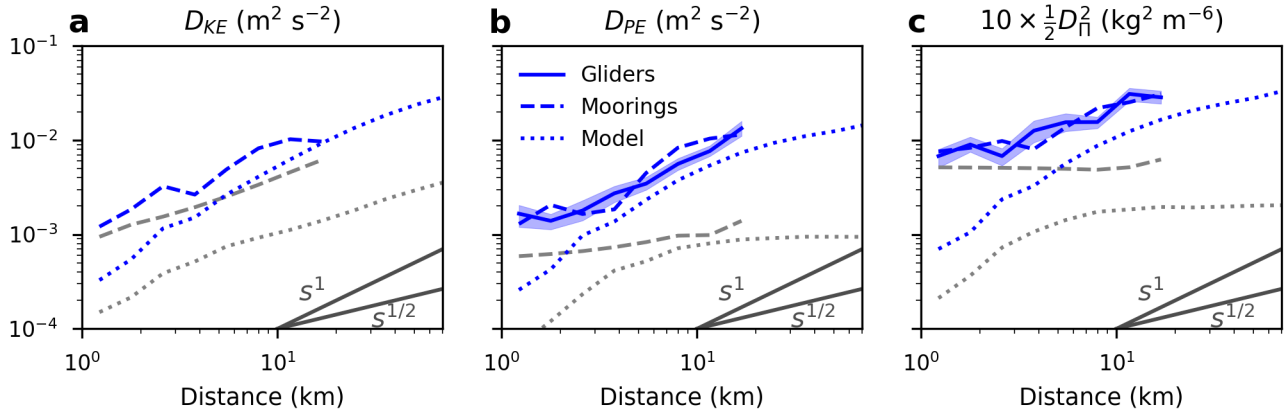

Figure 2.6: Structure functions (SFs) for kinetic energy (KE; a), potential energy (PE; b), and spice (Π; c) for winter (see Figure 2.2a) at 350 m from gliders (solid), moorings (dashed), and the model (dotted). Blue lines correspond to the standard SF calculation; grey lines are only using super-inertial frequencies as described in the text. The 90% confidence interval from a bootstrap analysis is given in light shading for the glider results. Confidence intervals for the mooring and model are not shown, but are small compared to those for the gliders. Representative slopes of s^1 and $s^{1/2}$ are shown in each panel.

2.5 Results

We construct SFs of KE (D_{KE}; Equation 2.4a), PE (D_{PE}; Equation 2.4b), and spice ($\frac{1}{2}D_\Pi^2$; Equation 2.1) from the gliders, moorings, and model during winter and summer. The results for winter at 350 m depth are shown in Figure 2.6. Slopes for D_{KE} and D_{PE} for *in situ* data are close to 1, corresponding to a spectral slope of k^{-2}. The passive tracer SF, D_Π^2, is significantly shallower, at a slope of close to 1/2, or $k^{-1.5}$. SF slopes of KE and PE show good agreement between the model and *in situ* measurements at scales of 4–20 km (Figure 2.6a,b). At scales smaller than about 4 km, the *in situ* measurements from gliders and moorings are both much flatter than the model. Spice SFs are in general much flatter in the observations than the model results, indicating greater spice variance at small scales (as seen in Figures 2.3 and 2.5). At larger scales, the model slope decreases, representing a saturation of variance at scales approaching 100 km. This is consistent with the lack of larger-scale features in this region.

We test the influence of internal wave heaving by calculating SFs along the isopycnal surface most closely aligned to this depth, and do not find a significant difference, indicating that internal waves have only a small imprint on this analysis (not shown).

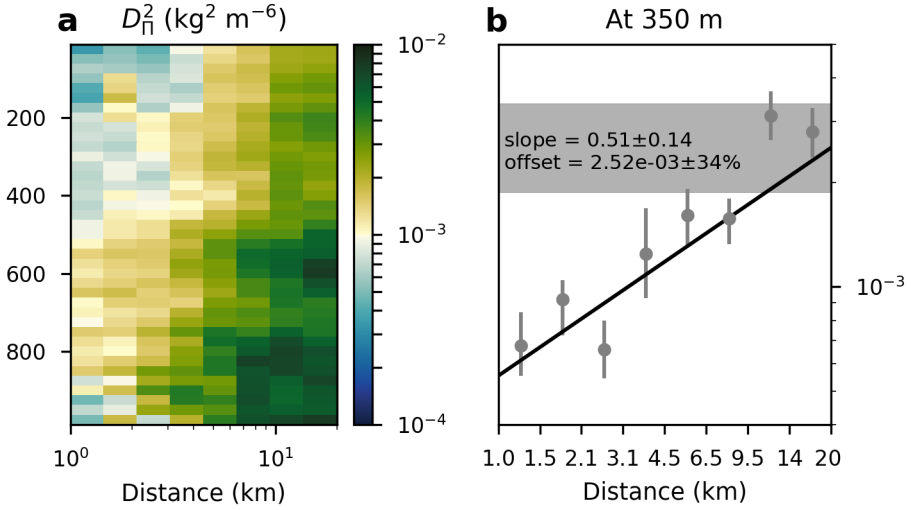

Figure 2.7: (a) Structure function of spice power at all depths from the glider using winter time data. (b) Example of calculating best-fit slopes for a representative SF taken from 350 m depth on panel (a). Black line gives the best fit to the data, and grey horizontal bar shows the range of values of the offset, defined as the variance at 20 km separation.

We decompose the model and mooring measurements into super- and sub-inertial components by filtering out signals at frequencies less than and greater than 16 hours, respectively, corresponding to the local inertial period. The mooring super-inertial SFs are spectrally flat, and can even be dominant over the sub-inertial component for D_{KE} and D^2_Π at scales less than 5 km (sub-inertial results not shown, but are equivalent to the sub-inertial SFs subtracted from the full SF). The model results, in contrast, show little variance associated with super-inertial motions, and the sub-inertial SFs are similar to the full SF at all scales. This is an important result from this *in situ* dataset, as theoretical and numerical models of stirring in the ocean do not typically account for super-inertial motions (e.g., Smith and Ferrari (2009)).

SFs can be calculated at any depth to provide a full vertical structure of variance in a given property. An example for wintertime spice variance from gliders is shown in Figure 2.7a. This calculation reveals larger spice variance with increasing depth and increasing separation. In particular, the ability to resolve spice variance at scales below 20 km at up to 1 km depth is a major asset of this dataset.

In the range spanning 1–20 km, this information can be well-summarized by a

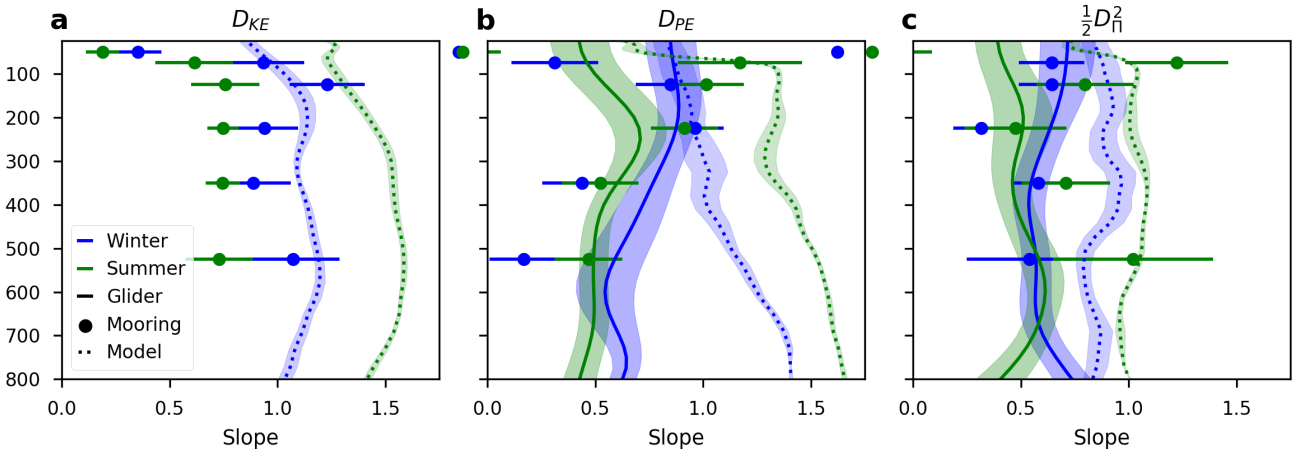

Figure 2.8: Best-fit slopes of KE (a), PE (b), and spice (c) structure functions from gliders (solid), moorings (dots), and model (dotted line) during winter (blue) and summer (green). Shading and error bars show the standard deviation of the fits.

power-law curve

$$D^2_\Pi = b(s - s_0)^\gamma, \tag{2.5}$$

where b is an 'offset' representing the variance at a separation of $s_0 = 20$ km. We fit the SFs to Equation (2.5) using a Levenberg-Marquardt minimization algorithm (example shown in Figure 2.7b). Weights for the *in situ* calculations are given as inverse standard deviations, calculated as the spread of the 90% confidence interval divided by 3.29 (i.e., assuming Gaussian distributions). For the gliders, we smooth the final b and γ results vertically with a Gaussian window with a standard width of 3 pixels (75 m). For the mooring data, we only calculate the SFs along depth surfaces with sufficient measurements (see Figure 2.1d), corresponding to 50, 75, 125, 225, 350, and 525 m. For fits to modeled data we use only SF calculations for s between 4 and 20 km, as this s-domain has relatively uniform slope.

The best-fit slopes (γ) for winter and summer are shown in Figure 2.8. Shading and error-bars give the standard deviation on the fit; however, this is an incomplete description of the full uncertainty. In some instances slopes (and offsets, discussed below) can vary depending on the precise time range chosen for winter and summer, and since we only have one year of data de-convolving seasonal effects with either inter-annual oscillations or chance occurrences in one year, such as an eddy drifting into the region, is not possible. We therefore only comment on those properties that we believe to be robust.

The *in situ* slopes for D_{KE} reveal surprisingly little seasonal variance, and are rather constant with depth, at about 0.7 (Figure 2.8a). The model, in contrast, shows a striking seasonality, with slopes increasing dramatically, indicating less variance at small scales, during the summer. For D_{PE}, the slope varies with depth in the upper 200 m in the summer, being small (greater variance at small scales) near the surface and increasing throughout the summertime pycnocline (Figure 2.8b). During the winter, evidence of a clearly defined mixed layer is muted. For the *in situ* results there is some evidence that the mixed layer is characterized by a rather uniform slope, which decreases below the average wintertime MLD of about 200 m. The model shows a much clearer transition across the base of the mixed layer base, with a dramatic increase in slope associated with the summertime pycnocline, and a smaller increase starting at the base of the wintertime mixed layer.

The slopes in spice variance are more difficult to interpret, and seasonal differences probably rely more on the presence of eddies and small-scale filaments moving through the region (Figure 2.8c). However, the larger slope (less variance at small scales) in the model vs. the *in situ* measurements, at least outside of the mixed layer, does appear to be a robust result.

The best-fit offsets (b) are shown in Figure 2.9. *In situ* D_{KE} offsets show a clear seasonal cycle in the mooring measurements, with higher variance in the winter (Figure 2.9a). Modeled results show a slight increase in summer; however, if values from the beginning of the model run (the previous summer) are added this relationship reverses itself, and we believe this seasonal difference is due to the model not being completely spun up.

The seasonality and vertical dependence in the offsets for D_{PE} (Figure 2.9b) largely follow changes in the vertical stratification b_z. It is, however, noteworthy that the model exhibits little seasonality below the base of the wintertime mixed layer, whereas seasonality persists in the *in situ* measurements down to the seasonal thermocline below 800 m. We believe this to be a signature of vertical mixing below the mixed layer during the winter, as discussed further in the next section.

The offsets in spice power are also shown in Figure 2.9c for completeness; however, as with the changes in slopes we do not believe any of the seasonal or depth variations to be significant.

Calculating best-fit slopes and offsets for time periods throughout the year reveal this seasonal difference between *in situ* and model results more clearly. There are

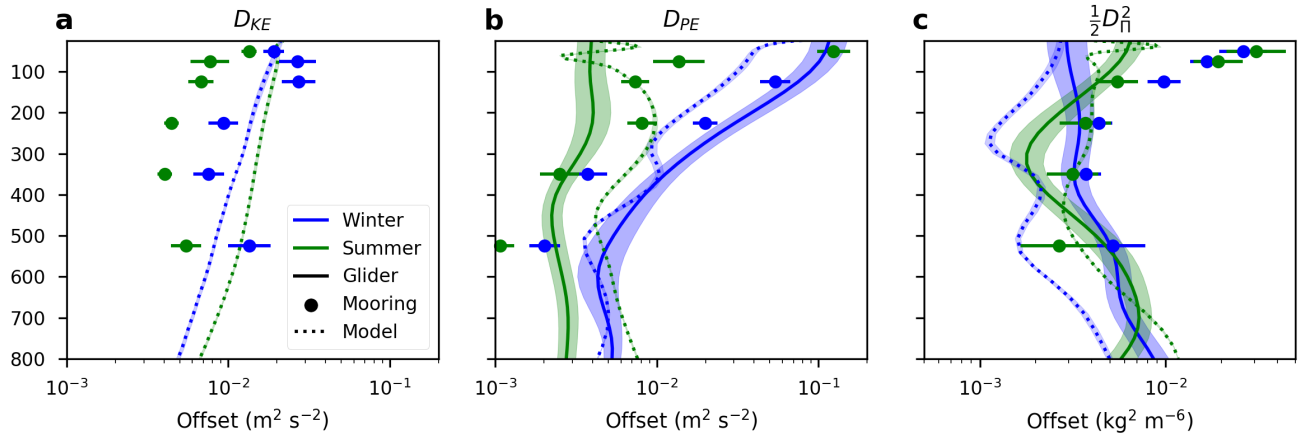

Figure 2.9: Best-fit offsets of KE (a), PE (b), and spice (c) structure functions from gliders (solid), moorings (dots), and model (dotted line) during winter (blue) and summer (green). Shading and error bars show the standard deviation of the fits.

small, likely insignificant changes in slopes throughout the year (not shown). The seasonality in offset shows a much larger signal for KE and PE (Figure 2.10). The KE in the model peaks much later, during the spring, than in the mooring results, which have their maximum signal during the winter. For PE, each of the three datasets — gliders, moorings, and model results — peak during in early winter at 50 m and later in winter for the deeper depths. However, the model also has a strong PE signal at 20 km in late spring which is not present in the *in situ* dataset. The cause of this is unclear, but likely related to the dynamics of the spring restratification, which involves small-scale instabilities such as baroclinic mixed layer and symmetric instabilities (Erickson and Thompson, 2018) that will not be fully represented in the model.

2.6 Discussion

Difference between high-resolution model and observations

Because of their utility across a wide range of types of data, SFs are useful to evaluate model fidelity with respect to observations. Here we perform a comparison between *in situ* and model data output using SFs at 1–20 km resolution. A key difference highlighted in this study is the increased slope of all of the SFs (KE, PE, and spice variance) in the model. The SF values at 20 km, labeled 'offsets' or b here, are more comparable, indicating that this increase in slope represents too little variance at small scales. This is an expected characteristic of models, for which variance

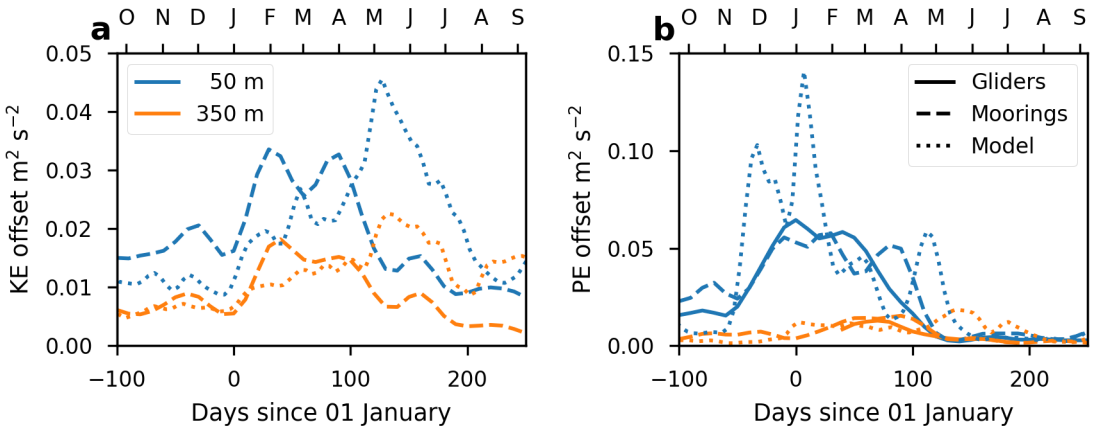

Figure 2.10: Best-fit offsets of KE (a) and PE (b) applied to moving 30-day windows at 50 and 350 m (colors) for gliders (solid), moorings (dashed), and model results (dotted). Data have been smoothed in time.

on scales smaller than about 4-5 model pixels (about 6 km here) is expected to be artificially low, and can also be seen in spectral deconvolutions (e.g., Figure 2.5).

However, we also point to the lack of high-frequency, super-inertial motions in the model as producing this lack of variance at small scales (Figure 2.6). Although the time-step of the model, at 60 seconds, could sufficiently resolve these motions, it is forced with 6-hourly reanalysis winds, which do not input energy at sufficiently high frequencies. Recent work has suggested that models that are subject to surface forcing at super-inertial frequencies develop greater variance at super-interial frequencies, which from Figure 2.6 we suggest will translate into more realistic properties at small spatial scales.

Implications for theoretical models of vertical structure of ocean mixing

As reviewed in the Introduction, there exists considerable uncertainty over the expected slopes of passive and active tracers in the ocean interior. In particular, at the surface frontogenesis can cause slopes of k^{-2}. Far from the surface, active tracers are predicted to have slopes similar to k^{-3}, which predicts passive tracers slopes that flatten from k^{-2} to k^{-1}.

Spice SF slopes are near 0.6 and exhibit little seasonality or vertical variability. Active tracer (KE and PE) slopes estimated from *in situ* data are generally between 0.6 and 1. This agrees well with the theoretical relationship between active and passive tracers: for an active tracer SF slope of n the predicted passive tracer SF

slope is $1 - n/2$.

A spice SF slope of 0.6 corresponds with a spectral slope of $k^{-1.6}$, which is significantly shallower than that shown in previous studies in other parts of the ocean (Cole and Rudnick, 2012; Schönau and Rudnick, 2015; Itoh and Rudnick, 2017; Kunze et al., 2015). Some of these studies are in regions with significant frontal structures, such as the Pacific Ocean North Equatorial Current (Schönau and Rudnick, 2015) or the California Current System (Itoh and Rudnick, 2017), where significant differences may exist from the OSMOSIS site location. The Kunze et al. (2015) study spanned scales from 5 m to 50 km; at scales that match our observations they could not distinguish between a spice gradient slope of k^0 and $k^{1/3}$; this latter corresponds to a SF slope of 2/3, which is close to our estimated value. Finally, Cole and Rudnick (2012) interpolate their glider data in the horizontal to find passive tracer slopes of k^{-2}. This interpolation can significantly change calculated slopes; when we interpolate our glider data in the vertical we find a substantial steepening of the spice SF slope to near 1 (or, k^{-2}). Finally, Klymak et al. (2015) found similar spice spectral slopes near the surface, which became significantly steeper with depth, unlike the uniform slope we find here. This study therefore suggests that the apparent k^{-2} slope in passive tracer spectra may be more isolated to regions with strong frontal structure, at least at scales of 1–20 km.

Seasonality in small-scale variance

There is clear seasonality in this region in properties such as the MLD and the strength of the pycnocline at the base of the mixed layer (Figure 2.2; see also Erickson and Thompson (2018)). This seasonality is also reflected in our 'offset' values, representing the degree of variance at 20 km separation (Figure 2.9). In particular, there is considerably more KE and PE represented in the winter than the summer. However, the seasonality is shifted in the model compared with the observations, in that the model KE peaks in spring and still remains high even into summer conditions (Figure 2.10a).

A key feature of spring is the restratification, which can be caused by direct surface forcing but also initiated by baroclinic mixed layer instabilities (Mahadevan et al., 2012; Erickson and Thompson, 2018). These instabilities are at scales of 1–20 km and are therefore not well-resolved in the model. During the model year, the spring restratification is pushed later in the season than in the observations (Figure 2.2a). However, the peak in KE is pushed even later in the year. The corresponding peak in

PE is significantly muted. We suggest that the model is not accurately representing the springtime restratification. From Figures 2.5 and 2.6 we see that superinertial motions in particular are not well-captured in the model. We suggest that during the spring restratification in the model, tidally-induced currents can become trapped in the shoaling mixed layer and intensify, whereas in the real ocean these motions are dispersed throughout wavenumber space (as seen in Figure 2.5, grey lines).

Interestingly, however, seasonality is not evident in the SF slopes estimated from the *in situ* data (Figure 2.8). This suggests that the dynamical balance setting small-scale tracer evolution at scales of 1–20 km does not fundamentally change seasonally. In other words, the same qualitative features reminiscent of submesoscale turbulence are active during both the summer and the winter.

Why does the model show changes in SF slopes between the two seasons in KE and PE? An appropriate Rossby radius is $L_r = 2\pi \frac{N_{th} H}{f}$, where $N_{th} \sim 2 \times 10^{-}3$ s^{-1} in the 200–400 m region (Figure 2.2c) and H is the MLD, which is about 20 m in the summer and 200 m in the winter. Then submesoscales will be energized at the Rossby radius of about 3 km in the summer, but 30 km in the winter due to the difference in MLD. The model grid resolution is about 1.5 km, which is too coarse to accurately resolve motions at the Rossby radius in the summer, but can resolve these same motions in the winter, leading to a seasonality in slopes at small scales in the model that is not represented in the actual ocean.

Mixing below traditionally-defined surface mixed layer

Temporally-varying MLDs are shown in Figure 2.2a from the gliders and the model, calculated using a density difference threshold method. One might assume that properties, such as the SF offsets and slopes calculated from Equation 2.5, would change at the base of the mixed layer. In fact, there is a slight change in properties associated with the shallow summertime pycnocline, but very little abrupt change across the base of the wintertime mixed layer for the *in situ* data. The model, however, shows a stronger change across the wintertime mixed layer base, which is most apparent in the changes of slope of D_{PE} (Figure 2.8b).

The effect of model resolution can be seen in a series of recent simulations performed by Balwada et al. (2018), where an idealized MITgcm was run at horizontal resolutions between 20 and 1 km. As the resolution increased stratification at the base of the mixed layer also increased, but so did the vertical transport of tracers across the mixed layer base. The authors attributed this increase in vertical transport

to increased strength of baroclinic mixed layer instabilities at higher resolution.

The high spatial resolution on horizontal velocities by the mooring array also allows a calculation of the vertical velocity through the density conservation equation (Yu et al., 2019). This estimate showed strong vertical velocities of up to 100 m day^{-1} extending 200 m below the mixed layer during winter and spring. Vertical velocities from from the llc4320, as well as also supported this observation (see their Appendix D).

In this study we used spice as a passive tracer, and found that there is not a clear sign of spice variance changing across the base of the mixed layer during winter, either in slope or magnitude. Other passive tracers, such as oxygen, nutrients, and dissolved organic carbon, can also be transported across the base of the wintertime mixed layer in a similar fashion. Erickson and Thompson (2018) found evidence of rapid downward transport of high-oxygen waters below the wintertime mixed layer using OSMOSIS glider data, and attributed this downward flux to intermittent submesoscale instabilities, with a particular focus on symmetric instability. These instabilities provide a mechanism both for upward transport of nutrients as well as downward transport of neutrally buoyant carbon, especially during winter.

2.7 Conclusions

The OSMOSIS project provides a useful testing ground to consider seasonality in submesoscale dynamics. We considered statistical relationships between spice, buoyancy, and horizontal velocities in the context of second-order structure functions, which give similar information to spectral decompositions but are better suited to data from arrays of moorings and gliders.

This unique observational dataset is the first to enable a statistical description of turbulence properties down to scales of 1 km over a full seasonal cycle to 1 km depth. Thus we were able to probe scales that would be expected to be only marginally resolved even in relatively high-resolution global models, for example the 1/48° llc4320 analyzed in this study.

An important finding of this study was the emergence of sharp features in spice at scales of less than 5 km well below the mixed layer. These small-scale features are present in a region of the ocean without strong currents or important bathymetric features, signifying that the results here may also occur in other open ocean areas.

We found a clear difference between *in situ* data and model results at small scales, where the *in situ* data had much more variance than the model. This is expected, as

the effective model resolution is approximately a factor of four larger than the grid scale resolution. However, the model did compare well with the mooring data using only the sub-inertial components of velocity, buoyancy, and spice variables, even down to very small separations (2 km). This points to high-frequency motions as being the key unresolved physics in the model simulation.

The other important aspect of this study was to highlight the seasonal cycle. In the winter mixed layers are deeper, yet the model mixed layers are deeper than the *in situ* data, which we conclude is due to unresolved restratification processes. However, the model structure functions agree much more closely with the *in situ* results during winter than in summer. One reason for this is that the model is more accurately resolving the important physical instabilities in the winter than the summer, because surface-enhanced submesoscale motions are larger in size when the mixed layer is deeper. This lack of sufficient resolution is most apparent during spring, when restratification processes make use of available potential energy to quickly shoal the mixed layer, removing submesoscale energy in the process. In the model high variance in velocities remain throughout spring and into summer, meaning the model does not efficiently transfer this energy to dissipative scales.

We also put this study in the context of other publications which have found a k^{-2} spectral slope of passive tracers in the ocean regardless of depth. Here we do not reproduce this steep slope, and present this dataset as a counterexample to several other studies suggesting a universal k^{-2} passive tracer spectral slope at depth.

Finally, we point to the importance these results may have for the vertical transport of properties beneath the mixed layer. This is especially important for biological properties such as particulate or dissolved carbon, where vertical exchange across the mixed layer base may lead to sequestration and carbon export on long time scales. Our observations suggest that the boundary between the ocean-atmosphere interface and the ocean interior — the pycnocline at the base of the mixed layer — is not well-developed during the wintertime, meaning the conventional distinction between well-mixed surface waters and an ocean interior out of contact with the atmosphere may not apply during all seasons.

2.8 Appendix

Structure function implementation for Seagliders

For each dive, the temperature and salinity at depths ranging from 25 to 975 m, at 25 m intervals, was linearly interpolated. CTD sensor precisions are 0.0003 S m^{-1}

and 0.001°C for conductivity and salinity, respectively, combining for an estimated 0.001 PSU preciion in salinity. Spice and buoyancy were calculated. The associated precision in this region of temperature-salinity space is within 0.001 kg m^{-3} for spice and 0.0001 m s^{-2} for buoyancy. Latitude and longitude were linearly interpolated with respect to time from surface GPS locations. assiming perfect 'V'-shaped dives. In reality, the glider transcribes a path which is dependent on fine-scale dynamics. Gliders pilot underwater using a compass and pressure sensor, and can control their motion through rolling and pitching (Eriksen et al., 2001). Using heading, pressure, pitch, roll, and surface GPS measurements, a flight model (UEA Seaglider toolbox; http://www.byqueste.com/toolbox.html; see also Frajka-Williams et al. (2011)) was used to estimate the actual path of the glider through the water column. The difference between the flight-model and the 'V'-shaped dive estimates is small at the surface and generally less than 1 km at 1000 m (Figure 2.11). The average error on the distance between a pair of measurements is $\delta x\sqrt{2}$, where δx represents the error on a single location. The median error on glider-glider distances is therefore between 0–0.6 km from the surface to 1000 m depth, with 5% of pairings at 1000 m depth having an estimated separation error of greater than 2.2 km. A "flat Earth" approximation is made to convert degrees of latitude and longitude into distances (111.12 km per degree of latitude, and 73.38 km per degree of longitude).

Observations at different separations were grouped according to the logarithmically-spaced bins represented in Figure 3.1c. Measurements systematically oriented towards one end of a given bin could bias averaged values; however, subdividing the pairing distances in Figure 3.1d into smaller bin sizes does not show any systematic bias (Figure 2.12; mean distance in each bin not shown, but in most cases is statistically indistinguishable from the center of each bin).

Pairings were also grouped into time period bins, either for a season (defined as in Figure 2.2a) or into staggered 30-day windows (Figure 2.10). These were bootstrapped by choosing values randomly (with replacement) and recalculating statistics; the uncertainty shown in Figure 2.6 is based on the 90% confidence intervals from this analysis.

Structure function implementation for moorings

The moorings were instrumented with CTD and ACM instruments as shown in Figure 2.1e. Pressure sensors on these registered "knock-down" events throughout the year which deepened the instruments by up to 150 m. To calculate the SFs, we

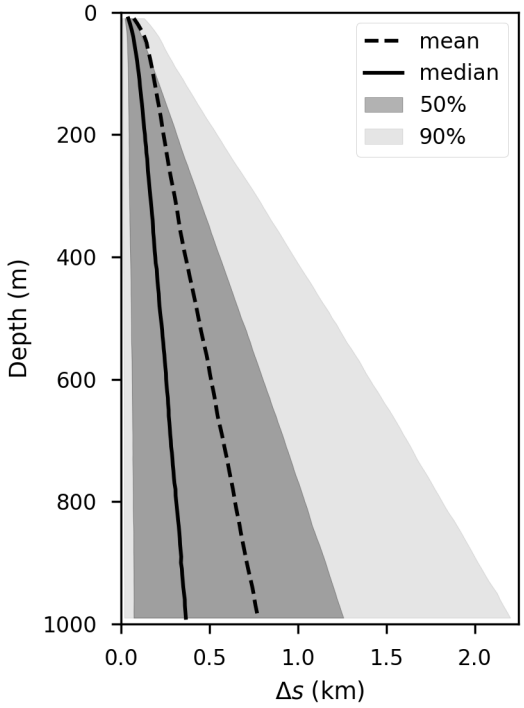

Figure 2.11: Uncertainty in glider position, represented as the mean distance between modeling as 'V'-shaped dives and using the flight model (see text). Median (solid black line), mean (dashed black line), 25–75th percentiles (medium grey shading), and 5–95 percentiles (light grey shading) shown as a function of depth.

permitted mooring measurements that were within 10 m of the target depth. Interpolating measurements vertically between instruments was found to significantly modify the final SF results, and therefore no vertical interpolation was performed here. As described in the text, we used observations at 10 minute intervals. We only permitted pairings between moorings that were at equivalent recorded times, and only plotted points with at least 200 such pairings.

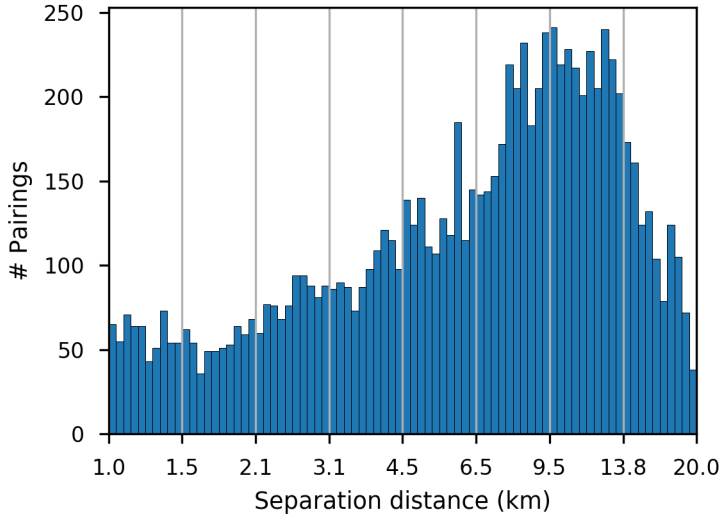

Figure 2.12: Histogram of separation distances in glider pairings for 200 m depth, where each "distance bin" has been subdivided into ten logarithmically-spaced units.

Chapter 3

THE SEASONALITY OF PHYSICALLY-DRIVEN EXPORT AT SUBMESOSCALES IN THE NORTHEAST ATLANTIC OCEAN

3.1 Abstract

Submesoscale dynamics $O(1 - 100\,\mathrm{km})$ are associated with enhanced vertical velocities and evolve on a timescale similar to that of biological production (hours to days). Here we consider an annual cycle of submesoscale dynamics and their relation to productivity and export in a small (20×20 km) region of the northeast Atlantic Ocean. In this region, a springtime bloom is initiated by re-stratification of the mixed layer in June, although intermittent shoaling of the mixed layer maintains phytoplankton populations throughout the year. An optical community index suggests a dominance of large species (e.g., diatoms) during spring and picophytoplankton during the winter. We review three types of submesoscale instabilities — mixed layer (baroclinic), gravitational, and symmetric — and consider the impact of each on export of fixed carbon out of the surface layer. Mixed layer instabilities can potentially export material out of the mixed layer during winter, although the vertical velocity across the base of the mixed layer is sensitive to the parameterization scheme. Symmetric instabilities, in contrast, provide a clear mechanism for rapid export out of the mixed layer. A crucial factor determining export potential is the strength of the pycnocline at the base of the mixed layer. Export production is sensitive to the degree of overlap that exists between intense submesoscale activity associated with deep mixed layers in the winter and high productivity associated with the spring restratification, meaning physically-driven export of fixed carbon will likely happen over a short time window during spring.

3.2 Introduction

Marine biota account for approximately half of global primary productivity (Field et al., 1998), yet the residence time of carbon in the biosphere is an order of magnitude smaller in the ocean than on land. There is a clear seasonal cycle of phytoplankton biomass, with bloom dynamics in the mid-to-high latitudes dominating during spring. Blooms develop on timescales of days, which is much shorter than the evolution timescale of weeks for mesoscale eddies and fronts (where "mesoscale" signifies length scales L such that the Rossby number $Ro = \frac{U}{fL} \ll 1$, where f

is the planetary vorticity and U is a characteristic velocity). Biological processes are therefore often implicitly assumed to happen in a stationary physical regime. However, research in the field of submesoscale dynamics motions characterized by $Ro \sim 1$) has shown the importance of scales of $O(1 - 100$ km) in stimulating large vertical velocities and lateral and vertical tracer transport (Mahadevan and Tandon, 2006; Lévy et al., 2012; Rosso et al., 2014; Brannigan, 2016; McWilliams, 2016). Submesoscale dynamics evolve on a timescale ofhours to days, which is similar to the timescale of biological production. The ability of submesoscale dynamics to influence biological production and export fixed carbon out of the surface ocean is not well understood.

Phytoplankton blooms are typically considered to be a result of restratification-driven shoaling of the mixed layer into the euphotic zone (Sverdrup, 1953; Mahadevan et al., 2012). Blooms are generally dominated by diatoms, which exist at low concentrations during the winter (Kostadinov et al., 2009) and may be maintained during this time through small-scale restratification events (Lacour et al., 2017). However, phytoplankton biomass in the surface ocean does not necessarily lead to carbon export. Much progress has been made considering this problem in a one-dimensional Lagrangian framework, where the important processes controlling export are aggregation, sinking, and predation with the associated formation of fecal pellets and other detritus (Ducklow et al., 2001; Stemmann et al., 2004).

Sinking of particulates, whether in the form of single organisms, aggregates, detritus, or fecal pellets, is not the only method by which carbon is exported. Physical subduction of water masses can also induce export. At the largest scales, this is the reason for the observed distribution of chlorofluorocarbons, nutrients, and oxygen in the ocean interior (Broecker et al., 1998). One mechanism for this subduction is due to surface buoyancy forcing (heating or precipitation) during spring capping the deep wintertime mixed layer, which in some locations leads to export either through net advection of high-biomass waters deeper into the interior along isopycnals or through consumption of dissolved organic carbon and subsequent particulate sinking (Sarmiento, 1983; Carlson et al., 1994). However, processes at the submesoscale, where the effect of planetary rotation is no longer dynamically dominant, can drive vigorous vertical motions of up to hundreds of meters per day (Lévy et al., 2012). The effect of these small-scale vertical motions in bringing nutrients from depth into the euphotic layer and stimulating production is seen in high-resolution models (Mahadevan and Archer, 2000; Lévy et al., 2001; Brannigan, 2016). Observations

also suggest that these vertical motions can subduct water high in chlorophyll below the mixed and euphotic layers (Hood et al., 1991; Washburn et al., 1991; Erickson et al., 2016). The combined effects of submesoscale motions may dominate export in much of the highly-productive ocean (Omand et al., 2015).

Submesoscale dynamics are particularly active in regimes with large lateral shear, such as boundary currents (L. Thomas et al., 2013; Molemaker et al., 2015; L. Thomas et al., 2016; Rocha et al., 2016b; Rocha et al., 2016a) or the Antarctic Circumpolar Current (Erickson et al., 2016). However, a growing body of evidence shows that vigorous submesoscale activity is present even in the relatively quiescent open ocean (Brannigan et al., 2015; Thompson et al., 2016; Su et al., 2018). The open ocean is generally oligotrophic or mesotrophic (commonly defined as surface chlorophyll values below 1 mg m^{-3}), but constitutes a large fraction of total export due to its large areal extent (Laws et al., 2000). Seasonality in the energy content of submesoscale motions is related to seasonality in the mixed layer depth (MLD) (Sasaki et al., 2014; Callies et al., 2015), and may affect export throughout the year.

Although high-resolution models show the importance of submesoscale motions in the injection of nutrients into the mixed layer and subduction of particulate organic carbon (POC) out of the mixed layer (Mahadevan, 2016), few *in situ* studies have been able to resolve these scales. In the Sargasso Sea, Estapa et al. (2015) used high resolution O_2/Ar and thorium isotope measurements to show that net community production and export production were uncorrelated at scales less than 10 km. They associated this short decorrelation length scale with small-scale vertical circulation systems (Lévy et al., 2012). Off the coast of California, Stukel et al. (2017) found evidence of carbon export through downward transport along isopycnals in frontal regions, and estimated that this subductive flux was comparable in magnitude to that of export through particle sinking. They hypothesized that similar mechanisms would exist in eastern boundary upwelling systems worldwide, representing a significant flux in the global carbon budget. In another instance, Omand et al. (2015) used Lagrangian measurements of phytoplankton and export in the North Atlantic (Alkire et al., 2012) to estimate the effect of submesoscale dynamics, through baroclinic instability in the mixed layer, on export production. Using satellite and climatological data, they found that eddy-driven subduction from submesoscale instabilities could account for 30-60% of export in much of the productive ocean.

Here we use observations from Seagliders (hereafter, gliders) in the northeast At-

lantic Ocean to examine the seasonal cycle of phytoplankton and assess the potential for export due to submesoscale instabilities throughout the year. In contrast to the Lagrangian approach typically used (e.g. Alkire et al. (2012)), we do not follow a water mass or characterize the evolution of a single water parcel. Instead, we continuously measure properties in a 20×20 km region of the ocean (Figure 3.1), providing a yearly cycle of biological variables such as fluorescence, backscatter, and oxygen, as well as physically relevant measurements of horizontal and vertical buoyancy gradients at scales of 3-5 km in the horizontal and 2 m in the vertical. These latter measurements allow the calculation of potential vorticity (PV), which we use to characterize instabilities and link them to export production in this region. The unique aspect of this dataset is its resolution and duration; we measure biological and physical properties at submesoscale resolution from September 2012 to September 2013, and can therefore study the full seasonal cycle of production and submesoscale dynamics.

We consider the theoretical framework of submesoscale instabilities using buoyancy gradients and PV in Section 2, followed by our observations and results in Sections 3 and 4. In Section 5 we discuss how our observational results are affected by the theoretical mechanisms outlined in Section 2 at the event level and their relevance for annual export estimates, before concluding with Section 6.

3.3 Theoretical framework

At large scales $O(100+$ km), the ocean is approximately in hydrostatic and geostrophic balance, meaning the vertical and horizontal pressure gradients are balanced by gravity and the planetary vorticity (Coriolis force), respectively. Vertical velocities are weak, and horizontal flows are non-divergent and evolve over timescales of weeks or longer. At smaller scales $O(1 - 100$ km), the effect of planetary rotation is less dominant, and ageostrophic dynamics may become important. Since global ocean models are rarely able to resolve these scales directly, a variety of parameterizations for submesoscale dynamics have been developed.

An important diagnostic variable that provides insight into submesoscale motions is potential vorticity

$$\mathrm{PV} = \omega_a \cdot \nabla b, \tag{3.1}$$

where $\omega_a = f + \nabla \times \mathbf{u}$ is the absolute vorticity, expressed as the sum of the planetary and local vorticities, $b = g(1 - \rho/\rho_0)$ is the buoyancy, g is gravity, ρ is potential density, $\rho_0 = 1025$ kg m^{-3}is a reference density, and $\mathbf{u} = (u, v, w)$ are velocities in

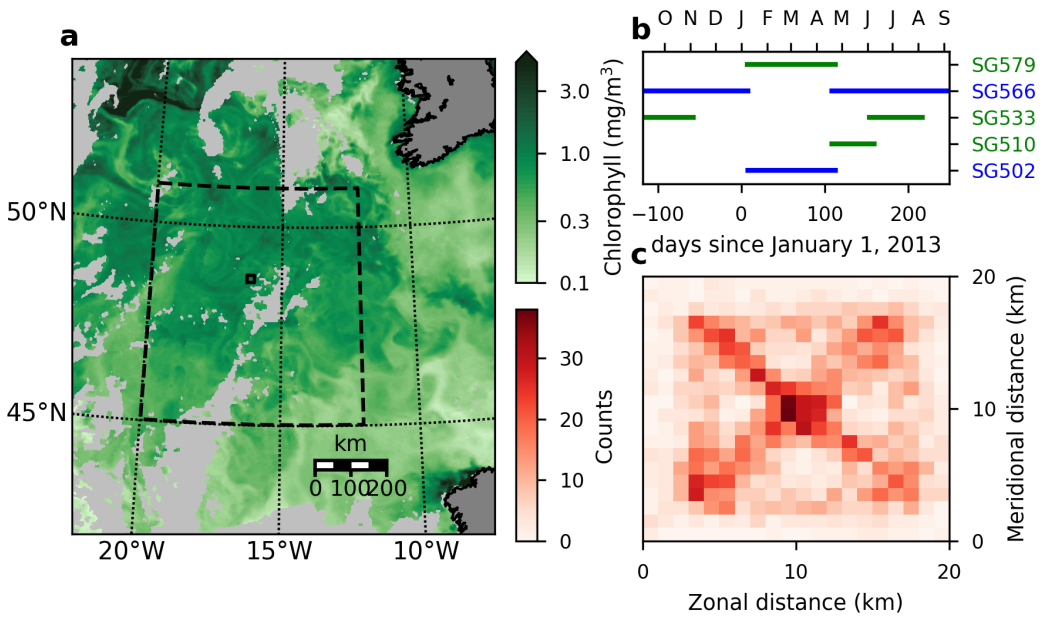

Figure 3.1: (a) Average surface chlorophyll concentration from 12-19 July, 2013 from MODIS Aqua. Light grey gives cloud-covered areas, and dark grey are land masses (Ireland in the upper right, and the Iberian peninsula in the lower right). Note the logarithmic colorbar. OSMOSIS region is shown in the black box centered at 16.2°W, 48.7°N, and the region used for the satellite-derived bloom time series in Figure 3.2 is shown by the black dashed line. (b) Deployment periods for each of the five gliders. Blue gliders are hereafter referred to as "Glider 1"; green are "Glider 2" (Table 3.1). (c) Histogram of surface locations for each vertical glider profile over the entire five-glider deployment, encompassing a total of 7,458 profiles. Each grid point is 1×1 km.

the (x, y, z) direction. PV is conserved in the absence of diabatic effects, such as wind stress or surface buoyancy forcing at the ocean surface, implying that once a fluid parcel subducts out of the mixed layer its PV is fixed.

If we assume terms associated with the gradient of the vertical velocity w are small, Equation (3.1) becomes

$$\mathrm{PV} = (f + \zeta)b_z + u_z b_y - v_z b_x, \tag{3.2}$$

where $\zeta = v_x - u_y$ is the local vertical vorticity and subscripts denote partial derivatives. Assuming thermal wind balance, $(u_z, v_z) = (-f b_y, f b_x)$. Substituting $N^2 = b_z$ and $M^2 = \left(b_x^2 + b_y^2\right)^{1/2}$ as the squared vertical and horizontal buoyancy frequencies, respectively, results in

$$\mathrm{PV} = fN^2 + \zeta N^2 - f^{-1}M^4. \tag{3.3}$$

The first term is generally positive (in the northern hemisphere, where $f > 0$). The second term can take either sign, and is responsible for the asymmetry in submesoscale dynamics between cyclonic ($\zeta > 0$) and anticyclonic ($\zeta < 0$) eddies (Rudnick, 2001; Brannigan et al., 2017). The third term is always negative, and can become large in frontal regions.

We use the framework of buoyancy gradients and PV to review three types of submesoscale instabilities: baroclinic instability within the mixed layer, gravitational instability, and symmetric instability. In Section 5 we return to this framework to estimate the potential for each type of instability to export fixed carbon out of the surface ocean.

Mixed layer (baroclinic) instability

Baroclinic instability occurs due to the release of potential energy stored in lateral density gradients. Baroclinic instability energizes submesoscale motions within the mixed layer (where it is sometimes called mixed layer instability; MLI), where surface buoyancy forcing or lateral stirring by mesoscale eddies causes strong horizontal buoyancy gradients to develop. MLI slumps steep isopycnals associated with large lateral density gradients, releasing potential energy by converting horizontal buoyancy gradients b_x into vertical gradients b_z, generally over a period of days (Haine and Marshall, 1998; Boccaletti et al., 2007). This overturning of density surfaces always acts to restratify the water column, and can be expressed in terms of a vertical streamfunction

$$\psi_{MLI} = 0.06 \frac{\mu(z) b_x \mathrm{MLD}^2}{|f|}, \tag{3.4}$$

where $(u, w) = (-\psi_z, \psi_x)$ (Fox-Kemper et al., 2008). The term

$$\mu(z) = \left[1 - (1 - 2z')^2\right]\left[1 + \frac{5}{21}(1 - 2z')^2\right], \tag{3.5}$$

where $z' = z/\mathrm{MLD}$, is a vertical structure function which goes to zero at the surface and base of the mixed layer, following a "no normal flow" condition at the boundaries of the mixed layer, which is assumed to be bounded by a highly stratified pycnocline at its base (Fox-Kemper et al., 2008).

MLIs have been implicated in initiating both small-scale (Lacour et al., 2017) and large-scale (Mahadevan et al., 2012) restratification-driven blooms, as well as driving submesoscale subduction of POC (Omand et al., 2015). However, their ability to, by themselves, subduct material out of the mixed layer is limited. As

they are normally parameterized (e.g. Fox-Kemper et al. (2011), Gent et al. (2011), Hurrell et al. (2013), Tjiputra et al. (2013), Danabasoglu et al. (2014)), MLIs have no signature below the MLD due to $\mu(z)$, which is equivalent to assuming that the base of the mixed layer is a solid boundary. We will return to this assumption in Section 5, where we discuss the implications for export through MLI of a mixed layer with weak stratification at its base.

MLIs can also lead to subduction and export when combined with diabatic processes, such as spring restratification driven by positive atmospheric heat flux. In this scenario, MLI subducts material from the surface to the base of the mixed layer, and another process, such as atmospheric buoyancy or Ekman forcing (see below) forms a new mixed layer above the now-subducted material. The export potential of this mechanism is, however, dependent on the definition of "export" used. Unless this capping of the mixed layer is associated with a downwelling regime (leading to mode water formation) or death and sinking of phytoplankton, this material will simply be re-entrained into the mixed layer during the next mixing event.

Gravitational instability

Gravitational instability (GI) releases potential energy in statically unstable density profiles ($b_z < 0$). GI is an integral part of the seasonal cycle, as surface cooling during the autumn and winter deepens mixed layers. Conversely, spring surface heating increases b_z and contributes to a stable re-stratification of the mixed layer. GI can also arise when the surface wind stress (τ) interacts with horizontal surface buoyancy gradients. If a component of the wind stress is perpendicular to the horizontal buoyancy gradient, surface Ekman transport will advect dense water over light if the wind stress is in the same direction as the geostrophic flow, and vice versa if it is in the opposite direction (L. Thomas and Lee, 2005). As with surface buoyancy forcing, Ekman-driven gravitational effects can either de-stabilize or re-stabilize a water column.

Surface buoyancy and Ekman forcing is directly related to the mixed layer, since the MLD is, to a large extent, determined by the depth upon which buoyancy and Ekman forcing act. Therefore, GI will not act to subduct water masses beneath the mixed layer, since by definition this will cause the mixed layer to deepen. Stratifying buoyancy or Ekman forcing can, however, trap water masses beneath a new, shallower mixed layer and indirectly lead to export, as mentioned in Section 2.1.

Symmetric instability

Symmetric instability (SI) is a shear instability which drives vigorous slantwise convection along isopycnals (Hoskins, 1974). It arises from the interaction between buoyancy and absolute momentum restoring forces in areas with strong horizontal buoyancy gradients and weak absolute momentum gradients. Diagnostically, a water column is symmetrically unstable when $f\mathrm{PV} < 0$ and $-1 < Ri_b < f/\zeta$, where $Ri_b = \frac{f^2 N^2}{M^4}$ is the balanced Richardson number (L. Thomas et al., 2013). Taylor and Ferrari (2009) used idealized nonlinear simulations to find that Kelvin-Helmholtz instabilities ultimately relieve SI by mixing high-PV waters from the pycnocline with low-PV waters from the SI-unstable mixed layer. The time scale for this process is of order hours.

Because SI is often associated with large b_x, water columns that are symmetrically unstable are also subject to MLI. The depth to which SI acts can be approximated as the deepest depth H for which (Bachman et al., 2017)

$$\int_0^H PV \mathrm{d}z > 0 \tag{3.6}$$

(see also Appendix 2 of Whitt et al. (2017)). Here we calculate this value directly from Equation 3.3, with the approximations already discussed. The end result of SI is to homogenize the PV above this depth to zero, at which point MLI acts on the remaining horizontal buoyancy gradients (Haine and Marshall, 1998).

3.4 Data

We use data primarily from glider observations in the Porcupine Abyssal Plain (PAP) region of the northeast Atlantic Ocean (Figure 3.1a). The region is located between the subtropical and subpolar gyres, is far from boundaries, and has no major bathymetric features. It experiences springtime bloom dynamics fueled by nutrients input into the surface ocean mainly through wind stress-induced mixing during winter (A. Martin et al., 2010; Rumyantseva et al., 2015). Both the initiation of the springtime bloom and flux of particles from the surface boundary layer exhibit substantial interannual variability (Hartman et al., 2010; Lampitt et al., 2010), with peak bloom times ranging from March to June (Figure 3.2). The seasonal distribution of MLD is controlled primarily by the air-sea heat exchange, with cooling and mixed layer deepening in winter and warming and shoaling in summer, although advection of waters into the area is also significant (Damerell et al., 2016).

Five gliders were deployed in pairs from September 2012 to September 2013 near the PAP site, with deployment times ranging from two to five months (Figure 3.1b,

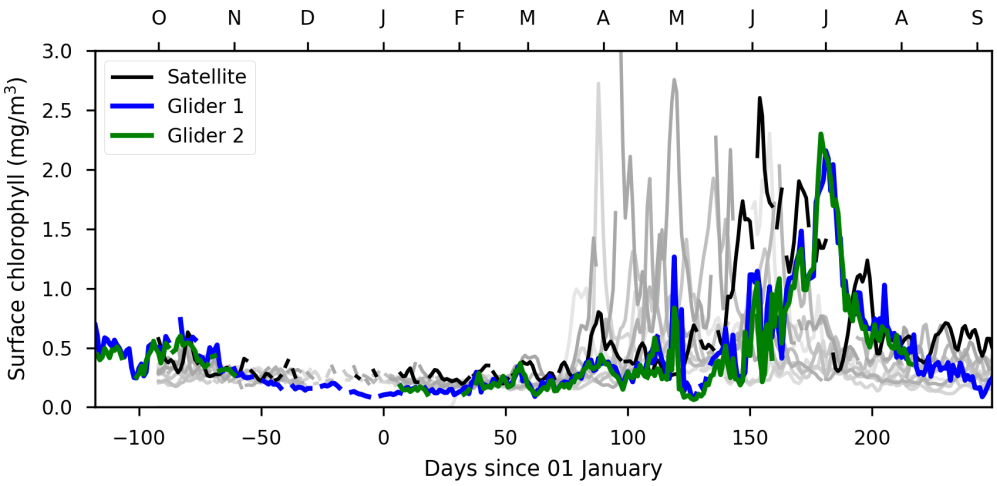

Figure 3.2: Average surface chlorophyll concentrations each year from 2002-03 to 2011-12 from MODIS Aqua (grey lines, chronologically light to dark) using the region within the dashed black box in Figure 3.1a. Thick black line is from 2012-13, which covers the OSMOSIS study period; blue and green lines are the average data in the upper 25 m, after calibration, for Gliders 1 and 2, respectively (see Section 3 and Table 3.1).

Table 3.1), as part of the Ocean Surface Mixing, Ocean Submesoscale Interaction Study (OSMOSIS). For the purposes of this paper, we define gliders SG502 and SG566 as "Glider 1" and SG510, SG533, and SG579 as "Glider 2" (Figure 3.1b; Table 3.1). Thompson et al. (2016) and Buckingham et al. (2016) show evidence of seasonality in submesoscale turbulence from the gliders and from moorings deployed over the same time period, respectively. Here we consider the connection between submesoscale dynamics, productivity, and the potential for export in this region.

The gliders were piloted in bow-tie shaped paths within a 20×20 km region of the ocean centered at 48.7°N, 16.2°W (Figure 3.1c). Dives were V-shaped to 1 km depth, with 3-5 hours and 2-4 km between surfacings, or about a day per leg of each of the transects. The gliders all carried unpumped CTD sensors measuring conductivity (salinity), temperature, and depth (pressure) at a vertical resolution of less than 1 m. Calibration of glider sensors is typically done using ship-based profiles at deployment and recovery (as in Damerell et al. (2016)). The advantage of this method is the high confidence in ship-based sensors which can themselves be calibrated before, after, and during the cruise. A disadvantage is the lack of calibration measurements during the glider deployment, which can be important if

Table 3.1: Biological sensor packages (WET Labs ECO Puck) for each glider deployment. Glider # refers to its designation in Figure 3.1b. Scale-factor if the multiplicative factor between MODIS Aqua and glider observations, where n is the number of MODIS Aqua observations used to calculate the scale-factor.

Seaglider		Deployment dates		Backscatter wavelength		Chlorophyll calibration	
ID	#	Start	End	Sensor 1	Sensor 2	scale-factor	n
SG502	1	08 Jan 2013	23 Apr 2013	470 nm	700 nm	1.9	17
SG510	2	19 Apr 2013	09 Jun 2013	650 nm	—	4.1	9
SG533	2	06 Sep 2012	08 Jan 2013*	650 nm	—	3.2	7
	2	03 Jun 2013	05 Aug 2013	650 nm	—	2.8	10
SG566	1	04 Sep 2012	08 Jan 2013	650 nm	—	3.1	11
	1	19 Apr 2013	07 Sep 2013	650 nm	—	3.1	26
SG579	2	08 Jan 2013	23 Apr 2013	532 nm	—	2.2	14

*Issues with the temperature sensor rendered CTD data unusable after 04 November.

a sensor starts to drift mid-deployment or if time considerations, inclement weather, or sensor malfunction prohibits calibration measurements during deployment or recovery (as happened for the first recovery of SG533; see Table 3.1). Instead, we perform an inter-glider calibration, which capitalizes on the overlap in glider deployments. Specifically, average temperature and salinity values with respect to depth were compared across glider platforms over time intervals when both were in the water. Sensor drifts were not observed, but depth-dependent offsets of salinity and temperature for individual gliders were required, of up to 1 PSU and 0.06 °C, respectively.

In addition to the physical measurements, each of the gliders carried an Aanderaa oxygen optode and WET Labs sensors for induced fluorescence (hereafter, fluorescence) and optical backscatter (hereafter, backscatter) at various wavelengths (Table 3.1). Oxygen and WET Labs measurements were taken roughly every 1-2 m in the vertical to depths between 200 and 500 m, although occasional profiles to the full depth of 1 km were also taken to retrieve the background signal. Oxygen measurements were calibrated against ship-based oxygen measurements before and after each cruise, which were themselves calibrated with Winkler titration of water samples (Umberto, 2016). The gliders also carried PAR sensors (Photosynthetically Available Radiation; 400-700 nm), which were used by Hemsley et al. (2015) to calculate productivity, and all but one glider had a CDOM (Colored Dissolved Organic Material) sensor. The CDOM measurements were largely within the noise range for the sensor, and contained instrument effects related to the sampling frequency,

for which we are at present not able to correct. We therefore do not consider the CDOM data further in this paper.

Fluorescence and backscatter data are often used as proxies for chlorophyll concentration (e.g. Boss et al. (2008)), but care must be taken in interpreting them as such. Fluorescence measures the potential productivity of the water sample (Daly et al., 2004), and is typically scaled to a chlorophyll concentration using laboratory measurements of a diatom monoculture (*Thalassiora weissflogii*) after accounting for a linear offset (dark counts). A major difficulty in converting fluorescence to chlorophyll concentrations is in correcting for non-photochemical quenching (NPQ), defined as the sum of all processes that reduce fluorescence in high-light conditions as a protection mechanism for the light-harvesting apparatus (Cullen and Lewis, 1995). A common correction algorithm makes use of backscatter data and a known ratio between backscatter and fluorescence in areas not affected by NPQ (Boss et al., 2008). Self-shading by phytoplankton in the water column can also be measured by a PAR sensor and used to correct for low fluorescence values (Xing et al., 2011; Hemsley et al., 2015). Because we use a long time-series and some of our results concern changes in the fluorescence to backscatter ratio, we circumvent the issue by using only nighttime fluorescence data.

Laboratory-based estimates of dark counts are rarely consistent with the *in situ* instrument response, so here we determine the dark counts for each glider as the median of all measurements below 600 m depth for each glider deployment (for the first deployment of SG533, we instead use measurements below 280 m because no measurements deeper than 300 m were taken). In so doing, we make the assumption that fluorescence below this depth (well below the euphotic zone) is negligible. Fluorescence profiles often show abrupt spikes, which may be due to aggregated material (Briggs et al., 2011). We filter out these spikes using a 5-point minimum followed by a 5-point maximum filter (similar to the method used in Briggs et al. (2011)). The spike signal shows no structure, and here we only consider the filtered (baseline) signal.

Recent results have shown that factory-calibrated ECO Puck sensors' measurements of chlorophyll are greater than *in situ* chlorophyll measurements by a factor of 1-6 (Roesler et al., 2017). We determine this scaling factor by comparing daily average (nighttime) surface measurements in the upper 25 m with estimates of chlorophyll from the nearest MODIS Aqua measurement (OC3 algorithm; Level 3 gridded product at 4 km resolution), and obtain factors comparable to Roesler

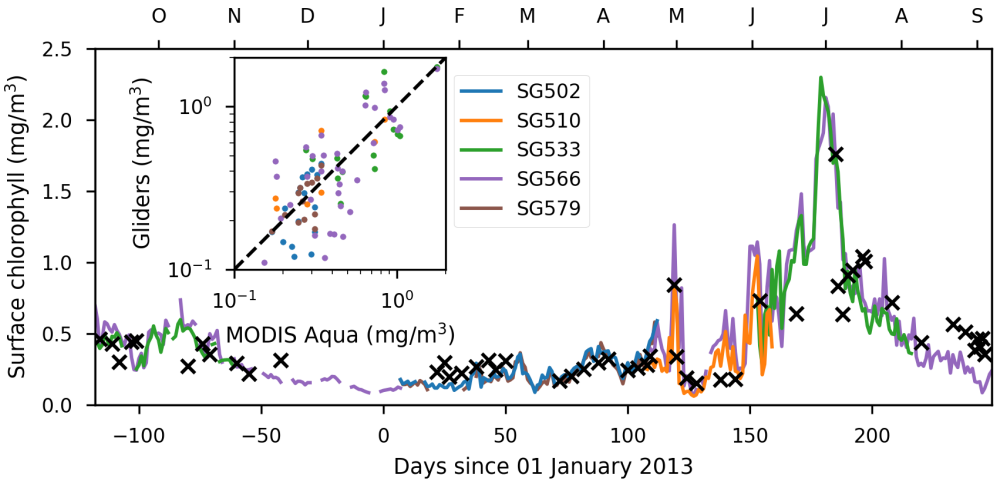

Figure 3.3: Surface chlorophyll data from each glider averaged over the upper 25 m during nighttime (colors), after calibrating with MODIS Aqua overpasses (black crosses; see Table 3.1 for scaling factors). Inset scatters calibrated glider measurements against MODIS Aqua results, where the dashed black line is 1:1.

et al. (2017) (Table 3.1). Using satellite data rather than ship-based measurements allows calibration throughout the deployment, which might span several ecological regimes. However, additional uncertainty is introduced because satellite chlorophyll concentration estimates are less reliable than ship-based laboratory measurements. We compare our calibrated Seaglider data with MODIS Aqua estimates (x's) in Figure 3.3, where the inset shows a scatter plot of the observations after calibration. The relatively small number of comparisons is due to frequent cloud cover in this region. Substantial scatter still exists in the calibration, but this scatter is relatively evenly distributed about the 1:1 line (inset). Much of this can be explained because of the comparison between point-measurements by the gliders and average measurements over an approximately 1 km^2 footprint by MODIS Aqua. In addition, up to 12 hours can separate the nighttime glider observation from the satellite measurement, which has a local overpass time between 13:00 and 15:00. Jacox et al. (2015), however, showed that calibration measurements can be effective tens of kilometers and many days distant from the *in situ* observation.

Backscatter data are from sensors with wavelengths ranging from 470 to 700 nm. We offset for dark counts using the same procedures as for fluorescence. In this case, finding an offset as the median value below a certain depth is less well-justified. Backscatter presented here is thus more accurately the difference in backscatter from

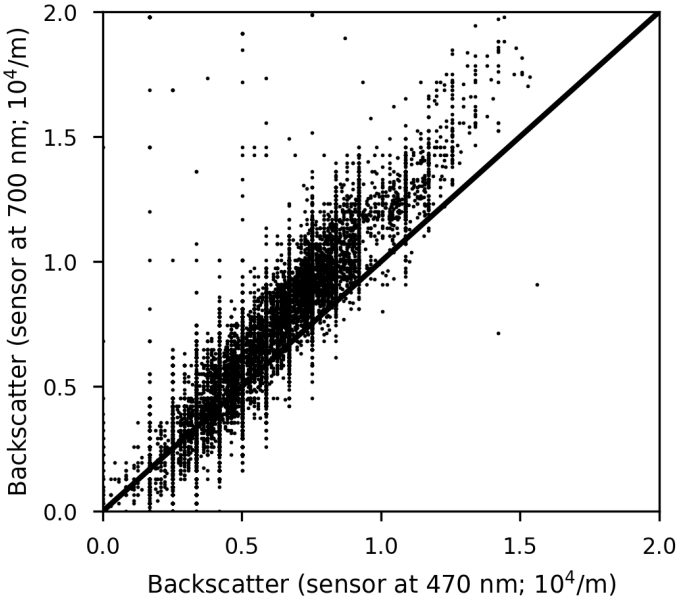

Figure 3.4: Scatterplot of coincident backscatter measurements at 470 and 700 nm from SG502 after offset, de-spiking, and calibration using a wavenumber slope of k^{-1} as described in the text. The ideal 1:1 line is shown in black.

a bulk interior value. In order to treat all wavelength sensors equally, we convert to an equivalent measurement at 650 nm assuming a k^{-1} slope of backscatter with respect to wavelength (Boss et al., 2008). We test this relationship using SG502, which was equipped with backscatter sensors at 470 and 700 nm. The observations after assuming a k^{-1} slope lies close to a 1:1 line between the two sensors (Figure 3.4), with a best-fit slope of $k^{-0.92}$. The remaining scatter can be understood as a combination of noise and differences in water masses from the two sensors pointing in different directions. Note that the preferential values for backscatter at 470 nm, at intervals of approximately 10^{-5} m^{-1}, are due to the discreteness of the underlying dataset.

3.5 Results

Seasonality of chlorophyll and community index

Chlorophyll concentrations are confined to the mixed layer, defined here as the depth at which the density increases by 0.03 kg m^{-3} over the density at 10 m depth (de Boyer Montégut et al., 2004), except when the mixed layer is shallow, in which case high-chlorophyll waters extend to the depth of the euphotic zone at 50-100 m (Figure 3.5a) (Hemsley et al., 2015). Maximum values of chlorophyll

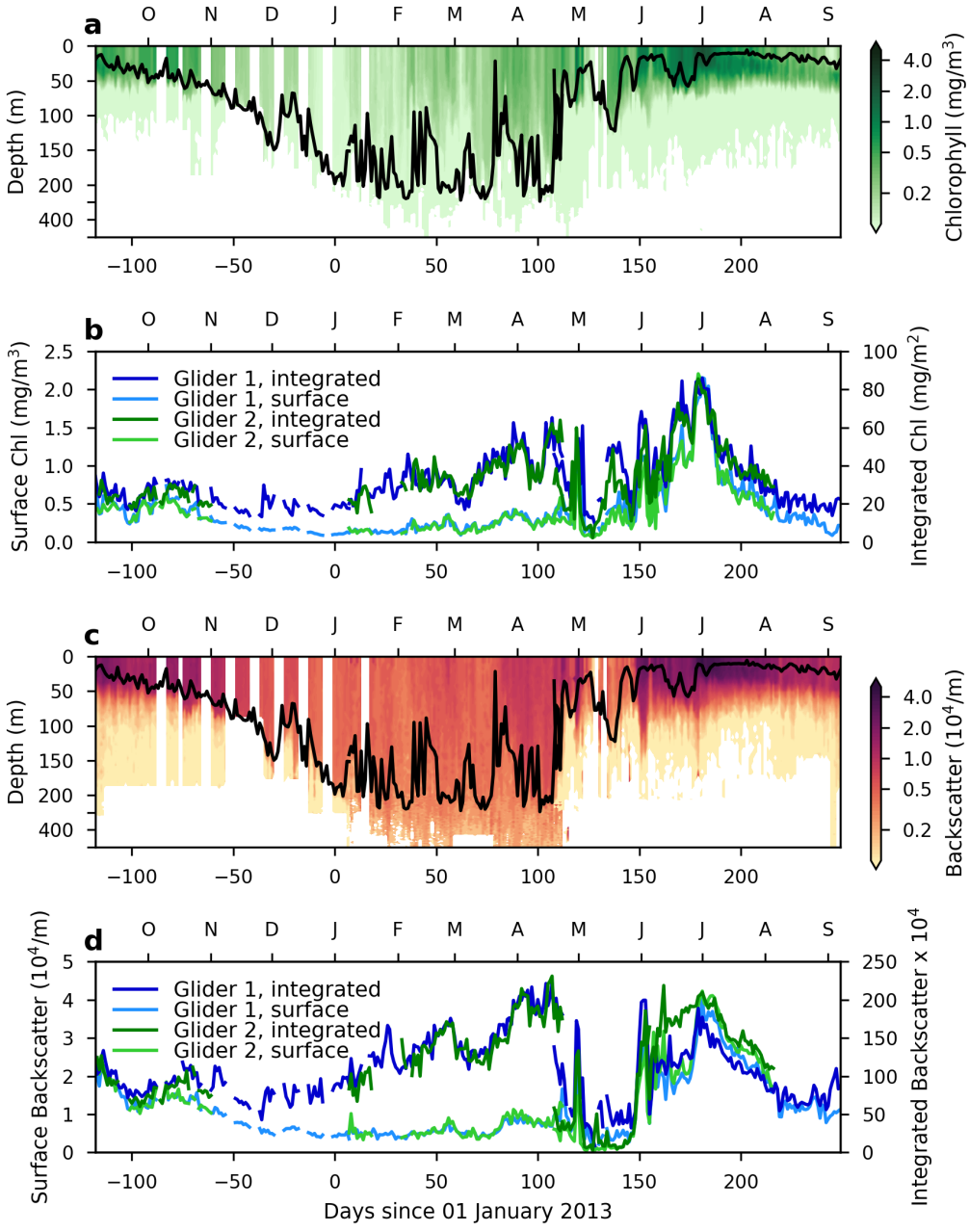

Figure 3.5: (a) Nighttime chlorophyll concentrations in the upper 500 m (note change in vertical scale at 200 m). (b) Average surface (upper 25 m) chlorophyll concentrations (blue) and total (upper 500 m) chlorophyll concentrations (green). (c,d) As in panels a and b, except for backscatter at 650 nm (see text). Black lines in (a,c) give the mixed layer depth.

($\sim$ 4 mg m^{-3}) exist near the surface in June and July. However, small chlorophyll concentrations persist within the mixed layer throughout winter (note the logarithmic colorbar). The surface average chlorophyll concentration (upper 25 m) is shown in panel b, as well as the integrated upper ocean chlorophyll (in the upper 500 m). Sporadic short-lived surface blooms occur throughout the winter, coincident with abrupt shoalings of the mixed layer. The final restratification event in April and May kicks off the spring bloom. After an initial burst of photosynthetic activity at the surface, chlorophyll concentrations are consolidated primarily within a sub-surface chlorophyll maximum just below the MLD, and production is maximized near the MLD (Hemsley et al., 2015). Although the gliders did not measure nutrient concentrations, this is consistent with an early depletion of surface nutrients followed by subsequent production at the nutricline, located slightly below the pycnocline.

The surface backscatter data is similar to that of fluorescence (Figure 3.5c), showing a dominant peak in June-July and smaller peaks in previous months. The interior backscatter concentrations, however, show a marked increase from December through mid-April, spanning multiple glider deployments (Figure 3.5d). If we assume a specific relationship between backscatter and POC, this could be interpreted as a build-up of POC over the winter months. However, since we do not have *in situ* calibration for any backscatter to POC conversion, we choose to work with the glider-derived backscatter measurements and focus our analysis on relative changes in this quantity.

Community composition

The composition of phytoplankton species is important in determining export potential, as the remineralization coefficient of aggregates varies widely (Berelson, 2001; Armstrong et al., 2001). Field experiments characterizing phytoplankton composition in this region have found a short-lived surface diatom bloom that evolves into a sub-surface chlorophyll maximum dominated by diatoms during early summer (Painter et al., 2010). A simple ratio of fluorescence to backscatter, also known as the optical "community index", is shown in Figure 3.6a. Cetinić et al. (2015) used this ratio to categorize phytoplankton species, with larger diatoms having a higher ratio than smaller picophytoplankton. We expect diatoms to flourish under high-nutrient conditions, such as during the springtime bloom and at the nutricline in the summer. While the community index approach does not take into account many other biological effects, the results from this simple analysis agree with expectations: high values (greens) where we expect high nutrients, mid-range values (reds) where

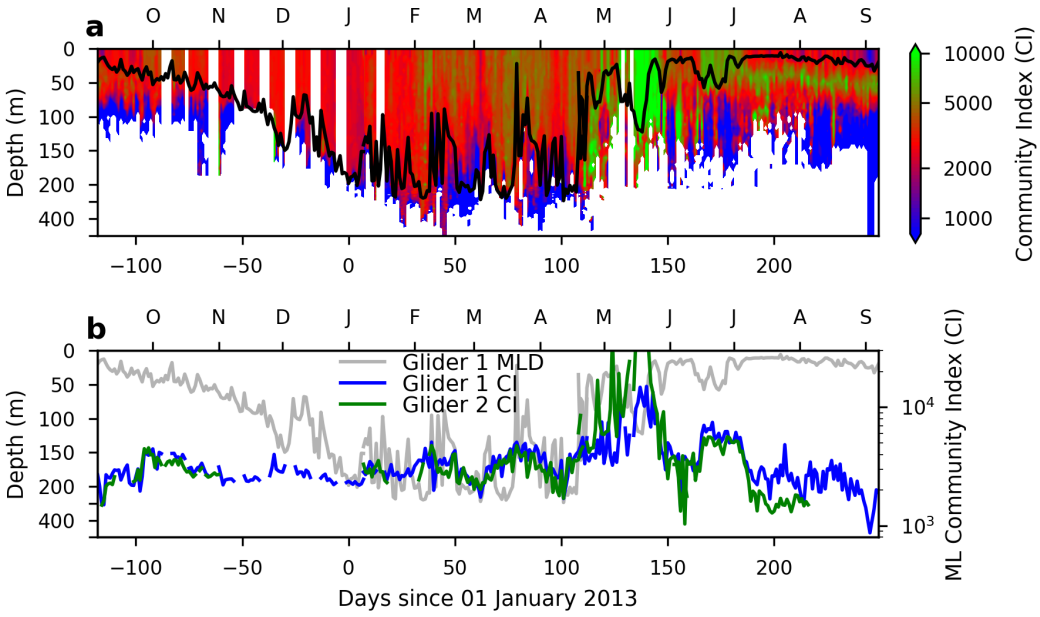

Figure 3.6: (a) Community index, defined as the ratio of chlorophyll to backscatter, in the upper 500 m (note change in vertical scale at 200 m). (b) Average ratio of chlorophyll to backscatter within the mixed layer. Black line in (a) and grey line in (b) show the mixed layer depth.

nutrients are scarce, such as during autumn and at the surface in summer, and low values (blues) where we expect no production (below mixed and euphotic layers).

The community index convolves information on community composition with other processes, such as photoacclimation, which can impact the amount of chlorophyll per unit biomass. Photoacclimation increases the concentration of chlorophyll and accessory pigments under low light conditions, and acts on a timescale of under a day (Neori et al., 1984). During the spring, the community index within the mixed layer is correlated with the MLD on short timescales (Figure 3.6b). For example, the deepening event in June is accompanied by increased fluorescence:backscatter ratios, consistent with the effects of photoacclimation. However, another mechanism potentially at work is an entrainment of nutrients into the mixed layer during mixed layer deepening events, which promote the growth of large species such as diatoms with high fluorescence:backscatter ratios.

Seasonality of PV and AOU

In Figure 3.7a we show PV in the upper 500 m of the water column for Glider 1. In calculating PV through Equation 3.3, we take u and x to be the velocity

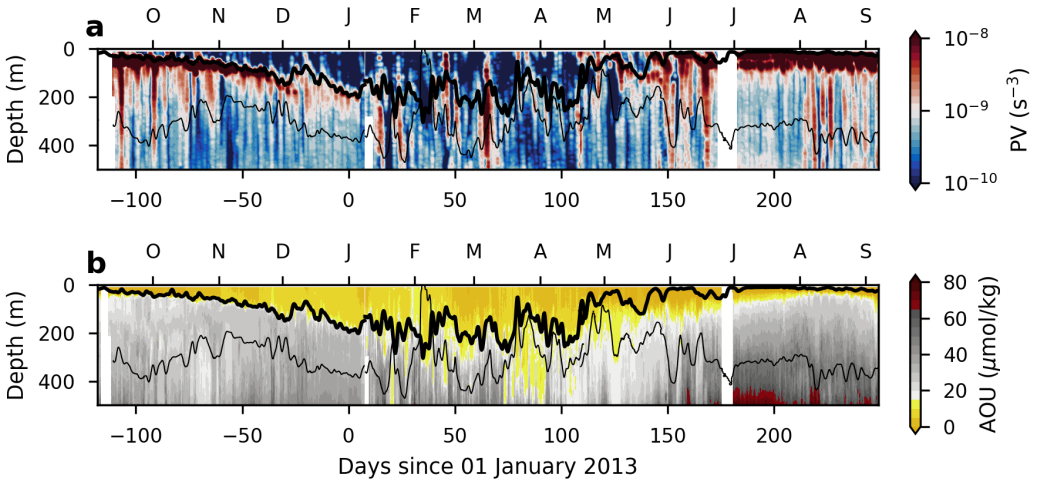

Figure 3.7: (a) Potential vorticity (PV), calculated as in Equation 3.3, and (b) apparent oxygen utilization (AOU), calculated as the difference between saturated and measured oxygen concentrations, from Glider 1. Thick black lines give the mixed layer depth, and thin black lines give the $\sigma_0 = 27.1$ kg m^{-3} isopycnal.

and direction, respectively, along the glider path. One-dimensional glider transects give no information about derivatives in y. One option is to assume $b_x = b_y$. In an approximately horizontally isotropic region such as is considered here, this approximation yields accurate average PV values. However, assuming $b_x = b_y$ increases the number of negative PV events beyond what is actually present. We instead conservatively approximate $b_y \equiv 0$, $M^2 \approx b_x$, and $\zeta = v_x$. This is likely to bias our final PV estimates positive and identify fewer negative PV events than actually occurred (see detailed discussion and analysis in Thompson et al. (2016)).

The waters above the MLD (thick black line) are low in PV (blue colors), reflecting primarily low vertical buoyancy stratification within the well-mixed part of the ocean. The base of the mixed layer is host to a strongly stable pycnocline (red colors) during June-November. During December the pycnocline erodes. Here we calculate the MLD using a threshold method of 0.03 kg/m^3 difference in density from the density at 10 m depth (de Boyer Montégut et al., 2004), which defines a wintertime mixed layer of 100-250 m. This definition is consistent with the chlorophyll concentrations, which become near-zero beneath this depth (Figure 3.5a). MLD calculated by this definition is also very similar to MLD calculated by a vertical density gradient of 5×10^{-4} kg m^{-4} (not shown) (Dong et al., 2008). However, the MLD is highly sensitive to the precise definition of mixed layer used,

and it may be more accurate to say that the base of the mixed layer is no longer well defined, because of the lack of a strong pycnocline within the upper water column.

The interior of the ocean below the pycnocline is also relatively low in PV. Isolated pockets of waters with very low PV are also present, the most prominent being at 100-300 m depth in early May. Since PV is conserved in the absence of frictional effects, we expect that these especially low PV waters were subducted from the mixed layer.

We test the hypothesis that low PV waters were subducted from the mixed layer using apparent oxygen utilization (AOU), the difference between saturated and measured oxygen concentration. AOU decreases with photosynthesis and increases with respiration, and is "reset" to zero when a water parcel comes in contact with the atmosphere. Thus, low (high) AOU values are characteristic of water that has (has not) been recently ventilated at the surface. AOU values are near-zero at the surface and within the mixed layer, and decrease slightly due to photosynthesis during the spring bloom in May-July (Figure 3.7b). AOU tends to increase with depth, but is low where PV is low, which suggests that these low-PV waters below the mixed layer have indeed been recently subducted.

Low-AOU waters (yellow colors) are found within the mixed layer from summer through early winter (September-January), but exist below the MLD in late winter and spring (February-June). Figure 3.8 shows PV and AOU on potential density rather than depth surfaces (to relate the two, the thin black line in Figure 3.7 is the 27.01 kg m^{-3} isopycnal, and the thin black line in Figure 3.8 is the 500 m isobar). Low PV values align along the 27.0-27.25 kg m^{-3} potential density surface, which is also the density of the mixed layer during winter. AOU values in this same potential density range decrease suddenly in the wintertime, and then slowly increase over time in the spring and summer. This increase of approximately 20 μmol kg^{-1} over 100 days is, however, much faster than typical oxygen utilization rates (Sarmiento et al., 1990), signifying the importance of horizontal advection (Hartman et al., 2010; Damerell et al., 2016). These results show subduction of passive tracers such as AOU during winter, and motivate the need for a better understanding of how these subduction processes interact with surface biological variables such as chlorophyll and backscatter.

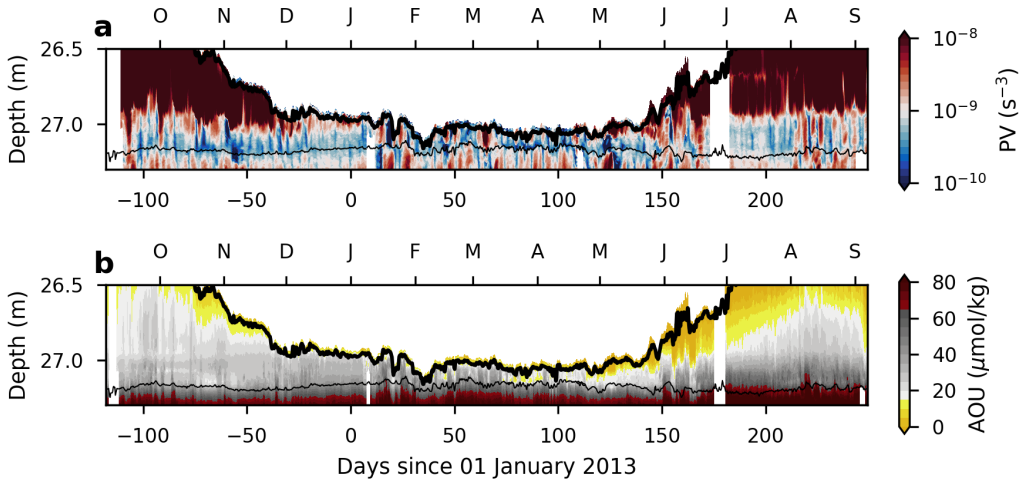

Figure 3.8: As in Figure 3.7, but on potential density surfaces rather than depth. Thick black lines give the MLD, and thin black lines are the 500 m isobar.

External forcing and submesoscale-instability export

An increase in sea surface temperature (SST) is associated with the spring restratification in MLD, but occurs well after the atmospheric heat flux becomes positive, indicating that surface heat flux is not the only factor contributing to the restratification (Figure 3.9a,b). The wind stress τ decreases throughout the spring from a maximum in winter. Increasing (decreasing) τ will deepen (shoal) the mixed layer, and indeed short-lived deepenings of the mixed layer in May and June correspond to increases in τ (Figure 3.9a).

Brannigan (2016) and Brannigan et al. (2017) predict that symmetric instabilities will be strongest near the periphery of anticylonic eddies. We use Sea Level Anomaly (SLA) measurements from AVISO (Archiving, Validation and Interpretation of Satellite Oceanographic data), where positive (negative) values of SLA correspond to cyclones (anticylones) (Figure 3.9c; black). The Okubo-Weiss parameter (OW) is shown in grey in Figure 3.9c, where

$$\mathrm{OW} = S_n^2 + S_s^2 - \zeta, \tag{3.7}$$

where $S_n = u_x - v_y$ and $S_s = v_x + u_y$ are the normal and shear components of strain. Regions in the center (periphery) of an eddy will have strongly negative (positive) OW (Henson and A. Thomas, 2008). Due to the low resolution (1/4°) of AVISO data, $|\mathrm{OW}| \ll f^2$; however, in reality, strong eddies will be associated with $|\mathrm{OW}|/f^2 \sim 1$. The OSMOSIS location encounters three prominent eddies (days

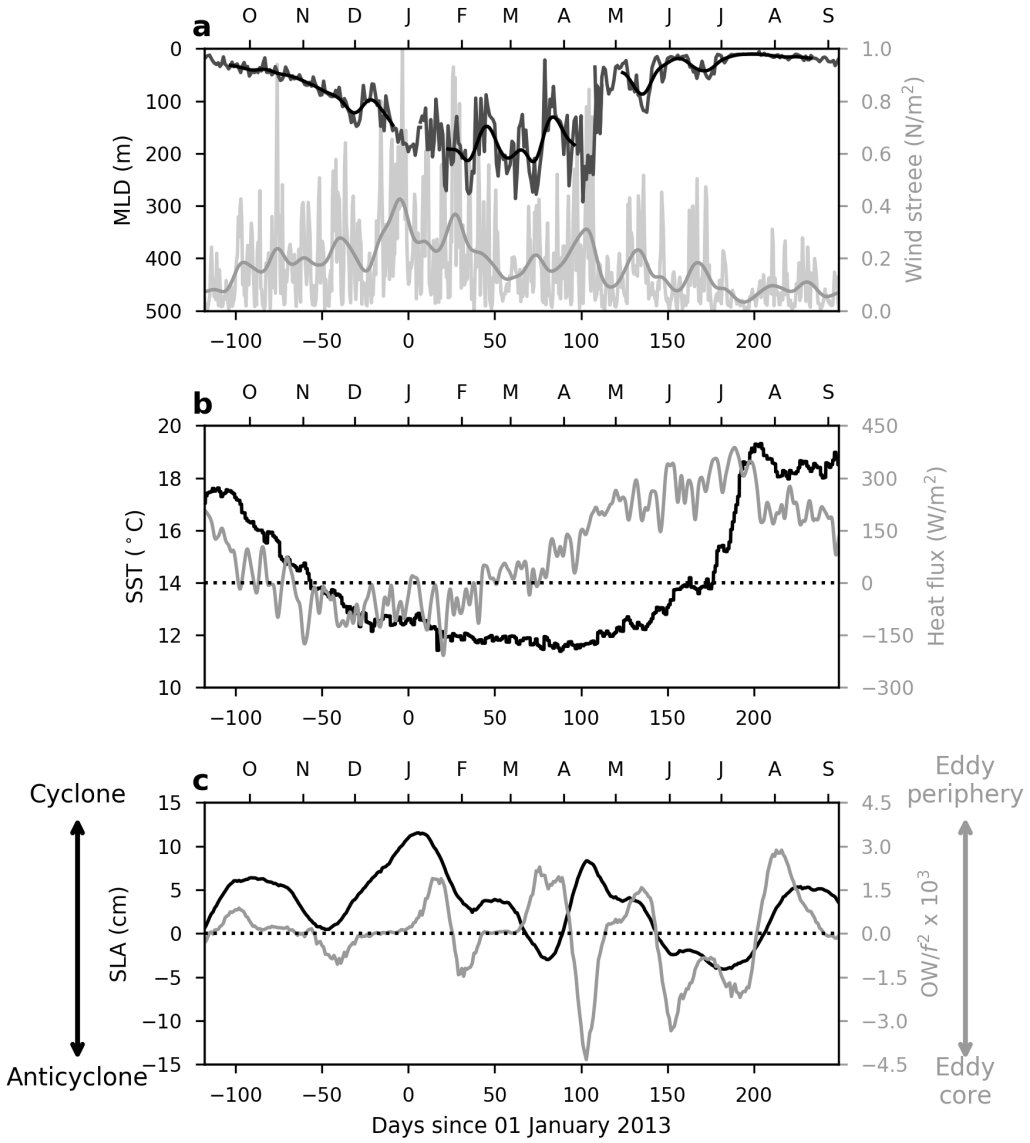

Figure 3.9: (a) MLD (dark grey) from Glider 1, and after filtering with a Gaussian window (standard deviation one day; black). Wind stress (light grey), and after filtering with a Gaussian window (standard deviation one day; grey). (b) SST (black) and total heat flux from the atmosphere (grey), both filtered with a Gaussian window with standard deviation of one day. (c) Sea Level Anomaly (SLA; black) and the Okubo-Weiss parameter (OW; Equation 3.7) scaled by f (grey). Wind stress, SST, and total heat flux from ECMWF ERA-interim re-analysis are shown as an average for values within a one degree by one degree box centered on the OSMOSIS location. SLA and OW from AVISO data at the pixel nearest the OSMOSIS location.

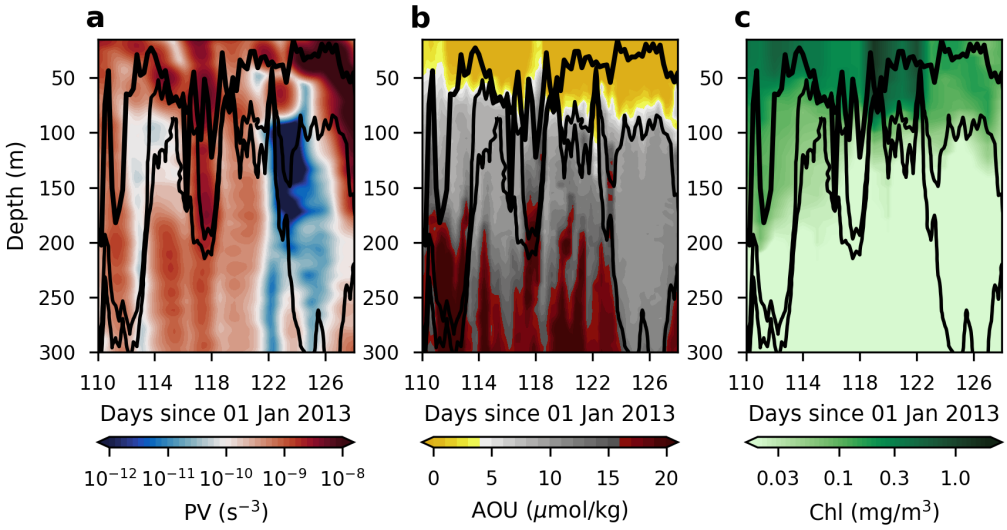

Figure 3.10: PV (a), AOU (b), and chlorophyll (c) from SG566 from 20 April to 08 May. Thick black line gives the MLD; thin black lines show isopycnals at $\sigma_0 = 27.09$ and $\sigma_0 = 27.1$ kg m^{-3}.

0 to 40, 90 to 110, and 150-200) throughout the year, of which the first two are cyclonic and the third anticyclonic. Smaller-scale eddies not captured by AVISO are likely also present.

A pronounced low-PV subduction event occurs in early May (Figure 3.7), when the OSMOSIS region is in the periphery of a cyclonic eddy. Figure 3.10 shows PV, AOU, and chlorophyll concentration for this event. The subduction feature is bounded by potential density surfaces at 27.09 and 27.1 kg m^{-3} (thin black lines). A subduction signal is clearly indicated in decreased PV and AOU, but is not present in the chlorophyll data (or backscatter; not shown), suggesting that this event did not correspond with export of fixed carbon out of the surface ocean.

3.6 Discussion

Event-level export

Which of the submesoscale instabilities outlined in Section 2, if any, are responsible for the subduction events observed over the winter period? The vertical velocity w_{MLI} associated with MLI (from Equation 5.1) for the time period before and during that shown in Figure 3.10 is given in Figure 3.11a. Large vertical velocities (> 20 m day^{-1}) associated with MLI are present throughout wintertime, but, by definition, go to zero at the base of the mixed layer. This no-normal-flow boundary condition at the mixed layer depth is due to the $\mu(z)$ term (Equation 5.2), which goes to zero

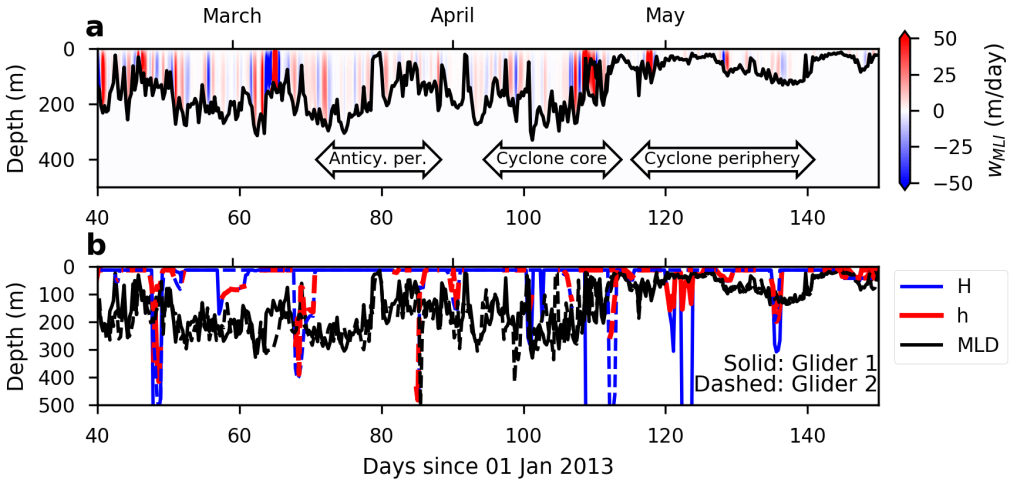

Figure 3.11: (a) Vertical velocity $w = \psi_x$ (Equation 5.1) associated with mixed layer instability. (b) Depths at which the water column is symmetrically unstable (H, blue line; Equation 3.6) and gravitationally unstable (h, red line; Equation 3.8). Solid (dashed) lines are from Glider 1 (2). Black lines in each panel give the mixed layer depth.

at the top and bottom of the mixed layer.

The characteristic depth over which turbulence occurs during an SI event is given by H, as determined through Equation 3.6, and is plotted in Figure 3.11b (blue line). As discussed in Section 2.3, H is the depth over which mixing must occur to bring PV back to marginal stability, i.e. PV = 0. The depth at which GI, or convection, occurs is given by the convective depth h (Figure 3.11b; red line), and is always less than H. The convective depth is solved using the quartic equation

$$\left(\frac{h}{H}\right)^4 - 14^3\left(1 - \frac{h}{H}\right)^3\left[\frac{w_*^3}{|\Delta u_g|^3} + \frac{u_*^2}{|\Delta u_g|^2}\cos\phi\right]^2 = 0, \tag{3.8}$$

where $h \leq H$, $w_* = (B_0 H)^{1/3}$ is the convective velocity, $u_*^2 = \sqrt{|\tau|/\sigma_0}$ is the friction velocity, $B_0 = F\alpha g C_p^{-1}\rho_0^{-1}$ is the surface buoyancy flux, ϕ is the angle between the wind vector and the geostrophic shear, which in this case is the glider orientation, F is the total heat flux, α is the thermal expansion coefficient, C_p is the specific heat of seawater, and Δ refers to the difference between the surface and $z = H$ (Taylor and Ferrari, 2010; L. Thomas et al., 2013). As GI is a diabatic process, a convective depth $h >$ MLD will result in mixed layer deepening and entrainment of new material into the mixed layer, while retaining surface tracers such as phytoplankton in the well-mixed region. Thus, $h >$ MLD is only possible transiently before the

mixed layer responds by deepening. Sporadic events occur where GI extends below the MLD (Figure 3.11b); we assume that these are associated with a deepening of the mixed layer and that GI does not contribute to export production.

Theoretically, surface buoyancy gain can form a new, shallow mixed layer that overlays a deeper, denser mixed layer. This capping effect can lead to export either through large-scale advection of this remnant water mass to deeper depths, or slow sinking of particles in this water mass (Carlson et al., 1994). At the OSMOSIS site, however, this effect does not seem to be dominant, as the major mixed layer shoaling events in April and May do not leave behind high-chlorophyll or high-backscatter waters (Figure 3.5a,c).

The SI depth H, however, often reaches below the MLD, and indeed a SI event takes place shortly before the most prominent subduction feature observed during the OSMOSIS time series (Figure 3.10). This points to SI as a primary candidate for export across the base of the mixed layer. The limited duration of the extreme H values shown in Figure 3.11b reflects the relatively short temporal and spatial scales over which SI events occur. This highlights the difficulty in observing SI, as these instabilities are quickly stabilized. MLI tends to occur over a longer time scale of days, but from the snapshot nature of the glider observations, it can be difficult to determine the stage of the instability. It is important to note that the diagnostics presented here provide a statistical representation of the submesoscale motions that are active in this region, but do not capture the life cycle of any individual instability process.

SI could give rise to the observed subduction features seen here (e.g. Figure 3.10), as it provides a clear mechanism for export below the mixed layer through entrainment of pycnocline and other sub-mixed layer waters into the mixed layer. SI also occurs on timescales of order hours, meaning the biological field can be well approximated as a passive tracer for this process, and the existence of symmetrically unstable waters extending below the mixed layer during winter is consistent with episodic injections of low-PV and low-AOU waters (Thompson et al., 2016), as is shown in Figure 3.10a,b. Unlike Brannigan (2016) and Brannigan et al. (2017), we do not observe a clear increase in SI events while the gliders are in the periphery of an eddy. However, the total number of events captured is small, so we cannot conclusively comment on this prediction.

Although SI is present during winter, MLI effects may also contribute to the subduction of mixed layer waters into the interior. At the OSMOSIS region, and in

many other mid-to-high latitude regions, a well-defined mixed layer base does not exist during wintertime, and MLI can produce vertical velocities that extend across the base of the mixed layer. Callies et al. (2016) show that the vertical decay scale of a tracer anomaly with wavelength k due to MLI is kN/f. If N decreases sharply at the MLD, this scaling drastically limits the vertical range at which MLI can extend below the mixed layer, but if N is small below the mixed layer substantial vertical penetration is possible.

As described above, an important aspect of this system is the coupled seasonal cycle of MLD and the stratification at the base of the mixed layer, and in particular the difference in these properties across the fall-winter and winter-spring transitions (Figure 3.12a). During winter, mixed layers are deep and vertical stratification at the base is small. This is shown schematically in Figure 3.12b, where the along-isopycnal movement of water due to MLI is indicated by the grey arrows. The combination of deep mixed layers, implying a large reservoir of available potential energy, and weak stratification, causing a weak vertical decay of vertical velocities, can lead to deep subduction of water masses through MLI. During the spring, the mixed layer shoals, but periodic de-stratification events keep the vertical stratification at the base of the mixed layer weak, and along-isopycnal motions can still lead to deep subduction. During summer, a strong pycnocline forms, and the mixed layer is shallow with a well-defined base (Figure 3.12c). This is the type of mixed layer that is well-parameterized by Eq. 5.1, with negligible export potential. Interestingly, during autumn the pycnocline is stronger than during spring (Figure 3.12a), limiting the potential for export during this season, even though the mixed layer is deepening and submesoscale motions in the mixed layer will be more energetic (Su et al., 2018). Thus, the vertical velocities at the base of the mixed layer, and particularly their decay into the interior of the ocean, need to be parameterized accurately based on the observed or simulated stratification to properly account for export by submesoscale motions.

Seasonal/annual export

There is increasing evidence that submesoscale motions are broadly active throughout the ocean and in particular in regions with strong spring blooms (e.g. the midlatitudes and subpolar gyre in the North Atlantic). Submesoscales are most active when mixed layers are deep, providing large reservoirs of available potential energy (Boccaletti et al., 2007; Su et al., 2018). The transition from deep to shallow mixed layer conditions can occur rapidly, on the order of one or two weeks, but the

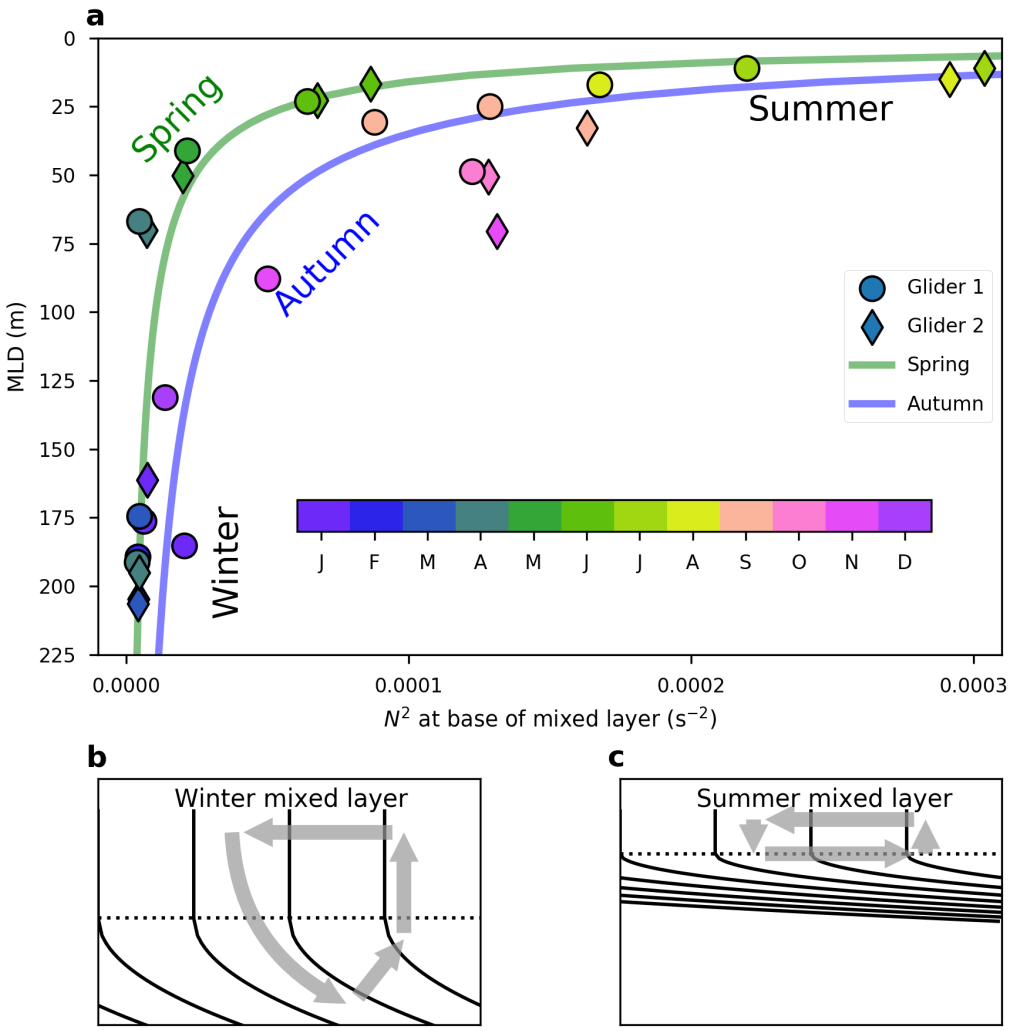

Figure 3.12: (a) MLD and vertical stratification at the base of the mixed layer as monthly averages for Glider 1 (circles) and Glider 2 (diamonds). The best-fit exponential for the winter-to-summer (summer-to-winter) transition is shown in green (blue). (b-c) Schematics for winter (b) and summer (c) surface ocean densities, where solid lines are isopycnal surfaces, dotted lines are the mixed layer depths, and grey arrows show the effect of MLI.

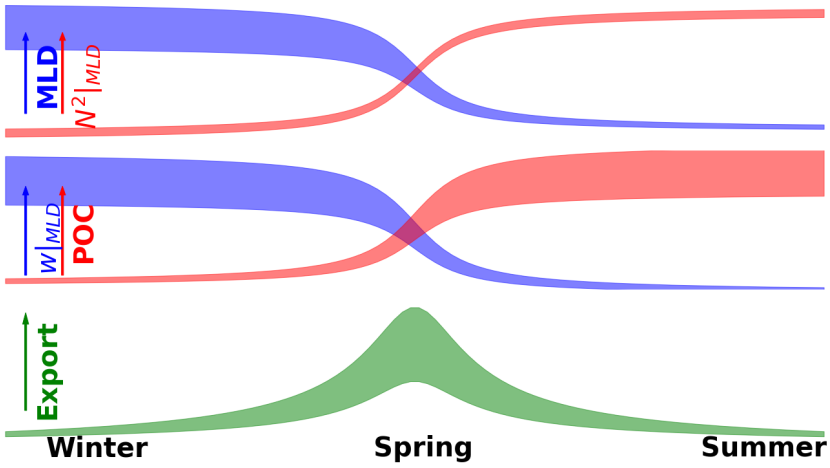

Figure 3.13: Schematic of the seasonal evolution of the MLD, the strength of the pycnocline (N^2 at the base of the mixed layer), the strength of vertical motions associated with submesoscale instabilities (w at the base of the mixed layer), POC concentrations, and export $\langle w'\text{POC}'\rangle$ throughout the year. The width of the curves represents the expected variance in these properties throughout the seasonal cycle. The typical timescale of the spring transition is of order weeks, but the time of year can vary widely.

transition may have different timing and duration from year to year. In addition, transient restratification events, as seen in the MLD during winter in Figure 3.5, may induce small-scale blooms that can be exported when the mixed layer deepens and submesoscale motions are enhanced.

A schematic for the large-scale seasonal evolution of export from submesoscale instabilities is shown in Figure 3.13. In the winter, mixed layers (blue, top) are deep and highly variable. Stratification at the base of the mixed layer, $N^2|_{\text{MLD}}$, is small, reflecting a weak pycnocline (red, top). These conditions both lead to the potential for large vertical velocities at the base of the mixed layer $w|_{\text{MLD}}$ through the submesoscale instabilities discussed in this paper (blue, middle). The winter is therefore a time of large amounts of subduction out of the mixed layer.

Export, however, requires fixed carbon to be present. As discussed in the introduction, bloom dynamics and POC concentrations are strongly inversely proportional to the MLD (Sverdrup, 1953); this is true in the OSMOSIS region as well, although we do show non-negligible amounts of fluorescence and backscatter during winter

(Figure 3.5a,b). In the spring and summer, fixed carbon concentrations, represented here as POC, increase (red, middle). Export mediated by submesoscale instabilities (Omand et al., 2015), which can be calculated as $\langle w'\mathrm{POC}'\rangle$ (green, bottom), is therefore highly dependent on the temporal overlap between submesoscale vertical velocities and POC concentrations.

Our results here suggest export rates due to physical processes at the OSMOSIS site in winter/spring of 2013 are low, although we do find evidence of subductive events. These observations are consistent with a relatively limited period of overlap between high vertical velocities and high POC concentrations. However, we emphasize that this study represents conditions at one particular location and one particular year. It would not be surprising to encounter different behavior in subsequent experiments, and there is clearly a need to find new ways to assess the overlap window between submesoscale instabilities and productivity over a broader range of conditions and across multiple years. Future studies could address this issue by measuring submesoscale motions and export properties (e.g. through thorium isotopes) in the late winter-early spring transition.

3.7 Conclusions

Data from the OSMOSIS project, using ocean gliders in the northeast Atlantic Ocean with biological and physical measurements, capture the full seasonal cycle of mixed layer and export variability at submesoscale resolution. In 2012-13, a spring bloom occurs in May-June following a shoaling of the mixed layer; however, the timing of this bloom varies widely from year to year. Shorter re-stratification events occur as well throughout winter and may help to maintain phytoplankton populations. We consider the potential for subduction of water masses out of the surface ocean and associated export of fixed carbon from mixed layer, gravitational, and symmetric instabilities. Mixed layer instability may be important, but accurately parameterizing its effects on subduction and export requires knowledge of the strength of the vertical stratification at the base of the mixed layer. Gravitational instabilities are important in determining the depth of the mixed layer, but do not directly induce meaningful export. Symmetric instability is active in this region during winter, and provides a clear mechanism for subduction of water masses from the surface; however, due to the highly episodic nature of this instability it is difficult to assess its contribution to total export.

Although we found instances of subduction of water masses, we did not find evidence

for substantial export of fixed carbon via this subductive route. Export through submesoscale instabilities requires both the production of unstable water columns and high fixed carbon concentrations at the surface. From this analysis, the influence from submesoscale motions at this location on export is small due to a limited overlap between strong vertical velocities across the base of the mixed layer associated with submesoscale instabilities, which are largest during winter, and fixed carbon concentrations in the surface of the ocean, which are largest in spring and summer. We point to the need for future work targeting this overlap window in other regions of the ocean.

Chapter 4

AN ADVECTIVE MECHANISM FOR DEEP CHLOROPHYLL MAXIMA FORMATION IN SOUTHERN DRAKE PASSAGE

4.1 Abstract

We observe surface and sub-surface fluorescence-derived chlorophyll maxima in southern Drake Passage during austral summer. Backscatter measurements indicate that the Deep Chlorophyll Maxima (DCMs) are also deep biomass maxima, and euphotic depth estimates show that they lie below the euphotic layer. Sub-surface, off-shore and near-surface, on-shore features lie along the same isopycnal, suggesting advective generation of DCMs. Temperature measurements indicate a warming of surface waters throughout austral summer, capping the Winter Water (WW) layer and increasing off-shelf stratification in this isopycnal layer. The outcrop position of the WW isopycnal layer shifts onshore, into a surface phytoplankton bloom. A lateral potential vorticity (PV) gradient develops, such that a down-gradient PV flux is consistent with offshore, along-isopycnal tracer transport. Model results are consistent with this mechanism. Subduction of chlorophyll and biomass along isopycnals represents a biological term not observed by surface satellite measurements which may contribute significantly to the strength of the biological pump in this region.

4.2 Introduction

The oceans account for approximately half of global photosynthesis (Field et al., 1998), yet productivity estimates are poorly constrained (Carr et al., 2006). High-latitude regions ventilate the deep ocean and contribute to carbon sequestration on long time scales (Sarmiento and Toggweiler, 1984; J. Martin, 1990; Broecker et al., 1998). High-nutrient low-chlorophyll (HNLC) conditions prevail over much of the Southern Ocean, where primary production is thought to be limited by the availability of iron and light (J. Martin, 1990; Boyd and Ellwood, 2010; Cassar et al., 2011). The Southern Ocean is a source region for non-anthropogenic carbon dioxide due to inefficient photosynthesis (Gruber et al., 2009). Locally, however, convergence of micronutrients can lead to large chlorophyll blooms, as in Drake Passage (Measures et al., 2013; Frants et al., 2013).

Deep chlorophyll maxima (DCMs) are an important component of the biological pump, accounting in some cases for over half of depth-integrated primary production

and export production (Hood et al., 1991; Weston et al., 2005; Omand et al., 2015). DCMs are generally considered in a one-dimensional framework (Cullen, 2015), where they have been attributed to photoacclimation processes (Cullen, 1982; Neori et al., 1984; Longhurst and Harrison, 1989), formation of thin phytoplankton layers driven by straining processes, vertical migration, and buoyancy control (Ralston et al., 2007; Richardson and Cullen, 1995; Stacey et al., 2007), and sub-surface production maxima caused by co-limitation of photosynthesis by light and nutrients (Mitchell et al., 1991; Holm-Hansen and Mitchell, 1991). Holm-Hansen and Hewes (2004) studied these features in the Western Antarctic Peninsula (WAP) region in southern Drake Passage and found evidence of a persistent DCM. They suggested the bloom was sustained by *in situ* biological growth, and linked biological production to an observed increase in oxygen concentration at the depth of the DCM.

In contrast, other studies have pointed to allochthonous origins of DCMs through subduction of water masses. Hood et al. (1991), Kadko et al. (1991), and Washburn et al. (1991) used ship-based observations to show subduction of biomass along isopycnals in narrow filaments off the coast of California. The subducted features were high in chlorophyll concentration but located beneath the euphotic layer (Hood et al., 1991; Washburn et al., 1991). Particle size distributions (Hood et al., 1991) and radium isotope measurements (Kadko et al., 1991) both indicated that the subducted features had been produced over a time period of hours to days. Recently, Omand et al. (2015) found strong evidence of eddy-driven subduction of particulate organic carbon along isopycnals in the North Atlantic, and estimated that this process may account for half of the total biological export in the Southern Ocean. Model results from this study highlighted the importance of submesoscale (1-10 km) dynamics in these subduction events.

Along-isopycnal subduction can be broken into submesoscale ageostrophic and mesoscale geostrophic components. Fronts at the submesoscale induce an ageostrophic circulation with associated vertical velocities of tens of meters per day (Lapeyre et al., 2006; Mahadevan and Tandon, 2006; Lévy et al., 2012; Rosso et al., 2014). At larger scales, mesoscale eddies mix properties along isopycnals. Eddies are generated in frontal systems, and are ubiquitous in the Drake Passage region (Frenger et al., 2015).

Here, we use ocean glider observations to show the development of a DCM in southern Drake Passage. We provide evidence that this development is affected by physical processes, and propose a mechanism by which eddy mass fluxes associated

with a potential vorticity (PV) gradient subduct surface waters with high chlorophyll and/or high micronutrient concentrations. Our data and methods are given in Section 2. Results are summarized in Section 3, and a discussion and conclusions are in Sections 4 and 5.

4.3 Data and Methods

Deployment site

Drake Passage is a choke point in the Southern Ocean, where the Antarctic Circumpolar Current (ACC) funnels through a gap of only 800 kilometers, leading to high velocity shear, strong frontal systems, and a vigorous eddy field. The continental slope generates persistent, topographically-steered fronts along the southern boundary, similar to other areas of the Southern Ocean such as the Kerguelen and Campbell Plateaus (Zhou et al., 2010; Sokolov and Rintoul, 2009; Thompson et al., 2010; Rosso et al., 2015; Frenger et al., 2015).

Our study area is in southern Drake Passage, upstream of the Shackleton Fracture Zone (SFZ; Figure 4.1a). This region contains the Southern Boundary of the ACC (SBACC) and the Southern ACC Front (Orsi et al., 1995; Sokolov and Rintoul, 2009), which are strongly steered by topography (Zhou et al., 2010), being channeled through the Shackleton Gap and northward around the SFZ, respectively. A surface bloom in this area occurs in austral summer and is associated with the shelf break (Holm-Hansen et al., 2005). This area is one of the major HNLC regions, where growth is thought to be co-limited by light and iron (J. Martin et al., 1990; Dulaiova et al., 2009), and is upstream from the highly productive Scotia Sea. Waters sourced from the shelf or nearby Bransfield Strait may supply crucial micronutrients to the region (Measures et al., 2013).

Seaglider data

We use three months of high-resolution data from an autonomous, buoyancy-driven Seaglider during austral summer (December 2014 to March 2015) as part of the ChinStrAP (Changes in Stratification at the Antarctic Peninsula) project. The glider followed a saw-tooth pattern to 1000 m depth, with average spacing between dives of 3-5 km. Measurements were taken of temperature (T), salinity (S), and pressure (p) with a Sea-Bird CTD Sail, oxygen (O_2) with an Aanderaa optode, and fluorescence (F), backscatter (b_{bp}) at 650 nm, and CDOM (colored dissolved organic matter) with a WETLabs ECOPuck Triplet.

Fluorescence is a widely used proxy for chlorophyll-*a* (Chl) and, often, for phyto-

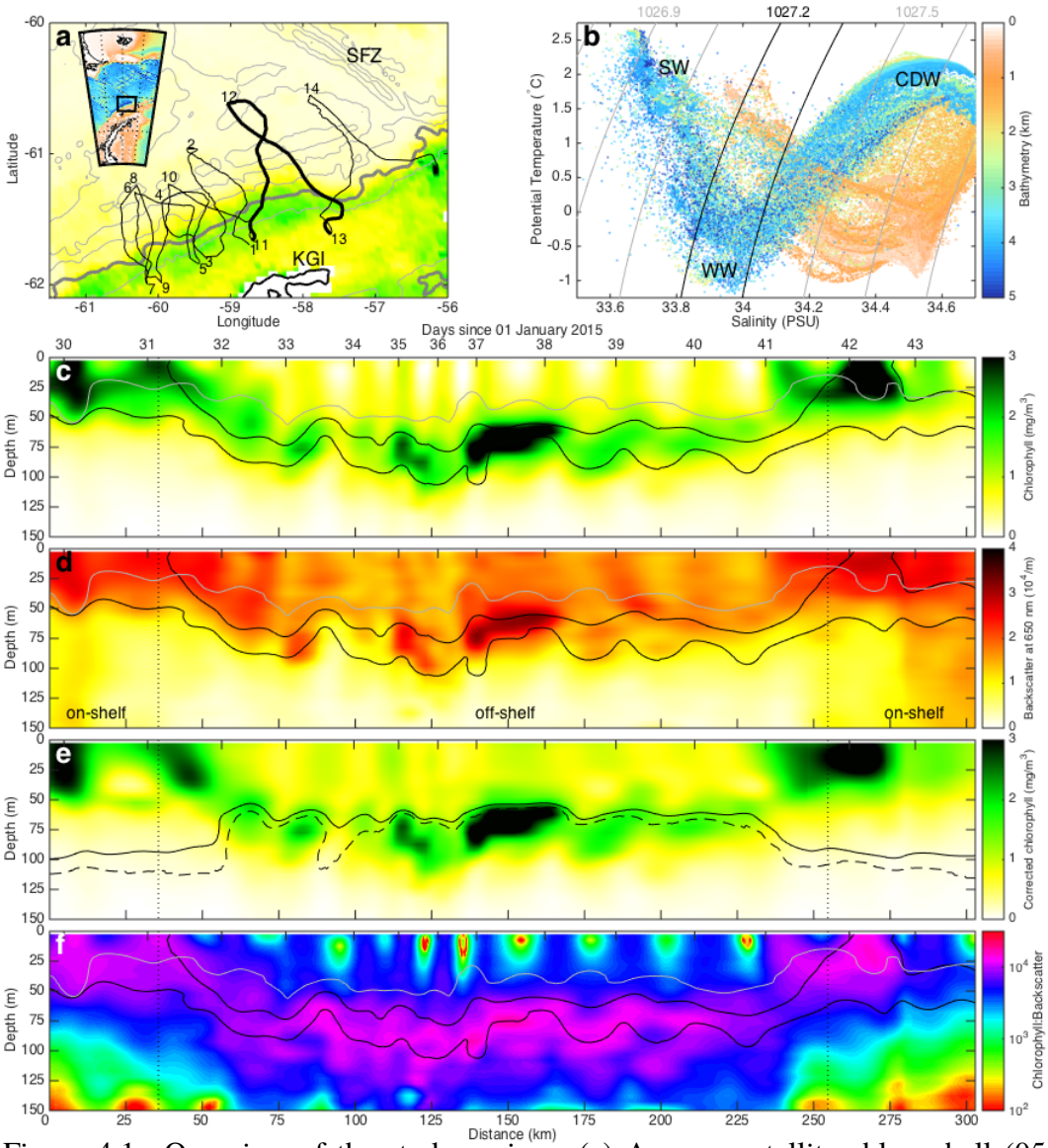

Figure 4.1: Overview of the study region. (a) Average satellite chlorophyll (05 Dec 2014 to 02 Mar 2015) from MODIS Aqua, using the Johnson et al. (2013) algorithm with colorbar as in (C), with bathymetry contours every 1 kilometer (grey) and glider transects (black). Inset shows the region in a larger context with bathymetry colorbar as in (B). Shackleton Fracture Zone (SFZ) and King George Island (KGI; black contour) are labeled. (b) Temperature-salinity plot of Transects 1-14; colors denote bathymetry. Circumpolar Deep Water (CDW), Winter Water (WW), and Surface Waters (SW) are labeled, and isopycnal contours (kg/m^3) are overlain in grey and black. (c-f) Objectively mapped chlorophyll, backscatter, corrected chlorophyll, and the chlorophyll:backscatter ratio from Transects 11 and 12 (bold line in **a**). Isopycnal contours at 1027.2 and 1027.35 kg/m^3 in black are shown in (c,d,f). Mixed layer depth is given in grey in (c,d,f). Black solid (dashed) line in (e) gives the euphotic depth, defined as the 1% light level (0.1 mol/m^2/day isolume). Dotted vertical black lines in (c-f) give the location of the 2000 meter isobath.

plankton biomass. The scale factor relating fluorescence and chlorophyll concentration (F:Chl) was determined in a factory calibration with a *Thalassiosira weissflogii* diatom mono-culture. This scale factor is highly dependent on a range of factors, including community composition and structure (Cullen, 1982; Boss et al., 2008) and nutrient and light stress (Slovacek and Hannan, 1977; Neori et al., 1984), which can vary over small spatial and temporal scales (Cullen, 1982; Boss et al., 2008). We compared nighttime surface fluorescence-derived chlorophyll measurements to remotely-sensed chlorophyll concentrations from MODIS Aqua and found good agreement with the factory calibration.

During daytime, the ratio F:Chl decreases at the surface due to an array of photoadaptative processes collectively known as nonphotochemical quenching (NPQ) (Cullen and Lewis, 1995). A common NPQ correction relies on a constant ratio between backscatter and fluorescence measurements below the surface in the mixed layer (Boss et al., 2008; Boss and Haëntjens, 2016). This method was used to generate our "NPQ-corrected chlorophyll" results.

More information on the processing, calibration, and NPQ-correction methods are given in the Supplementary Text. We note that *in situ* calibration steps during the bloom were not available due to the autonomous nature of our sampling, and emphasize that our results are primarily dependent on the relative spatial and temporal distribution of the Chl or biomass concentrations as opposed to their absolute values.

Mixed layer depth calculations

We calculate the mixed layer depth (MLD) as the depth at which the potential density differs by a threshold value of 0.03 kg/m^3 from the potential density at 10 meters depth (Dong et al., 2008).

Euphotic depth calculation

We adapt the method given in Arrigo et al. (2008) to estimate the propagation of photosynthetically available radiation (PAR; 400-700 nm) through the water column. Our approach differs from that of Arrigo et al. (2008) in that we use depth-resolved glider chlorophyll concentrations, ozone measurements from NASA OMI (Ozone Monitoring Instrument),s ea level pressure and wind data from the Antarctic Mesoscale Prediction System (AMPS), and choose a relatively clear visibility of 12 km. We use the NPQ-corrected chlorophyll results in order to estimate light propagation during daytime measurements.

The euphotic depth is often taken as the depth at which 1% of surface PAR is available (e.g. Ryther (1956), Behrenfeld and Falkowski (1997), and Dunne et al. (2005)). Because phytoplankton respond to absolute rather than relative light levels, the 1% PAR threshold may not be the best measure of the euphotic depth (Banse, 2004). Holm-Hansen and Mitchell (1991) estimate the euphotic depth in this region at approximately the 0.1 mol quanta/m^2/day isolume. We estimate this depth by correcting solar irradiance for cloud cover as in Arrigo et al. (2008) using daily-averaged AMPS cloud fraction and calculating daily insolation from hourly estimates of PAR.

Satellite measurements

We include in our analysis satellite observations of surface chlorophyll from the MODIS Aqua platform at 4 km resolution using the Johnson et al. (2013) algorithm. This method updates the reflectance ratio coefficients using only Southern Ocean measurements, showing substantially larger amounts of chlorophyll in the Southern Ocean than the standard global algorithms (Mitchell and Holm-Hansen, 1991; Kahru and Mitchell, 2010). We temporally average the results by taking the mean value over all days with valid observations. Satellite imagery produces values representative of ocean conditions within about one optical depth of the surface, which for 550 nm light is approximately 20 meters (Gordon and McCluney, 1975), but can be highly dependent on seawater constituents (Arrigo et al., 1998).

Southern Ocean model

To test the advective hypothesis, a 1/12° simulation of the Southern Ocean was run using the MITgcm (Marshall et al., 1997). The domain is 78°S to the equator, with lower resolution north of 30°S. Topography is prescribed using ETOPO1 (Amante and Eakins, 2009). The model has 104 vertical levels with partial bottom cells. An atmospheric boundary layer scheme is employed where fluxes of heat, freshwater (salt), and momentum are determined by bulk formulae (Large and Yeager, 2009). The atmospheric state is prescribed from the ERA-Interim reanalysis. Runoff is prescribed at the continental boundary. Initial conditions are derived from a 1/6° Southern Ocean state estimate (Mazloff et al., 2010). The model is run from 2005 to 2010, with a one-year spin-up to the increased resolution. We analyze model results from austral summer 2008-09, but our analysis is not strongly dependent on the year considered.

4.4 Results

We consider fourteen glider transects that are roughly perpendicular to bathymetric contours (Figure 4.1a). We define glider dives as being south (on-shore) or north (off-shore) of the SBACC, which is well approximated by the 2000 meter isobath. This isobath is also the approximate limit of the surface phytoplankton bloom, as shown by satellite measurements.

Temperature/salinity properties in our area show the presence of a strong frontal system associated with the SBACC (Figure 4.1b).

Chlorophyll distribution

The vertical distribution of fluorescence tracks the growth of both an on-shelf surface-intensified chlorophyll bloom and a DCM. Interpolated chlorophyll data for Transects 11 and 12 are shown in Figure 4.1c. The on-shelf bloom is coincident with the chlorophyll levels observed from satellite. This bloom reaches approximately 50 meters depth and is bounded by the mixed layer.

The DCM develops soon after the surface bloom and is of a similar magnitude, but centered beneath the mixed layer at 50-90 meters depth. It lies along the same isopycnal as the surface bloom (black lines in Figure 4.1c) and, importantly, is not found until after the surface bloom is expressed and the isopycnal layer outcrop location migrates onto the shelf. An off-shelf bloom is not shown in satellite observations at any point throughout the glider deployment.

DCMs can result from an increase at depth of phytoplankters or from an increase in the chlorophyll:biomass ratio in phytoplankton at depth through photoacclimation. In Figure 4.1d we provide backscatter data (650 nm) from the same two transects. Backscatter provides a measure of the concentration of total particulate matter in the ocean, and is well-correlated with phytoplankton concentration in the open ocean (Boss et al., 2008). In these example transects, the combination of high fluorescence measurements and high backscatter provides strong evidence that there exists a layer of elevated phytoplankton concentration below the mixed layer.

We also consider the relation of the DCM to the euphotic layer depth, shown as the solid (1% of surface PAR) and dashed (isolume method) black lines in Figure 4.1e (see section 4.3). Both definitions show that the DCM is located below the euphotic layer, although we note that the light attenuation coefficient is strongly dependent on water column chlorophyll concentration, meaning we cannot rule out the possibility that available light may allow net photosynthesis at the top of the DCM.

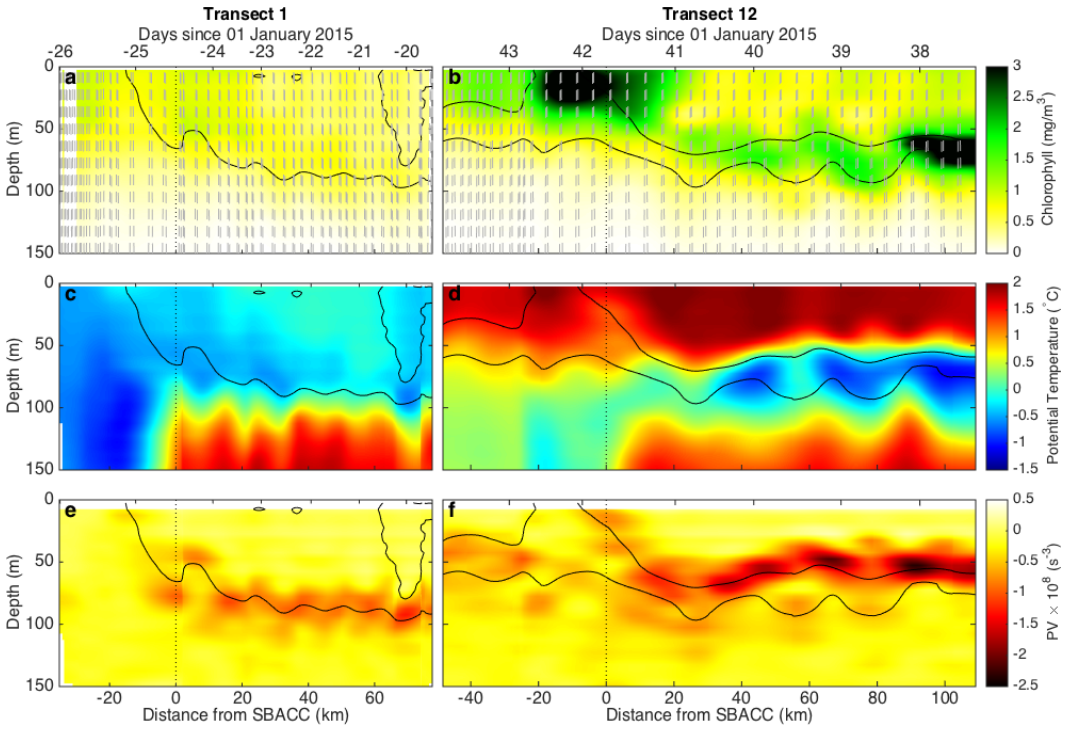

Figure 4.2: Winter water capping and development of an along-isopycnal PV gradient. (a,b) Objectively mapped corrected chlorophyll measurements for Transects 1 and 12. Isopycnal contours at 1027.2 and 1027.35 kg/m^3 are shown in black. Glider path is given by the grey dashed line. Distance is determined from the 2000 m isobath, where negative values are closer to the coast. (c,d) As in (a,b), but colors shown are potential temperature data from Transect 1 and 12. (e,f) As in (a,b), but colors shown are PV.

Subduction through thickness fluxes

In Figure 4.1 we highlight the isopycnal layer between 1027.2 and 1027.35 kg/m^3, which at depth is associated with the Winter Water (WW) layer. In spring and early summer, WW extends to the surface and stratification (lateral and vertical) is weak. Low biomass is observed throughout the region, presumably caused by light limitation (Figure 4.2a). The outcrop area of the WW isopycnal is large in extent and reaches off the shelf into the open ocean. As summer progresses, increasing insolation fuels an on-shelf phytoplankton bloom (Figure 4.2b) and warms the upper $\sim$ 50 meters of the water column, capping the existing WW layer (Figure 4.2c,d). The WW isopycnal layer deepens and thins, increasing the vertical stratification in the upper 50-70 meters. The meridional extent of the WW isopycnal outcrop decreases and moves poleward onto the shelf.

A widely used ocean tracer is potential vorticity (PV), which is conserved in the

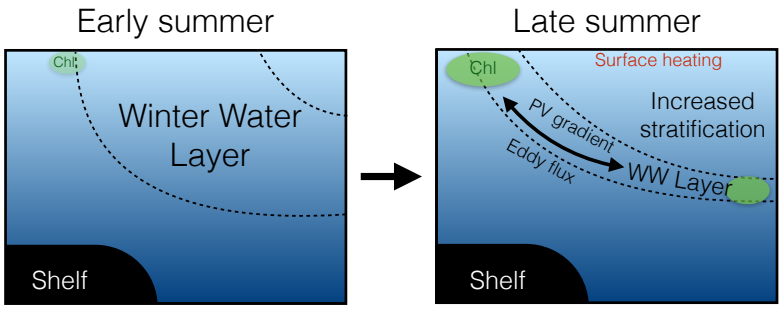

Figure 4.3: Schematic of mechanism generating off-shelf DCMs.

ocean interior where diabatic processes are weak. In the presence of a mesoscale or submesoscale eddy field, eddy fluxes tend to reduce the PV gradient, homogenizing PV along isopycnal layers (Marshall et al., 1993). We approximate PV as

$$q \approx (f^2 N^2 - M^4)/f, \tag{4.1}$$

where f is the planetary vorticity, $N^2 = \partial_z b$ is the vertical stratification, $M^2 = \nabla_h b \approx \partial_y b$ is the horizontal stratification, ∇_h is the horizontal gradient operator, and we consider only the along-track cross-frontal component (y-axis) (Thompson et al., 2016). The vertical stratification term (N^2) dominates the PV equation in most cases, although at frontal regions the horizontal stratification (M^2) becomes important.

PV (Equation 4.1) is shown for two transects in Figure 4.2e,f. An along-isopycnal gradient in PV develops in late summer just north of the SBACC. The reduction of the PV gradient is associated with an eddy thickness flux that produces an eddy velocity (defined below) transporting tracers offshore (Marshall and Radko, 2003). In the case of a surface bloom, eddies will subduct high biomass water to depth along the WW isopycnal layer (Figure 4.3).

4.5 Discussion

Scaling arguments

We propose that eddies in our study region will produce an off-shore mass transport, consistent with a down-gradient PV flux. This mechanism can be considered in two stages: vertical velocity w associated with submesoscale ageostrophic circulations in frontal regions, and along-isopycnal mixing through mesoscale motions.

We estimate w using the mixed layer restratification streamfunction from Fox-

Kemper et al. (2008),

$$\psi_{ML} = \frac{C_e H^2 M^2 \mu(z)}{|f|}, \quad w = \psi_y, \tag{4.2}$$

where C_e is an empirically-derived scaling constant, H is the mixed layer depth, and $\mu(z)$ is a dimensionless constant such that $0 \leq \mu(z) \leq 1$. Scaling arguments give

$$w \sim \frac{C_e H^2 M^2 \mu(z)}{|f|L} \sim \frac{(0.1)(50\text{ m})^2(10^{-6}\text{ s}^{-2})(1)}{(10^{-4}\text{ s}^{-1})(10^4\text{ m})} \sim 25\text{ m/day}, \tag{4.3}$$

which agrees well with typical submesoscale-induced vertical velocities of $O(10$ m/day) (e.g. Lévy et al. (2012)), and gives a subduction timescale of approximately 2 days.

To estimate a timescale for mesoscale, along-isopycnal advection, we use a high resolution (1/12°, approximately 4.5 km at this latitude) Southern Ocean model (Section 4.3) to calculate the thickness-weighted velocities in the WW isopycnal layer (Marshall and Radko, 2003). We directly calculate the residual velocities

$$\overline{\mathbf{u}}^{*} = \frac{\overline{\mathbf{u}h}}{\overline{h}} = \overline{\mathbf{u}} + \frac{\overline{\mathbf{u}'h'}}{\overline{h}}, \tag{4.4}$$

where $\mathbf{u} = (u, v)$ and primes are deviations in temporal averages (overbars), associated with a given isopycnal layer of thickness h. The total and eddy residual velocities perpendicular to the continental shelf for the isopycnal layer 1026.9 – 1027.1 kg/m^3 during the summer of 2008-09 are shown in Figure 4.4. We choose this isopycnal layer because its outcrop location approximately matches that of the WW layer in our data; however, our results are not dependent on the exact isopycnal layer or the model year used.

The residual velocities are dominated by the mean term, and show a meandering front that largely follows contours of constant f/H (where H is full ocean depth; Figure 4.4a). Large off-shelf velocities near the shelf break at 63°W are due to conservation of PV downstream of a bathymetric ridge. The total velocity also includes a large along-slope term (not shown). The eddy component, while smaller, consistently transports water off-shelf throughout this density layer (Figure 4.4b).

Using a characteristic eddy velocity of 0.05 m/s, we estimate that eddy-driven transport across the front could transport high chlorophyll waters approximately 100 km offshore (Figure 4.1c) in about 20 days. The mean velocity transport mechanism includes a large along-slope component. Using a characteristic mean velocity of 0.2 m/s and a length of 150 km gives an estimate of mean-flow transport across the front of 8 days. We expect both mean and eddy components to contribute to the offshore DCM, emphasizing the three-dimensionality of the system.

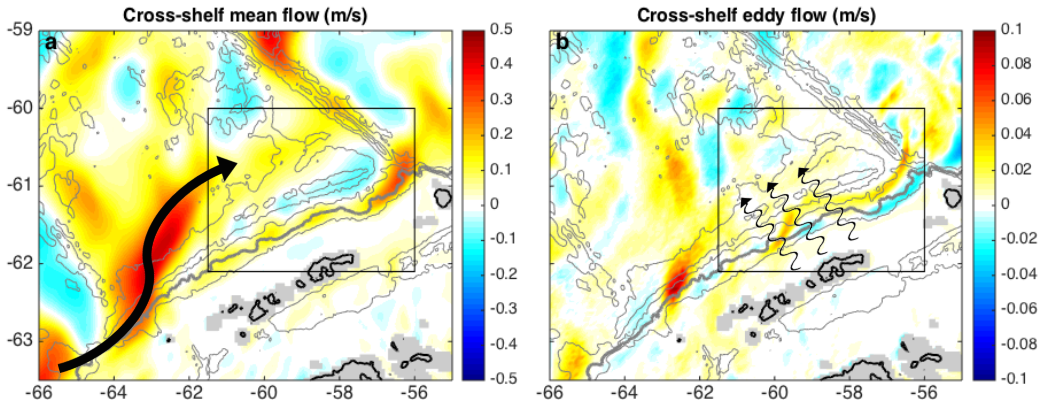

Figure 4.4: Layer-wise velocities from the Southern Ocean model. Mean (a) and eddy (b) residual velocities for 15 Nov 2007 to 15 Apr 2008 in the isopycnal layer 1026.9-1027.1 kg/m^3. Bathymetric contours at 1 km intervals are shown in grey (2 km bold), and black box gives domain of Figure 4.1a. Arrows give a general sense of the flow.

T-S properties

Although the DCM lies in the same isopycnal layer as the surface bloom, the T-S properties are distinct. The strong frontal system in this area separates water masses, but infilling of properties is also observed, indicating the presence of small-scale, irreversible mixing (Figure 4.1b). Recently, Klymak et al. (2016) observed submesoscale-induced mixing across the Gulf Stream, where "streamers" of water masses with drawn-out T-S properties are subducted along isopycnals. They used Lagrangian drifters to track streamers as they detrained from the Gulf Stream. Daily snapshots of salinity data along an isopycnal surface from the model suggest that streamers are also present here, as a strong frontal feature associated with the SBACC is present along with strong eddy activity across this front.

Biological considerations

DCMs in this area have generally been attributed to biological production. Holm-Hansen and Hewes (2004) conclude that they are the result of positive net community production, in part due to increased oxygen concentration in DCM locations. We note that oxygen saturation is the appropriate variable due to temperature effects on solubility, and do not observe a maximum in this quantity at the depth of the DCM. However, the oxygen released through net community production of the scale of this DCM is small compared to the spread in oxygen measurements, and ventilation of near-surface waters through wind-driven mixing means a large accumulation of

oxygen at this depth is unlikely. Oxygen data therefore provides neither evidence for, nor against, our hypothesis.

The DCM lies mainly below the euphotic depth, and is co-incident with a maxima in backscatter, suggesting that it is not simply a result of photoacclimation. The thickness of the DCM layer is greater than the typical thickness of thin phytoplankton layers (< 5 meters; Dekshenieks et al., 2001), and located below the pycnocline, making it unlikely that it formed through biological settling in the water column. Another option is that biomass accumulates in the WW isopycnal layer as that layer is thinned by increased insolation and capped by warmer water through buoyancy equilibration or preferential photosynthesis in potentially iron-replete WW. An off-shelf surface bloom exists far upstream from our study region in early austral spring; however, this bloom does not persist into late December, when surface warming caps WW. While we do not entirely discount biological production in the DCM, the reasons above support the conclusion that an off-shelf flux of high-chlorophyll surface waters contributes significantly to the presence of the DCM in this area.

An important prediction of our hypothesis is that the ecosystem composition in the off-shelf DCM should resemble that of the on-shelf bloom, although we do not expect chlorophyll to act purely as a passive tracer and some community evolution should be anticipated. Mendes et al. (2012) conducted a chemotaxonomic HPLC (High Performance Liquid Chromatography) analysis on stations within our study area in February/March 2008. They note a sharp gradient in surface ecosystem composition between on-shelf and off-shelf waters. However, the ecosystem composition at depth off-shelf (60-100 m, within our DCM layer) much more closely resembles the surface community on-shelf, especially with regard to its percentage of diatoms. Diatoms tend to dominate other species in high-iron conditions (Boyd et al., 2000). While the high proportion of diatoms in the DCM can be attributed to high-iron concentrations from periodic intrusions of CDW water (Prézelin et al., 2000), advection of either high-iron or high-diatom shelf waters into the area through the mechanism we propose is also consistent with these observations.

The F:b_{bp} ratio is another important biological measurement. As mentioned above, this ratio is dependent on a wide variety of factors, one of which being ecosystem community. In Figure 4.1f we show this ratio for Transects 11 and 12. The daily cycle in the upper ~50 meters is due to NPQ effects. Considering only the off-shelf area, this ratio increases with depth, as expected based on photoacclimation (Cullen, 1982; Neori et al., 1984). However, the similarity in this ratio between on-shelf and

off-shelf blooms is consistent with our advection hypothesis.

Strength of the biological pump

Subduction along isopycnals acts to export material below the mixed layer and out of the euphotic zone. Net subduction therefore contributes to a flux of chlorophyll out of the productive sunlight region and below the depth of surface observations, although storms may deepen the mixed layer sufficiently to partially negate this effect. This sets up a chemostat-like surface environment, where surface on-shelf net primary production is partially balanced by an off-shelf flux. Estimates and models of net primary productivity that do not take into account this subduction mechanism may underestimate the strength of the biological pump in this region.

4.6 Conclusion

We use high resolution Seaglider data over a period of three months to document the seasonal development of a PV gradient along the WW isopycnal layer. We suggest that this gradient will tend to be relaxed through the actions of eddies formed on shelf or advected into the region by the ACC, and will subduct high chlorophyll waters off-shore in the WW layer. We find evidence of chlorophyll subduction along isopycnals, which is not captured in satellite imagery (Figure 4.1a) or in climate simulations due its small scale. This mechanism potentially functions as a highly efficient biological pump in southern Drake Passage, and may be present in topographically similar areas with large surface phytoplankton blooms such as the Kerguelen and Campbell Plateau regions. This study suggests that mesoscale and submesoscale dynamics can make an important contribution to the subduction of high-biomass water masses in the Southern Ocean, emphasizing the need for parameterization in numerical models, especially in strong frontal regions.

Chapter 5

SUBDUCTION FROM SUBMESOSCALE INSTABILITIES IN A SIMPLE ONE-DIMENSIONAL MODEL

5.1 Abstract

Submesoscale instabilities in the water column can induce vertical transport of water masses, leading to the potential for carbon export if carbon-rich water masses are subducted. Baroclinic mixed layer instabilities (BMLI) in particular have been implicated in carbon export below the mixed layer. In this paper we use a simple one-dimensional model of the upper ocean, and parameterize the effects of BMLI, as well as Ekman buoyancy fluxes, on the resulting water column properties. We show that our parameterized fluxes of carbon out of the mixed layer and across depth surfaces is in general larger than those in simpler parameterizations of BMLI. We also use our model to predict export associated with two Bio-Argo floats, and find significant export during the winter-spring transition as a result of the mixed layer pump. This export is, however, greatly increased by submesoscale instabilities, pointing towards the importance of these effects on the marine biological carbon pump.

5.2 Introduction

Biological carbon export from the ocean surface boundary layer is an important pathway in the global carbon cycle. The globally-integrated flux from marine carbon export is estimated at 13 Pg C/yr, or slightly greater than the anthropogenic carbon flux into the atmosphere (Laws et al., 2000). This is accomplished despite the small total mass of phototrophs in the ocean, which is approximately 3 Pg C (IPCC, 2013), implying a turnover rate of weeks to months.

In general, marine carbon is designated as 'exported' if it sinks below the surface mixed layer of the ocean (Passow and Carlson, 2012). Most of the exported carbon is remineralized to inorganic carbon species at greater depths in the water column, with only a small fraction being deposited as sediment (Armstrong et al., 2001). The total export of phototrophic carbon therefore depends on the spatial patterns of production, export, remineralization, and upwelling of this remineralized water back into the surface mixed layer. Once back in the surface mixed layer, the water mass can re-equilibrate with the atmosphere, in the processes releasing much of the

previously sequestered carbon back into the atmosphere (Archer et al., 2000).

The export of carbon is accomplished via three pathways: particulate sinking, vertical migration, and water mass subduction (Ducklow et al., 2001). Most research has focused on the first pathway, wherein negatively buoyant particles (dead phytoplankton or fecal pellets) sink vertically through the water column at a speed determined by their size and composition (Asper, 1987; Burd and Jackson, 2009; Guidi et al., 2009). This sinking material can be captured by conical traps (Buesseler et al., 2007), measured indirectly through isotope disequilibria (Buesseler et al., 1992; Buesseler et al., 1998), or sensed by backscattering of light (Briggs et al., 2011), and is the basis of most estimates of marine carbon export. The second pathway relies on migrators, generally heterotrophic zooplankton, which ascend to the surface at night to feed and descend to depth during the day to hide from predators. If they descend below the surface mixed layer, any carbon they emit, whether by fecal pellets or respiration, may be termed 'export', and in certain regions they can contribute a significant fraction of the total marine carbon export (Longhurst et al., 1990; Steinberg et al., 2000; Takahashi et al., 2009). The third pathway is simply the vertical transport of water masses within the ocean. The ocean is generally in hydrostatic balance, meaning vertical motions are small. This pathway has therefore generally been assumed to be small, with the exception of mode water formation regions in the ocean, where large-scale subduction and subsequent spreading throughout the oceans can lead to carbon export (Stommel, 1979; Sarmiento and Toggweiler, 1984; Broecker et al., 1998; Gebbie and Huybers, 2011).

Research in the past few decades has led to an improved understanding of vertical velocities in the ocean at scales of 0.1–20 km, operationally defined here as 'submesoscales' (Mahadevan and Archer, 2000; Lévy et al., 2001; Lévy et al., 2012; Rosso et al., 2014; Thompson et al., 2016). In particular, a wide array of instabilities that grow at submesoscale wavelengths can lead to significant vertical velocities of $O(100\ \mathrm{m\ day^{-1}})$. Submesoscale dynamics have been implicated in carbon export in observations and models, and have been suggested to contribute up to 25% of global springtime carbon export, and considerably higher fractions in certain regions of the ocean (Omand et al., 2015).

Baroclinic mixed layer instability (BMLI), or the slumping of steep isopycnals within the mixed layer to release potential energy, may be a crucial mechanism leading to submesoscale carbon export. BMLI can be parameterized as an overturning

streamfunction (Fox-Kemper et al., 2008)

$$\psi = C_e \frac{\nabla b H^2}{|f|} \mu, \tag{5.1}$$

where $C_e = 0.06$ is a dimensionless constant, b is the buoyancy, ∇ a horizontal gradient operator defined within the mixed layer, H the mixed layer depth defined by a density difference from the density at 10 m of 0.03 kg m^{-3} (Dong et al., 2008), f the planetary vorticity, and here we use the vertical function (Stone, 1972)

$$\mu(z) = 1 - \left(1 - \frac{2z}{H}\right)^2 \tag{5.2}$$

for $0 \leq z \leq H$, and $\mu(z) = 0$ for $z > H$. The effect of this streamfunction is to re-stratify the mixed layer. If the ocean is primarily temperature-stratified, this restratification can be expressed as a vertically-dependent temperature tendency

$$\frac{\mathrm{d}T}{\mathrm{d}t} = \frac{\rho_0}{\alpha g} \nabla b \psi_z, \tag{5.3}$$

where α is the thermal expansion coefficient (see Equation 5.12 below), ρ_0 is a reference density, g is the gravitational acceleration, and the only depth-varying term in ψ is μ, for which

$$\mu_z = \frac{4}{H}\left(1 - \frac{2z}{H}\right). \tag{5.4}$$

Another mechanism that can generate submesoscale motions is the interaction between the surface wind stress and horizontal buoyancy gradients (Ekman buoyancy flux; EBF) (L. Thomas, 2005). Under the same conditions as for Equation (5.3), the effect of EBF can be expressed as a temperature tendency

$$\frac{\mathrm{d}T}{\mathrm{d}t} = \frac{b_y \tau^x - b_x \tau^y}{f \alpha g z_{Ek}}, \tag{5.5}$$

where x, y subscripts denote horizontal differentiation (note that $\nabla b^2 = b_x^2 + b_y^2$) and $z_{Ek} = \sqrt{A|f|^{-1}} = 32$ m for a typical eddy viscosity $A = 0.1$ m^2 s^{-1}.

5.3 The model

The physical model

We use a model developed by Price et al. (1986) (PWP) to represent 1-D processes in the ocean, and then modify this model to parameterize horizontal submesoscale effects. We also find that it is crucial to parameterize sensible and latent heats (SH and LH) into the model, as described in the equations below.

The basic model (PWP-1D) contains four prognostic variables: temperature (T), salinity (S), and horizontal velocities in x (U) and y (V), and seven forcing variables: incoming shortwave solar irradiation (SW), outgoing long-wave radiation (OLR), precipitation (P), surface wind stress in x and y (τ^x, τ^y), air speed at a reference height of 10 m (U_{10}), and surface air temperature (T_{air}). These evolve according to the set of equations:

$$\frac{\mathrm{d}T}{\mathrm{d}t} = \frac{1}{C_p \rho_0}(I - L) + \kappa T_{zz}, \tag{5.6a}$$

$$\frac{\mathrm{d}S}{\mathrm{d}t} = S(E - P) + \kappa S_{zz}, \tag{5.6b}$$

$$\frac{\mathrm{d}U}{\mathrm{d}t} = -fV + \tau^x + \kappa U_{zz}, \text{ and} \tag{5.6c}$$

$$\frac{\mathrm{d}V}{\mathrm{d}t} = fU + \tau^y + \kappa V_{zz}. \tag{5.6d}$$

Here $C_p = 4218$ J K^{-1} kg^{-1} is the specific heat of water. The absorption of solar irradiation is assumed to follow an exponential

$$I = -\mathrm{SW} e^{-z/\lambda}, \tag{5.7}$$

where $\lambda = 17$ m is the depth scale of solar radiation absorption (note that this is modified slightly from the original formulation of Price et al. (1986) to match the biological model in Mahadevan et al. (2012); see below). Outgoing radiation is non-zero only at the surface:

$$L(z = 0) = \mathrm{OLR} + \mathrm{SH} + \mathrm{LH}, \tag{5.8}$$

where SH and LH are defined as

$$\mathrm{SH} = 0.2 C_p \rho_{\text{air}} C_D U_{10} (T_{\text{air}} - T(z = 0)), \tag{5.9a}$$

$$\mathrm{LH} = -LE, \tag{5.9b}$$

where $L = 2.5 \times 10^6$ J kg^{-1} is the latent heat of vaporization, $\rho_{\text{air}} = 1.293$ kg m^{-3} is a reference density for air, $C_D = 3 \times 10^{-3}$ is the aerodynamic transfer coefficient, and RH $= 0.9$ is the (assumed constant) relative humidity at the air-sea interface. The empirical scaling factor of 0.2 in the equation for SH comes from aligning the SH used in the PWP models with reanalysis results (see below). Evaporation is calculated as

$$E(z = 0) = \rho_{\text{air}} C_D U_{10} q(T(z = 0)) - (\mathrm{RH} q(T_{\text{air}})), \tag{5.10}$$

where the saturation humidity is

$$q(T) = 3.67\exp\left[\frac{L}{R_v}\left(\frac{1}{273.15} - \frac{1}{T + 273.15}\right)\right], \tag{5.11}$$

for T in degrees Celsius, where $R_v = 461$ J kg^{-1} K^{-1} is the water vapor gas constant. Values of $E < 0$ were set to 0; i.e., evaporation could not add freshwater, and latent cooling could not add heat to the ocean. Wind stress was assumed to act on U and V equally within the mixed layer, which was defined within the model as the minimum depth h where either the temperature or one of the horizontal velocities deviated from the surface value by 0.02°C or 0.01 m s^{-1}. Note that this mixed layer depth h is different from the previously defined H; h is here used as the depth of active mixing, whereas H is what would be detectable from *in situ* measurement platforms (which often do not have reliable measurements at the surface or of horizontal velocities). All variables were acted upon by the same diffusivity $\kappa = 2 \times 10^{-5}$ m^2 s^{-1}; i.e., the Prandtl number is unity and there are no double-diffusive effects.

At every time step the model adjusts to achieve static and shear stability. Static stability is reached by requiring $\rho_z > 0$ for all z, where the density is calculated assuming a linear equation of state about reference salinity S_0 and temperature T_0:

$$\rho = \rho_0 + \beta(S - S_0) - \alpha(T - T_0). \tag{5.12}$$

If static stability is not met, the modeled mixed layer is increased until the water column becomes statically stable, where the four prognostic variables are set to the mean value within the mixed layer. For all of the model results we use the same values $S_0 = 35$ ppt, $T_0 = 10$°C, $\rho_0 = 1025$ kg m^{-3}, $\alpha = 0.2$ kg m^{-3} K^{-1}, and $\beta = 0.8$ kg m^{-3} ppt^{-1}.

Requiring shear stability sets minimum thresholds on the the bulk (R_b) and gradient (R_g) Richardson numbers, where

$$R_b = \frac{g\Delta\rho h}{\rho_0(\Delta U^2 + \Delta V^2)} \geq 0.65, \tag{5.13a}$$

$$R_g = \frac{g\partial_z\rho}{\rho_0(U_z^2 + V_z^2)} \geq 0.25, \tag{5.13b}$$

and Δ is a difference across the base of the mixed layer h. If $R_b < 0.65$ the base of the mixed layer is unstable to shear forces, which will mix water masses across $z = h$. This is parameterized by incrementally increasing h, setting the four prognostic variables to the mean value within the mixed layer, and recalculating R_b until the

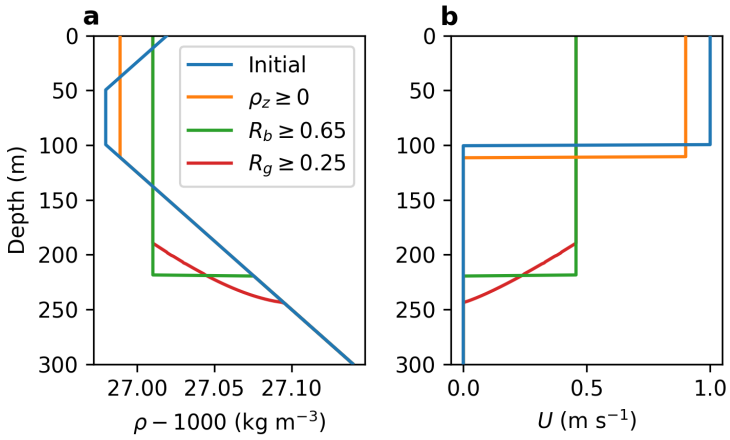

Figure 5.1: Potential density (a) and horizontal velocity (b) profiles illustrating the processes involved in setting water column stability in the PWP model. The blue line gives the initial, unstable profile. The orange line ensures static stability ($b_z > 0$) by homogenizing the water to deeper levels. The green line satisfies mixed layer stability by requiring $R_b \geq 0.65$ (see Equation 5.13a), which it also achieves by homogenizing the water column to successively deeper levels. Finally, the red line ensures shear stability through small-scale mixing between depths where $R_g < 0.25$ (see Equation 5.13b).

stability criterion $R_b \geq 0.65$ is met. Once the bulk criterion is met, R_g is calculated throughout the water column. A well-known Richardson number threshold is 0.25; at lower values small-scale three-dimensional turbulence is activated (Miles, 1961). This process is parameterized by linear vertical mixing of water masses across gradients where $R_g < 0.25$. This mixing extends vertically until the condition $R_g \geq 0.25$ is met throughout the water column.

These processes are illustrated in Figure 5.1, which is initialized with an unstable water column that has dense water at the surface and a sharp change in velocity across the mixed layer base (blue line). Requiring static stability (orange line) erodes the mixed layer slightly. The resulting statically stable mixed layer has large shear across its base, and must be mixed further (green line) to satisfy the bulk Richardson number criterion. However, the mixed layer base is still unstable to small-scale vertical gradients, and the final stable water column (red line) has smoothed out the sharp mixed layer base into a gradient in ρ and U characterized by $R_g = 0.25$.

We extend the PWP-1D model to incorporate BMLI and EBF as described in the Introduction. This modified model, PWP-SM, amounts to incorporating (5.3) and

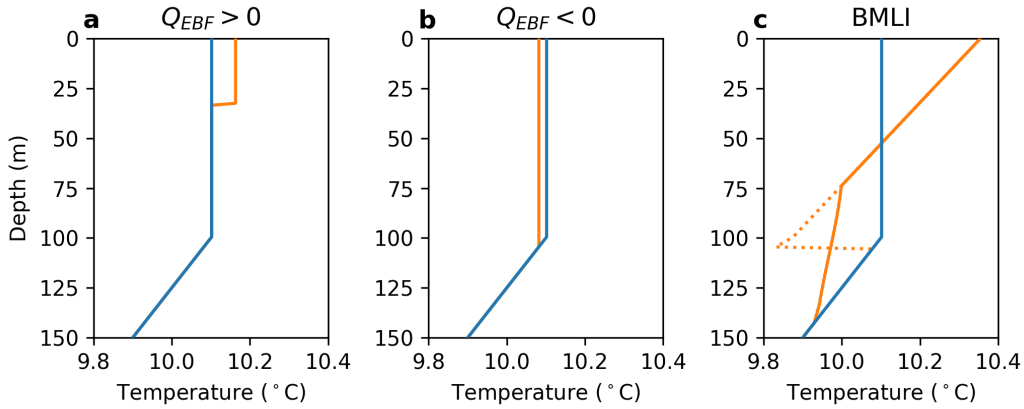

Figure 5.2: Effects of positive (a) and negative (b) Ekman buoyancy flux (EBF) and baroclinic mixed layer stability (BMLI) on a 1-D water column in the PWP-SM model.

(5.5) in (5.6a) as

$$\frac{\mathrm{d}T}{\mathrm{d}t} = \frac{1}{C_p \rho_0}(I - L) + \frac{\rho_0}{\alpha g}\nabla b \psi_z + \frac{(b_y \tau^x - b_x \tau^y)}{f \alpha g z_{Ek}} + \kappa T_{zz}. \tag{5.14}$$

Note that this approach differs from that of du Plessis et al. (2017) and Viglione et al. (2018), which assumed a constant heat input to the mixed layer from BMLI (as in Omand et al. (2015) and Thompson et al. (2016)). Here we do not allow BMLI to act as a heat source. This leads to a warming for $z < H/2$ and a cooling for $H/2 < z < H$, and an associated loss of static stability at the base of the mixed layer. We resolve this by linearly smoothing water masses about this discontinuity, as suggested in Fox-Kemper et al. (2008).

The effects of these submesoscale processes on the PWP model are seen in Figure 5.2. Positive EBF shoals the mixed layer to H_{Ek}, whereas negative EBF leads to a deepening of the mixed layer through static stability (e.g., Figure 5.1). In this formulation, BMLI acting alone shoals the mixed layer to the surface, since the effect is enhanced as $z \rightarrow 0$ m. However, BMLI is always accompanied by other processes, such as SW and OLR. Beneath $z = H/2$ BMLI leads to a layer of homogenized waters which extend deeper than the previous MLD due to the convection mentioned above. Here we also note that BMLI in our model leads to constant restratification in the mixed layer (before the homogenization process at the mixed layer base). This is a simplification to the parameterization developed in Fox-Kemper et al. (2008) that is caused by our choice of a simple, quadratic expression for μ (Equation 5.2) (Stone, 1972). Using a quartic expression, as recommended by Fox-Kemper et al.

(2008), leads to an increase in warming at the very surface, and a decrease in the discontinuity at the base of the mixed layer. However, a quartic expression for μ adds extra complexity to the problem, and we do not expect this change to qualitatively affect any of the results.

The biological model

We incorporate a simple biological model into the PWP framework, involving three prognostic variables: carbon biomass (C_{bio}), dissolved organic carbon (DOC), and dissolved inorganic carbon (DIC). These variables are understood to be deviations away from mean values in the ocean, and are evolved according to

$$\frac{\mathrm{d}C_{bio}}{\mathrm{d}t} = (\gamma - m)C_{bio} \qquad -wC_{bio,z} \qquad +\kappa C_{bio,zz} \tag{5.15a}$$

$$\frac{\mathrm{dDOC}}{\mathrm{d}t} = amC_{bio} \qquad -k\mathrm{DOC} \qquad +\kappa \mathrm{DOC}_{zz} \tag{5.15b}$$

$$\frac{\mathrm{dDIC}}{\mathrm{d}t} = ((1-a)m - \gamma)\, C_{bio} \qquad +k\mathrm{DOC} \qquad +\kappa \mathrm{DIC}zz, \tag{5.15c}$$

where $w = 1$ m day^{-1} is the assumed sinking speed, $m = 0.1$ day^{-1} is the mortality rate, $a = 0.1$ is the fraction of mortality that enters the DOC pool via "sloppy eating", $k = 1$ yr^{-1} is the decay timescale of DOC to DIC back to mean values, and growth (γ) is assumed to be of a hyperbolic form

$$\gamma = \alpha I \gamma_{max} \left(\gamma_{max}^2 + \alpha^2 I^2\right)^{-1/2}, \tag{5.16}$$

where $\alpha = 10^{-6}$ m^2 J^{-1} is a growth rate parameter, $\gamma_{max} = 0.5$ day^{-1} is the maximum allowed growth rate, and the depth-dependent solar irradiance is approximated by

$$I(z) = \mathrm{SW} e^{-z/\lambda - k_c \int_0^z C \mathrm{d}z}, \tag{5.17}$$

where $k_c = 0.05$ m^2 (mg Chl)$^{-1}$ is the attenuation coefficient for chlorophyll. We also assume a weight ratio for chlorophyll:carbon of 15:1. The model for carbon is nearly identical to that used in Mahadevan et al. (2012). The sinking speed is set to a relatively low number to simulate the effects of small, nearly neutrally buoyant particles that are typically assumed to not contribute significantly to the carbon export flux. Heat uptake via absorption of radiative energy by biomass is assumed to be negligible; i.e., biology does not feed back on the dynamical heat balance in (5.6a) or (5.14). We also assume that DIC is immediately equilibrated to the atmospheric value when in the mixed layer; that is, DIC within the mixed layer is always set to 0.

These three biological variables are treated as dynamically passive tracers. They are mixed uniformly throughout $z < h$ while satisfying static and bulk Richardson shear stability, and diffused via the κ term, through satisfying gradient Richardson shear stability, and through resolving the temperature discontinuity resulting from BMLI.

Export of carbon is defined in two ways: either as export out of the mixed layer or as export beneath the 250 m depth horizon. The latter is approximately equal to the wintertime MLD. In both cases, cumulative carbon export is calculated as the sum of the three biological variables beneath the given depth horizon.

We compare these export estimates to the parameterization of Omand et al. (2015), where during periods of BMLI the flux across the base of the mixed layer is calculated as

$$E_{O15} = \frac{C_e \nabla b^2 H}{|f| b_z} C_{ML}, \tag{5.18}$$

where the effects of a vertically-varying μ term have been neglected and C_{ML} is the mixed layer sum of C_{bio} and DOC.

5.4 Idealized model runs

We first run the PWP-1D model for an idealized seasonal cycle. Solar insolation is sinusoidal with period 365 days, mean value 342 W m^{-2}, and amplitude 100 W m^{-2}. Days 90 and 270 are the equinoxes, and day 0 (180) is the summer (winter) solstice. Outgoing longwave radiation is constant at 342 W m^{-2}, $T_{air} \equiv T(z = 0)$, and there is no wind stress or precipitation. Initial values are $S = S_0$, $U = V = 0$, and T is uniform at T_0 throughout the upper 30 m and decreases with depth at a constant rate equivalent to $b_z = 10^{-5}$ s^{-2} below.

The mixed layer undergoes a steady autumn and winter deepening, and a shoaling in the spring due to restratification caused by increased SW. Our simple model captures the observed asymmetry in mixed layer depth between the autumn and the spring (Figure 5.3); during autumn the existing pycnocline is steadily eroded; during the summer the deep wintertime mixed layers are capped by warmer water generated by solar heating, with a constant depth scale (set by λ) (Erickson and Thompson, 2018). In the real ocean, stratification develops beneath the strong summer pycnocline by a combination of vertical diffusion and horizontal advection of water masses into the area; our model does not have horizontal advection, so the increase in summertime temperature stratification below the mixed layer is simply due to the diffusion term.

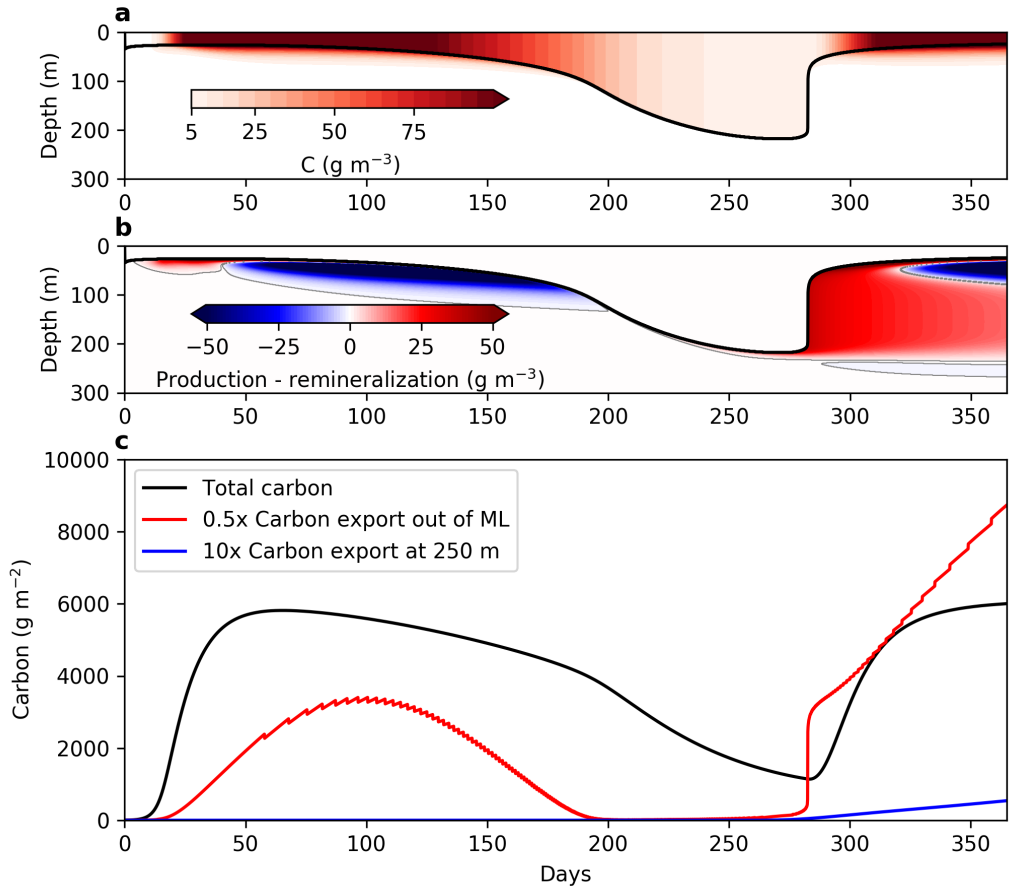

Figure 5.3: PWP-1D model run as for a simple seasonal cycle (365 days) as described in the text. The summer solstice is at day 0. Carbon concentrations are given in (a), and the difference between C_{bio} + DOC and DIC is in (b), where negative values indicate net remineralization and positive values net production. Values within the mixed layer are set to zero because DIC is assumed to be instantaneously eequilibrated across the air-sea interface. Thin grey lines give the 0 contour. Black lines in panels (a,b) show the mixed layer depth h. (c) Total carbon (black), carbon export across the mixed layer depth h (red) and across the 250 m depth surface (blue).

During the summer carbon stocks increase within the mixed layer, and sink out of the mixed layer at a rate prescribed by w (Figure 5.3a,c). This leads to a disequilibrium between production (growth of C_{bio} and DOC) and respiration (growth of DIC beneath the mixed layer) (Figure 5.3b). Cumulative carbon export is calculated as both across the mixed layer depth interface (red line; divided by 2) or across the 250 m depth surface (blue line, multiplied by 10), where the latter definition is approximately the depth of the wintertime mixed layer. The export across h is positive in the summer due to sinking of particulates that are remineralized below

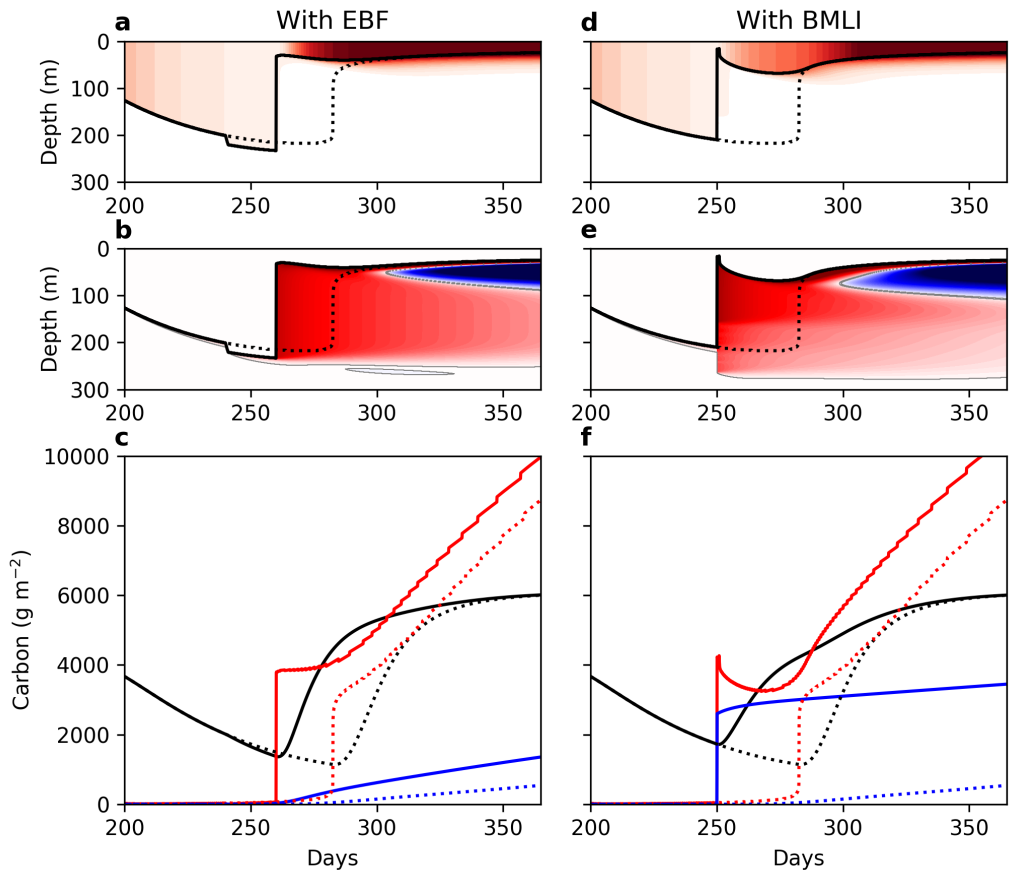

Figure 5.4: As in Figure 5.3, except with the addition of EBF and BMLI as described in the text. For each panel, dotted values give the results of the simple PWP-1D model (Figure 5.3. Note that before day 200 the results are identical to those in Figure 5.3.

$z = h$. A sinking speed of 1 m day^{-1} combined with a loss term of 0.1 day^{-1} implies that carbon sinks on average 10 m before being remineralized. As the mixed layer deepens in autumn it entrains this "exported" material, and the cumulative carbon export returns to zero. At the spring restratification event starting on day 270 (the spring equinox), the mixed layer abruptly shoals, leaving behind carbon which gradually is remineralized, contributing to export. The carbon export below the 250 m depth horizon is zero until the mixed layer depth increases to near 250 m, after which it rises slowly primarily due to the vertical diffusion in the model.

We now add EBF to the model by imposing a destratifying EBF of -1000 W m^{-2} during day 240 and a restratifying EBF of +1000 W m^{-2} during day 260 (Figure 5.4a–c). This leads to a deepening of the ML by about 10 m at day 240, and a

shoaling to Z_{Ek} at day 260. The net radiative forcing is unable to re-mix the waters, and this imposed EBF leads to an earlier spring restratification, as is often seen in observations (e.g., Mahadevan et al. (2012)). The total carbon present at the end of the year is identical to the model run without EBF; however, the carbon export (for both metrics) are higher due to both the deeper mixed layer depths, which increases the export across $z = 250$ m, and the early restratification, which increases the export across the base of the mixed layer.

We isolate the effects of BMLI by adding BMLI associated with $\nabla b = 5 \times 10^{-7}$ s^{-2} during day 250 (Figure 5.4d–f). This causes a dramatic shoaling of the mixed layer, which does not recover its wintertime depth even though the region experiences net negative surface buoyancy forcing until day 270. This forcing leads to similar increases of carbon export as in the case with EBF.

We compare the increase in export across the mixed layer base in the case with BMLI to the prediction from Equation 5.18 (Omand et al., 2015). During day 250, $b_z = 9.6 \times 10^{-6}$ at the base of the mixed layer, $H = 235$ m, and $C_{ML} = 8$ g m^{-3}. If we account for drawdown of $C_{bio,ML}$ due to the export from BMLI, the export becomes

$$E_{O15} = wc = wC_{bio,ML} - \frac{w^2 t}{H} C_{bio,ML}, \tag{5.19}$$

where $w = \frac{C_e \nabla b^2 H}{|f| b_z}$ (see Equation 5.18). Integrated over a day gives an estimated flux of 825 g C m^{-2}. This is much less than the value we calculate across the mixed layer base — however, this discrepancy is due to the fact that our model resolves the sharp decrease in mixed layer depth after BMLI. A more appropriate comparison might instead be the carbon export at 250 m. This is also significantly larger, by a factor of about 3. Our method, which more appropriately mixes surface properties deeper below the mixed layer depth, therefore gives much larger expected subduction values than those from Omand et al. (2015).

5.5 Realistic forcings from a Bio-Argo float

Our model can be used as a test bed for Lagrangian analyses from a variety of sources. Here we choose two Bio-Argo floats to use with our model. These were active in the north Atlantic Ocean between the periods of 2014–2015 (ID 6901516) and 2017–2018 (ID 6901180) (Figure 5.5). Argo floats drift with ocean currents at 1 km depth, and ascend to the surface every 5 days while taking measurements at intervals ranging from under 1 to about 10 m. It is therefore unclear the extent to which PWP-type models will accurately represent Argo data, as PWP assumes a

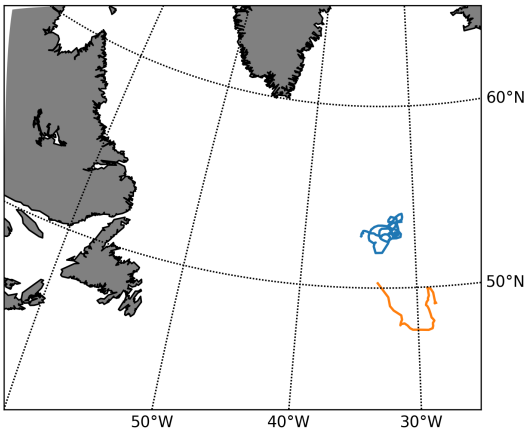

Figure 5.5: Locations of float 6901516 (blue) and 6901180 (orange).

1-D ocean (i.e., that the float is perfectly Lagrangian), whereas Argo floats are only approximately Lagrangian, and only at 1 km depth. We have specifically picked these floats because their properties, primarily their calculated mixed layer depths (H), are similar to those calculated using PWP.

We interpolate surface forcings from NCEP reanalysis data to the interpolated Argo float position at 6 hour intervals. The forcing variables used by the PWP models for each of the Argo floats are found in Figure 5.6 (first four rows).

To add the submesoscale forcings from EBF and BMLI requires knowledge of the horizontal buoyancy gradients in the ocean mixed layer. We estimate these by calculating average horizontal and meridional SST gradients from MODIS Aqua data within about 10 km about the interpolated float position. These SST gradients are interpolated in time using a Gaussian window to account for times with cloud cover, and converted to buoyancy gradients using our constant α value and assuming no compensation in salinity. We use this method to estimate mixed layer buoyancy gradients in the OSMOSIS region (see Chapters 2 and 3 of this thesis), and compare our satellite-based method to *in situ* glider observations in that location. The results indicate a mean discrepancy of about a factor of four, which we suggest is due to the spatial and temporal averaging applied to the satellite gradient calculations (Figure 5.7). Accordingly, we multiply our satellite results by this empirical scaling factor. The final ∇b values range from near-0 to almost 10^{-6} s^{-2}, which is very large. We set 5×10^{-7} s^{-2} as a maximum-allowed ∇b value in the analyses below. Our calculated EBF ranges from about -800 to 800 W m^{-2}. An EBF of 800 W m^{-2} corresponds to a temperature change of 0.2°C day^{-1} over the upper 100 m of the water column.

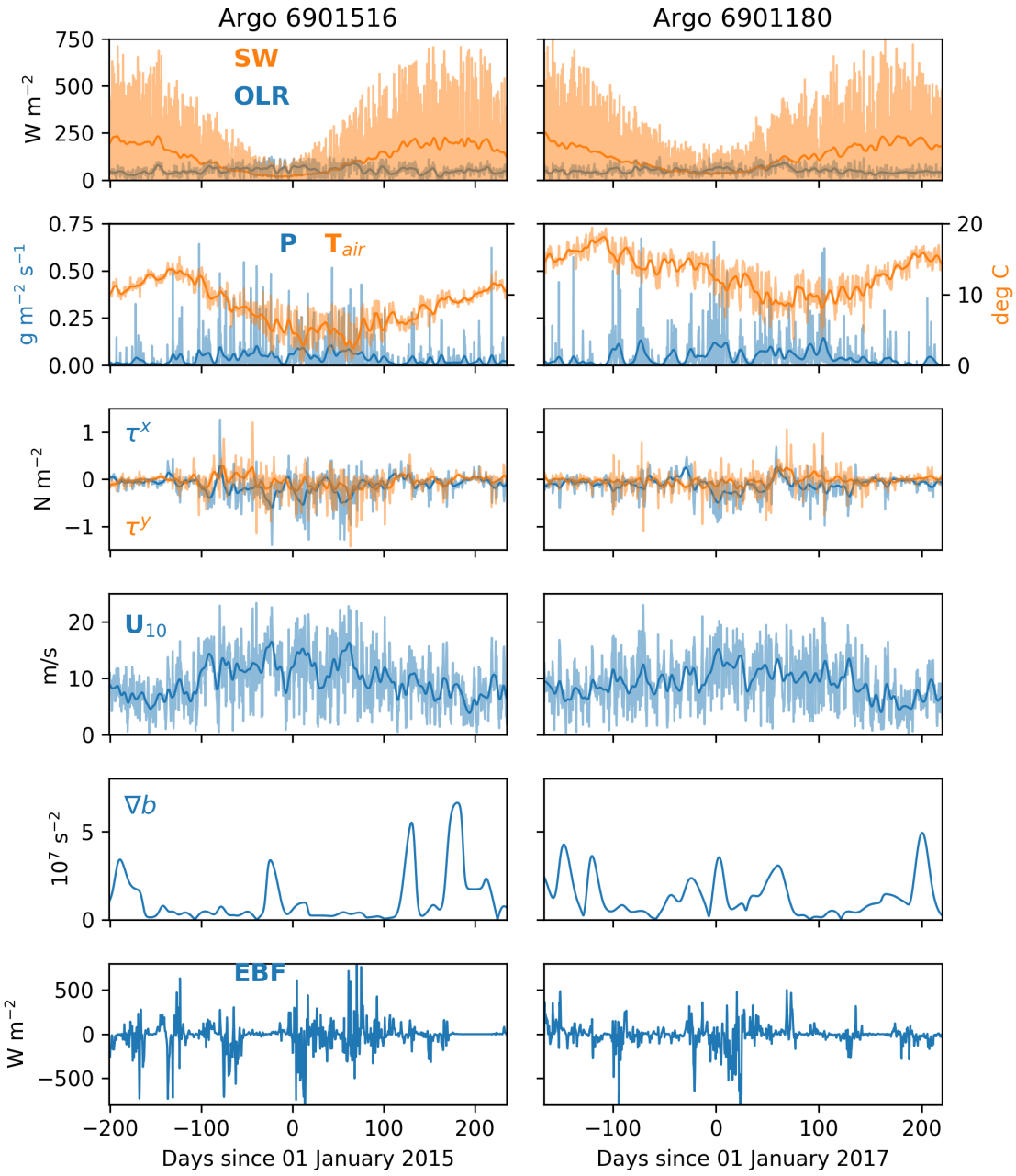

Figure 5.6: Surface forcings used for float 6901516 (left) and 6901180 (right). The first four rows are derived from NCEP reanalysis data. The bottom two are from SST gradients from MODIS Aqua, as described in the text. The light lines give the data used in the model; the dark lines give a smoothed result for ease of comparison.

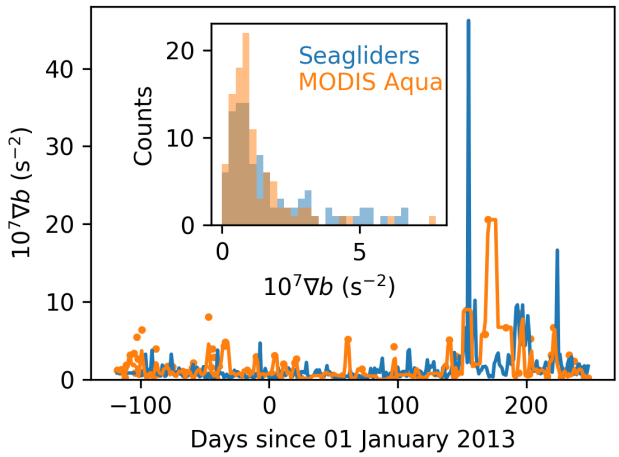

Figure 5.7: Buoyancy gradient observations from OSMOSIS Seagliders (blue) and derived from MODIS Aqua SST data (orange), using a constant α term. Scattered orange dots give the data, and the orange line interpolates the data using a Gaussian windowing function. The MODIS-based data are multiplied by 4 to compare best with the observed data. Note that only the full horizontal gradient is shown here (∇b); to calculate EBF this was broken up into zonal (b_x) and meridional ($b_x y$) components.

We take this value (±800 W m^{-2}) as the limit of our EBF forcing.

We apply the PWP-1D and PWP-SM models as described in the previous section to the initial data from the two Argo floats using the interpolated surface forcings. Initial data were taken as an average from the first fives Argo profiles, and smoothed vertically with a Gaussian filter with a standard deviation of 50 m. The mixed layer depths (H) calculated from each model run, as well as from the Argo floats, are shown in Figure 5.8). For float 6901516, both models capture the summer and autumn mixed layer depths and the timing of the spring restratification well, although the PWP-SM model has deeper wintertime H that better match the observations. For float 6901180, both PWP models are too shallow during winter but otherwise match the observed H values and the timing of the spring restratification well; the submesoscale fluxes in PWP-SM give significantly more variability in H than in the PWP-1D model, especially in autumn.

The temperature time series for each model, as well as the Argo floats, are shown in Figure 5.9. For both floats, the temporal change in temperature profiles matches well for both PWP-1D (center) and PWP-SM (bottom) during the autumn cooling period; however, the temperature decreases more rapidly than observed in the Argo

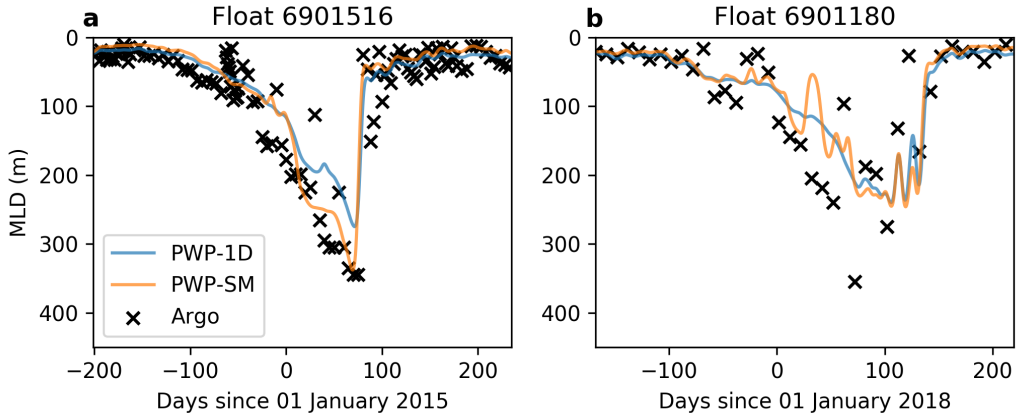

Figure 5.8: Mixed layer depths (H) for Argo float 6901516 (left) and 6901180 (right) using the PWP-1D model (blue lines), PWP-SM model (orange lines), and Argo float data (black x's).

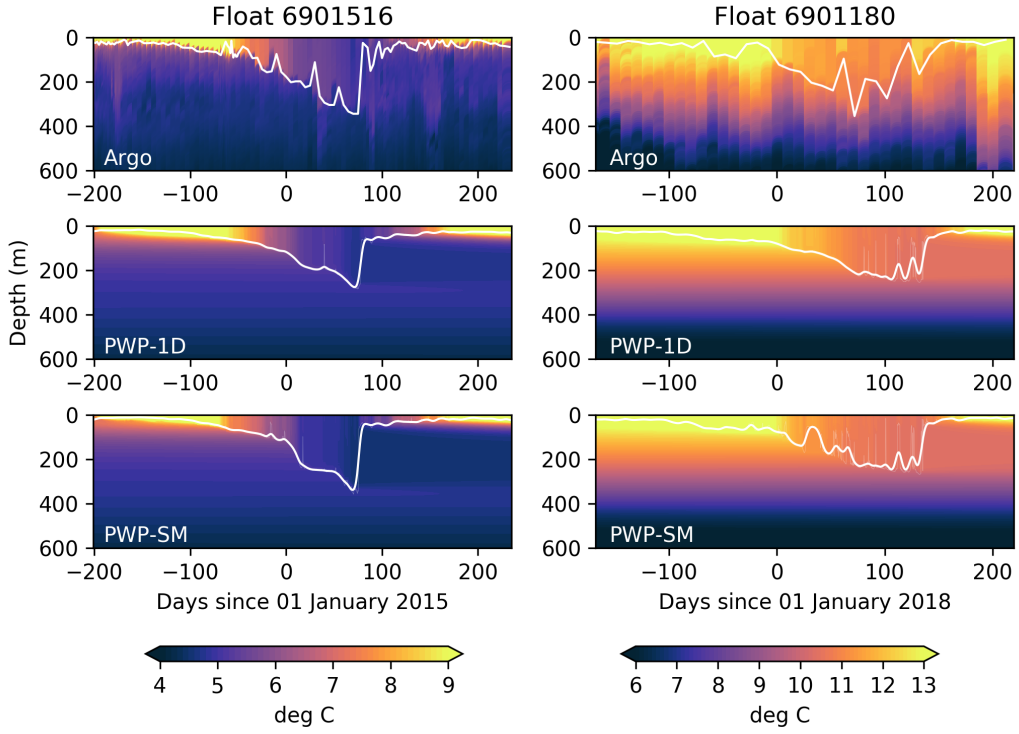

Figure 5.9: Comparison of the results for Argo float 6901516 (left) and 6901180 (right). Argo temperature data are in the top panels, PWP-1D model results are in the center, and PWP-3D results in the bottom. White lines give the mixed layer depths H. For the PWP results these are lightly filtered with a Gaussian convolution; the non-filtered results are given by the thin grey lines.

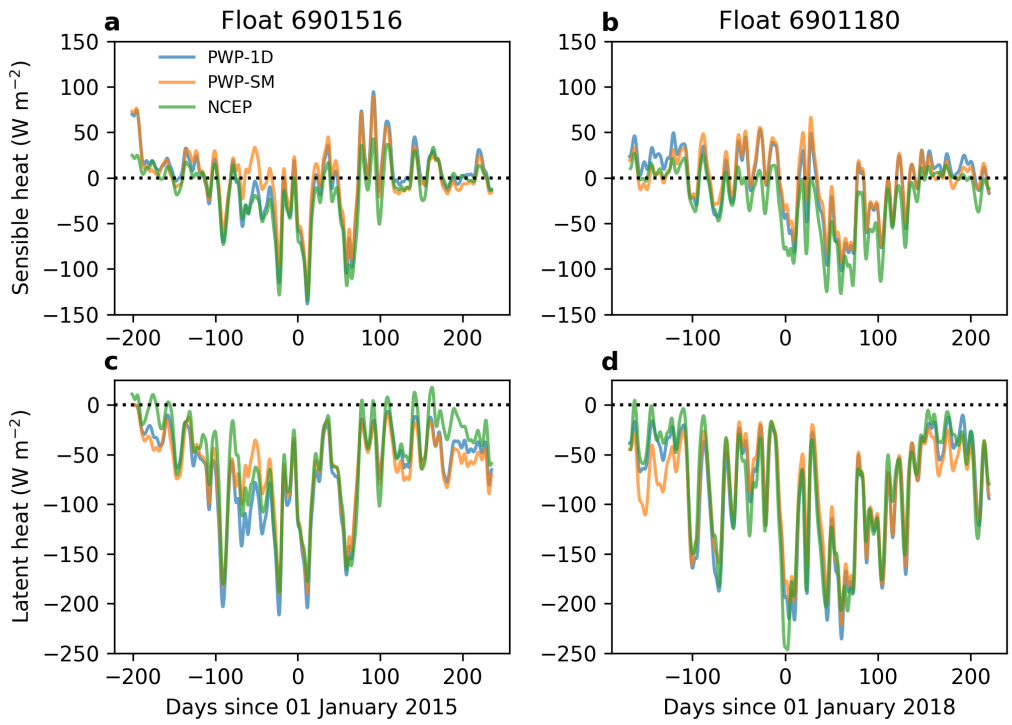

Figure 5.10: Sensible heat (a,b) and latent heat (c,d) for Argo float 6901516 (a,c) and 6901180 (b,d) for the PWP-1D model (blue), PWP-SM model (orange), and NCEP reanalysis (green). Note that the NCEP reanalysis also includes the latent heat gained by precipitation, and therefore sometimes becomes positive.

data during winter (top). After the spring restratification the temperature beneath the new mixed layer is only modified by vertical diffusivity, which is kept small in the model, accounting for the large discrepancy in interior temperatures after about day 80. A major forcing on the model is the estimated SH and LH. These compare very well (after reducing the SH by a factor of 5 as noted in Equation 5.9a) with NCEP reanalysis results (Figure 5.10).

Carbon (C_{bio}) was initialized in each model as a small amount within the mixed layer, and DOC and DIC were initialized at zero. All three were allowed to develop as per Equation 5.15. We also include a model run similar to PWP-1D, but at each time step the export out of the mixed layer from BMLI was calculated as per Equation (5.18); C_{bio}, DOC, and DIC were uniformly drawn down from the mixed layer as a result of this flux and deposited in a layer 10 m thick beneath $z = H$ (PWP-O15).

Surface values are compared with data from near-surface Argo backscatter data in

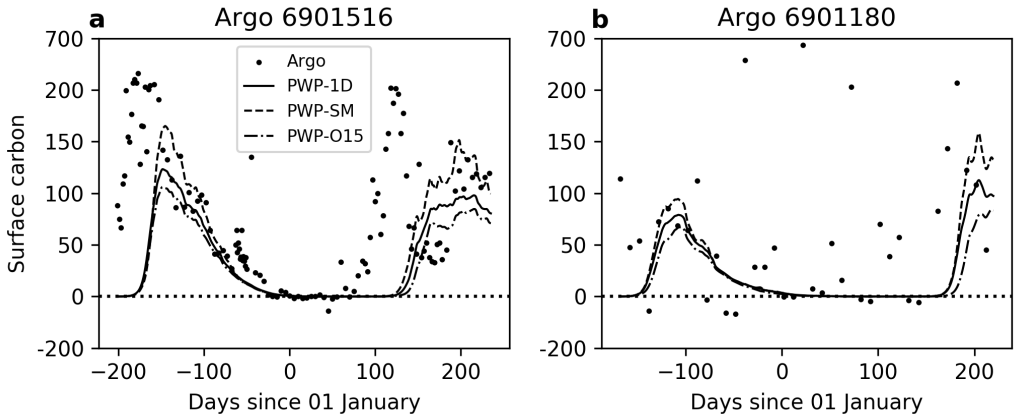

Figure 5.11: Comparison between surface carbon concentrations in the different PWP models (lines) and the Argo float at the uppermost measurement (typically at 2–4 m). The Argo float measurements are expressed after having been scaled and offset to best match the measurements.

Figure 5.11. Here backscatter values are adjusted linearly to best align with the modeled results (i.e., units are arbitrary). For float 6901516, the model represents the drawdown of surface carbon during the autumn well, but the spring increase lags the observations, which reach their maximum at about day 110 and decline from there. This observed springtime bloom is probably caused by larger, faster-growing organisms that also sink very quickly, and are not well captured by our model, which is tuned to more closely match smaller phytoplankton with slower sinking rates. For float 6901180, there are many high carbon values during the winter that appear incongruous, and it is difficult to tell how well our model does at capturing the biological cycle.

In general, the PWP-SM model shows slightly higher carbon export across $z = H$ than the PWP-1D model, and significantly higher carbon export at 250 m (Figure 5.12). For float 6901516 this is primarily due to the increase in H in PWP-SM (Figure 5.8a), but this increase is also present for float 6901516, which did not have a corresponding increase in H during winter between PWP-SM and PWP-1D. Somewhat non-intuitively, when the parameterized export (PWP-O15) is added to the model, the total carbon export at H decreases from the simple PWP-1D model. This is due to the drawdown of carbon in the mixed layer due to the parameterized fluxes; in PWP-SM this drawdown is accompanied by a restratification and therefore consolidation of phytoplankton in the euphotic zone and increased growth, but this effect is not present in the parameterized export. However, the export at 250 m

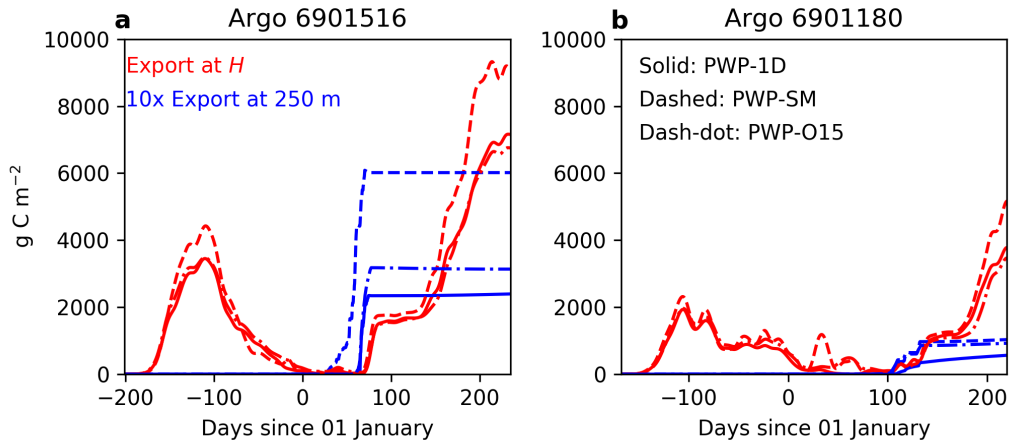

Figure 5.12: Carbon export calculated at two depth horizons, calculated as in Figure 5.3c and 5.4c,f, for Argo float 6901516 (a) and 6901180 (b).

depth is increased in the PWP-O15 model above that in PWP-1D, although not to the extent of PWP-SM.

5.6 Discussion

Effect of BMLI

BMLI emerges as a major candidate for export of carbon in our model. This is due to the the temperature discontinuity at the base of the mixed layer following an episode of BMLI, which is typically relaxed by a vertical diffusion term (Fox-Kemper et al., 2008). The effect of this enhanced vertical diffusion is to subduct other tracers such as carbon out of the mixed layer and deeper into the interior, where they can be considered exported.

Our formulation differs from that of Omand et al. (2015) in that we explicitly parameterize the vertical extent of this flux. We do so by including the vertical profile of the BMLI buoyancy tendency term, μ, back into the Fox-Kemper et al. (2008) parameterization. However, a fair comparison with the Omand et al. (2015) parameterization is complicated because the process defined above does not simply relate to a flux across the mixed layer base as in Equation 5.18. We can move towards this sort of parameterization by analytically calculating the effect of BMLI on the mixed layer (Figure 5.2c). We assume the end effect of BMLI is to create a thermostad at $T_0 - \delta T$ for z between z_1 and z_2, where $z_1 < H < z_2$, the temperature profile remains continuous throughout the water column, and we assume the previous mixed layer temperature was T_0. Further assuming no heat is gained or lost as a

result of BMLI,

$$\int_{z_1}^{H} T_{z,BMLI}\left(z - \frac{H}{2}\right) \mathrm{d}z = \int_{H}^{z_2} T_{z,pyc.}(z - H)\mathrm{d}z, \tag{5.20}$$

where $T_{z,BMLI}$ is the vertical derivative of temperature in the mixed layer following BMLI, and $T_{z,pyc.}$ is the vertical derivative of temperature within the pycnocline (assumed constant with depth). Here the left hand side is the heat gained by the lower part of the mixed layer following the strong diffusive flux that erodes the unstable temperature gradient (or more generally, buoyancy gradient) at the base of the mixed layer following BMLI, and the right hand side is the heat lost by the upper part of the pycnocline. Since the temperature profile remains continuous,

$$T_{z,BMLI}\left(z_1 - \frac{H}{2}\right) = T_{z,pyc.}(z_2 - H). \tag{5.21}$$

Then we can solve for $\delta z = z_2 - H$, the depth to which surface properties are subducted into the pycnocline within the newly-formed thermostad at the base of the previous mixed layer depth, as

$$\delta z = \frac{H}{2}\frac{R(1 - R^{1/2})}{1 - R}, \tag{5.22}$$

where R is the ratio between the vertical temperature derivative in the mixed layer, $T_{z,BMLI}$, and the derivative within the pycnocline, $T_{z,pyc.}$. But this is nothing but

$$R = \frac{8C_e \nabla b^2 \delta t}{|f| b_z}, \tag{5.23}$$

where δt is the time step, b_z is the pycnocline stratification, and we have used (5.3) and the knowledge that $\mu_{zz} = 8H^{-2}$. This ratio R is shown for varying b_z and ∇b in Figure 5.13a. Export from BMLI in our model can be thought of as the amount of carbon fluxed below the previous mixed layer depth through this mechanism, or

$$E_{BMLI} = \frac{H}{H + \delta z}\frac{C_{ML}\delta z}{\delta t} \approx \frac{C_{ML}\delta z}{\delta t}, \tag{5.24}$$

where the first fraction is the dilution factor and the approximation assumes $H \gg \delta z$. Using (5.23) to re-write (5.18) and incorporating (5.22) into 5.24), we find the ratio between these estimates to be (Figure 5.13b)

$$\frac{E_{BMLI}}{E_{O15}} = 4\frac{1 - R^{1/2}}{1 - R}. \tag{5.25}$$

This ratio, shown in Figure 5.13b, is unity at $R = 9$, and goes to 4 as R decreases.

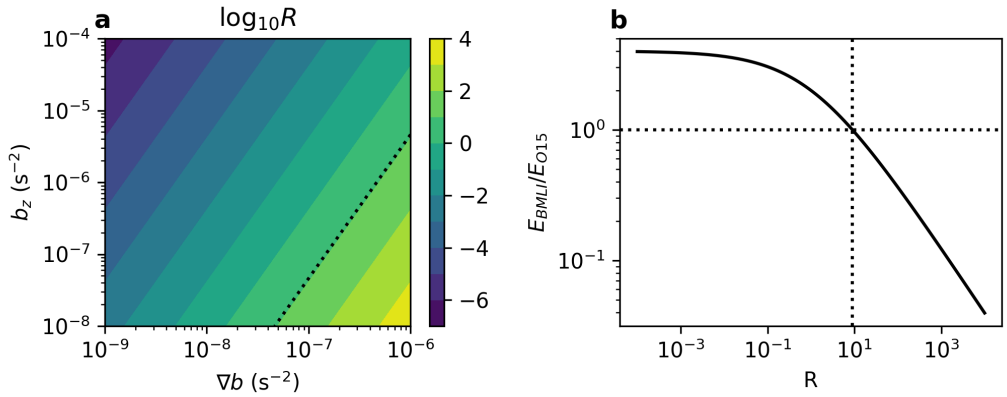

Figure 5.13: (a) Ratio R between vertical derivatives of temperature in the mixed layer following BMLI and in the pycnocline (see Equation 5.23), for $\delta t = 0.1$ day. (b) Ratio of export estimates (see Equation 5.25) with respect to R. Dotted black lines in each panel show where this ratio is unity, which occurs at $R = 9$.

We can use this result to explain the factor of 2.5 difference between the export calculated using the PWP-SM model and using the Omand et al. (2015) parameterization in Equation (5.18) in Figure 5.2c. For that system, $R \approx 1.1$, giving an expected ratio of about 2 for $\delta t = 0.1$ day. For our Argo-based results, in general $\nabla b < 10^{-7}$ s^{-2} (Figure 5.6) and $b_z > 10^{-6}$ s^{-2} (not shown), meaning $R < 9$ and $E_{BMLI} > E_{O15}$, as seen in Figure 5.12.

This result also shows that as b_z at the base of the mixed layer decreases, and the horizontal buoyancy gradients increase, the results of Omand et al. (2015) (E_{O15}) become closer to what we calculate here as E_{BMLI}. In other words, when export potential through BMLI is weak (high b_z and low ∇b), our results indicate proportionally higher export via BMLI (but still likely small). However, when export potential is strong, which is especially likely during the winter to spring transition (Erickson and Thompson, 2018), the parameterization developed here agrees much better with that used in Omand et al. (2015).

Effect of EBF

This study also highlights EBF as providing a mechanism for exporting carbon, either by periodically advecting heavier water over light and thereby increasing the mixed layer depth, allowing surface properties to mix to deeper depths (as in Figure 5.4a), or by advecting lighter water over dense and abruptly shoaling the mixed layer (as in Figure 5.4b). This latter effect only contributes to export if the mixed layer

does not subsequently return to its previous state, re-entraining the "exported" water masses. However, this periodic restratification can also spur increased biological production by concentrating phytoplankton within the euphotic zone, where they can grow more rapidly (Lacour et al., 2017). This effect was also captured in this model (e.g., Figure 5.1c).

Effect of constant sinking speed

The imposed, assumed constant sinking speed of 1 m day^{-1}, combined with a constant death rate of 0.1 day^{-1} leads to a mean sinking of 10 m before remineralization of C_{bio}. The sinking speed is in reality highly variable, and increases with particle size (Alldredge and Gotschalk, 1988; Richardson and Jackson, 2007). Larger particles therefore sink more rapidly, and lead to greater carbon export can become decoupled from submesoscale vertical velocities. However, smaller particles that sink slowly, such as are represented in the model developed here, will be impacted by these submesoscale velocities. Indeed, modeling work by Taylor (2018) shows that submesoscale vertical velocities can effectively subduct even positively buoyant phytoplankton, with upwards vertical velocities of up to 5 m day. Thus a full accounting for the importance of carbon export via submesoscale subduction should include some representation of the observed size distribution of particulates in the ocean (Briggs et al., 2013; Boss et al., 2018)

Limitations of a 1-D model

The PWP-SM is an attempt to reconcile 3-D submesoscale dynamics, which involve horizontal buoyancy gradients, with a 1-D model that is able to track a Lagrangian reference frame. One issue with this model is the limited ability to re-stratify the interior ocean during the summer, as already discussed above. Another issue is the inability to accurately portray horizontal gradients in biological properties. Biology in the ocean is patchy (Estapa et al., 2015; Stukel et al., 2015), and this cannot be captured here. For example, carbon advected along sloping isopycnals (e.g., (Erickson et al., 2016)) will not be captured in this model. This patchiness also turns up in vertical profiles because of vertical shear in horizontal flows in the ocean; this vertical shear prohibits water columns from being truly Lagrangian.

One instance where vertical shear becomes important is in symmetric instabilities (L. Thomas et al., 2013), which have recently been implicated in carbon export in the open ocean due to their ability to rapidly subduct surface properties below the mixed layer (Erickson and Thompson, 2018). Methods for parameterizing

symmetric instabilities in simple 3-D models are still in their infancy (Bachman et al., 2017), and a realistic 1-D representation is not yet available to be used in this model.

5.7 Conclusions

This chapter provides an explicit representation of the vertical structure of submesoscale fluxes and their impact on carbon export. This approach differs from previous studies, e.g. Omand et al. (2015), which have used the maximum vertical velocity within the mixed layer due to submesoscale instabilities in their flux calculations of carbon biomass out of the mixed layer. We feel like this may be an inadequate representation of the submesoscale fluxes because BMLI does not lead to subduction below the mixed layer; rather, export arises as a secondary result of mixed layer restratification. An initially surprising result of our analysis, therefore, is that under horizontal and vertical buoyancy gradients typical of most ocean conditions, our explicit parameterization of the vertical transport across the mixed layer base is larger than that of Omand et al. (2015). The increased export is due to the buoyancy discontinuity at the base of the mixed layer set up by the Fox-Kemper et al. (2008) parameterization of BMLI, which leads to enhanced diffusion and therefore increased subduction of water masses across the base of the mixed layer.

We also include the effect of Ekman buoyancy forcing (EBF) in our model, which can also lead to export through periodically deepening the mixed layer, mixing high-carbon waters from the surface to greater depth. In idealized simulations, the effects of EBF on export are comparable to those of BMLI, pointing to the need to consider this effect in realistic conditions.

Finally, this chapter provides a framework for applying this model to water masses in the ocean via Lagrangian platforms such as Argo floats. The holy grail of marine carbon export research is to predict export from surface properties. Our addition of submesoscale forcings and parameterization of carbon fluxes in a one-dimensional PWP model forced only through surface fluxes provides a step towards this goal, which can be improved through implementation of this model in more measurement-rich Lagrangian studies such as the NAB (North Atlantic Bloom) study (Alkire et al., 2012; Mahadevan et al., 2012; Omand et al., 2015) or EXPORTS (EXport Processes in the Ocean from RemoTe Sensing) (Siegel et al., 2016).

APPENDIX: GLIDER RECOVERY — THE MUSICAL

This skit was co-written with Giuliana Viglione, Janet Sprintall, Adele Morrison, and Jamie Yin. It was first performed at Palmer Station on 06 May, 2015, during an open mic night, with Adele Morrison as the Narrator, Jamie Yin as the glider, Zach Erickson as Robert (third mate), and Matt Louis (marine technician) and Giuliana Viglione as themselves. Janet Sprintall added to the kick line.

Narrator: This is the story of a group of scientists studying Changes in Stratification at the Antarctic Peninsula – a group known as ChinStrAP [all else turn around, point to t-shirt]. One of their Seagliders has run out of battery power and is slowly drifting northwards into the middle of Drake Passage. We join our intrepid team of young scientists on the good ship Laurence M. Gould as they pursue the glider.
All: Hi ho, hi ho, it's across the Drake we go / We're looking for our Seaglider, hi ho, hi ho / Hi ho, hi ho, halfway to Punta we will go / For science, we will go all night, hi ho, hi ho, hi ho, hi ho. (to the tune of "Heigh Ho")
Narrator: The sun rises on the morning of recovery.
Matt: [Goofy voice] Its a beautiful day in Antarctica! (from Mr. Rogers)
Narrator: There is no wind and conditions are ideal. The science team is up on the bridge and all are feeling confident about recovering the glider.
Narrator: Young Master Robert, the third mate, spots the glider bobbing up and down in the water [glider bobs up and down]. The glider recovery team mobilizes the zodiac. They are three: Matt, the MT with the Mostest, Giuliana, the Caltech science girl, and ...
All: I met him at the Palmer Store / He turned around and smiled at me / You get the picture?
Audience: Yes, we see!
All: That's when I fell for, Zodiac Jack, vroom, vroom! ("Leader of the Pack")
Narrator: Young Master Robert goes down to breakfast, and as he leaves, he implores:
Robert: The Antenna!
All: Do not let it go!
Glider: Let me go!
Robert: The Antenna!

All: Do not let it go!

Glider: Let me go!

All: Do not let it go!

Glider: Let me go!

All: Do not let it go! There it goes, goes, goes, goes, goes, goes, goes, goes, goes! ("Bohemian Rhapsody")

Narrator: The bridge radios down to the zodiac team. The glider is lost! The bridge crew resumes their search as the skies begin to darken. A storm is brewing!

All: The weather started getting rough, the LM Gould was tossed, if not for the effort of the fearless crew, the glider would be lost, the glider would be lost ("Gilligan's Island")

Narrator: All hands join the search, but in vain. Without other options, we must call upon Young Master Robert once more.

Giuliana: Save us, Young Master Robert! You're our only hope!

Narrator: Once again he locates the antenna of the glider with his young eagle eyes. The bridge radios down to put the zodiac in the water. When Matt tries to start the engine, the batteries begin smoking!

All: The boat, the boat, the boat is on fire! / We don't need no water, let the mother***er burn! ("The Roof is on Fire")

Matt: Actually, we do kind of need the boat ...

Narrator: The zodiac comes back aboard, the batteries are replaced, and the boat is relaunched. The recovery team drives out in a tempest of blinding snow and howling winds.

All: Say it ain't so / Can't see through the snow / Winds're picking up / Man, does this blow! Na, na, na, na, na, na, na, na, na, na, na, na, na, na, na, na, na, na, na ("All the small things")

[Matt/Giuliana lassos Glider and brings her on board]

Narrator: Zodiac Jack hoists the glider into the boat and the team secures it and returns to the ship. All is well ... but wait! Catastrophe strikes the glider team. While climbing from the zodiac, Giuliana is plunged into the icy waters of Drake Passage!

All: Mamma mia! There she goes again! My my!

Matt: Just jump when I tell you!

Giuliana: Mamma mia! Here I go again! Sorry guys, swear I didn't mean to! ("Mamma Mia!")

Narrator: Both Giuliana and the glider are successfully brought aboard.

All: Sweet glider of mine, woah, woah, woah / Good times never seemed so good! [so good, so good, so good] / Science is sublime, woah, woah, woah / Who'd believe we ever would see you again. ("Sweet Caroline")

Narrator: And they all lived happily ever after!

All: [form a kickline] Start spreading the news, the glider's okay / Hope you enjoyed our show of it, ChinStrAP, ChinStrAP / Let's get underway, we'll get drunk in PA / Glad that you were a part of it, Boat Trash, Boat Trash / If we can get back here, We'll see you all next year / It's been a blast, ChinStrAP, ChinStrAP ("New York, New York")

BIBLIOGRAPHY

Alkire, MB et al. (2012). "Estimates of net community production and export using high-resolution, Lagrangian measurements of O_2, NO_3-, and POC through the evolution of a spring diatom bloom in the North Atlantic". In: *Deep Sea Research Part I: Oceanographic Research Papers* 64, pp. 157–174.

Alldredge, AL and C Gotschalk (1988). "In situ settling behavior of marine snow 1". In: *Limnology and Oceanography* 33.3, pp. 339–351.

Amante, C and BW Eakins (2009). "ETOPO 1 Arc-Minute Global Relief Model: Procedure". In: *Data Source and Analysis, National Oceanic and Atmospheric Administration NOAA*.

Archer, DE, G Eshel, A Winguth, W Broecker, R Pierrehumbert, M Tobis, and R Jacob (2000). "Atmospheric pCO_2 sensitivity to the biological pump in the ocean". In: *Global Biogeochemical Cycles* 14.4, pp. 1219–1230.

Armstrong, RA, CM Lee, JI Hedges, S Honjo, and SG Wakeham (2001). "A new, mechanistic model for organic carbon fluxes in the ocean based on the quantitative association of POC with ballast minerals". In: *Deep Sea Research Part II: Topical Studies in Oceanography* 49.1-3, pp. 219–236.

Arrigo, KR, GL van Dijken, and S Bushinsky (2008). "Primary production in the Southern Ocean, 1997–2006". In: *Journal of Geophysical Research: Oceans* 113.C8.

Arrigo, KR, D Worthen, A Schnell, and MP Lizotte (1998). "Primary production in Southern Ocean waters". In: *Journal of Geophysical Research: Oceans* 103.C8, pp. 15587–15600.

Asper, VL (1987). "Measuring the flux and sinking speed of marine snow aggregates". In: *Deep Sea Research Part A. Oceanographic Research Papers* 34.1, pp. 1–17.

Babiano, A, C Basdevant, and R Sadourny (1985). "Structure functions and dispersion laws in two-dimensional turbulence". In: *Journal of the Atmospheric Sciences* 42.9, pp. 941–949.

Bachman, SD, B Fox-Kemper, JR Taylor, and LN Thomas (2017). "Parameterization of Frontal Symmetric Instabilities. I: Theory for Resolved Fronts". In: *Ocean Modelling* 109, pp. 72–95. ISSN: 1463-5003. DOI: https://doi.org/10.1016/j.ocemod.2016.12.003.

Baker, ET, DA Tennant, RA Feely, GT Lebon, and SL Walker (2001). "Field and laboratory studies on the effect of particle size and composition on optical backscattering measurements in hydrothermal plumes". In: *Deep Sea Research Part I: Oceanographic Research Papers* 48.2, pp. 593–604.

Balwada, D, JH LaCasce, and KG Speer (2016). "Scale-dependent distribution of kinetic energy from surface drifters in the Gulf of Mexico". In: *Geophysical Research Letters* 43.20.

Balwada, D, KS Smith, and R Abernathey (2018). "Submesoscale Vertical Velocities Enhance Tracer Subduction in an Idealized Antarctic Circumpolar Current". In: *Geophysical Research Letters* 45.18, pp. 9790–9802.

Banse, K (2004). "Should we continue to use the 1% light depth convention for estimating the compensation depth of phytoplankton for another 70 years?" In: *Limnology and Oceanography Bulletin* 13.3, pp. 49–52.

Behrenfeld, MJ, E Boss, DA Siegel, and DM Shea (2005). "Carbon-based ocean productivity and phytoplankton physiology from space". In: *Global Biogeochemical Cycles* 19.1.

Behrenfeld, MJ and PG Falkowski (1997). "Photosynthetic rates derived from satellite-based chlorophyll concentration". In: *Limnology and Oceanography* 42.1, pp. 1–20.

Behrenfeld, MJ and AJ Milligan (2013). "Photophysiological expressions of iron stress in phytoplankton". In: *Annual Review of Marine Science* 5, pp. 217–246.

Berelson, WM (2001). "The flux of particulate organic carbon into the ocean interior: A comparison of four US JGOFS regional studies". In: *Oceanography* 14.4, pp. 59–67.

Boccaletti, G, R Ferrari, and B Fox-Kemper (2007). "Mixed Layer Instabilities and Restratification". In: *J. Phys. Oceanogr.* 37.9, pp. 2228–2250. DOI: 10.1175/JPO3101.1.

Boss, E and N Haëntjens (2016). "Primer regarding measurements of chlorophyll fluorescence and the backscattering coefficient with WETLabs FLBB on profiling floats." In:

Boss, E, N Haëntjens, TK Westberry, L Karp-Boss, and WH Slade (2018). "Validation of the particle size distribution obtained with the laser in-situ scattering and transmission (LISST) meter in flow-through mode". In: *Optics Express* 26.9, pp. 11125–11136.

Boss, E, D Swift, L Taylor, P Brickley, R Zaneveld, S Riser, MJ Perry, and PG Strutton (2008). "Observations of pigment and particle distributions in the western North Atlantic from an autonomous float and ocean color satellite". In: *Limnology and Oceanography* 53, pp. 2112–2122. ISSN: 1939-5590.

Boyd, PW and MJ Ellwood (2010). "The biogeochemical cycle of iron in the ocean". In: *Nature Geoscience* 3.10, p. 675.

Boyd, PW et al. (2000). "A mesoscale phytoplankton bloom in the polar Southern Ocean stimulated by iron fertilization". In: *Nature* 407.6805, p. 695.

Brainerd, KE and MC Gregg (1995). "Surface mixed and mixing layer depths". In: *Deep Sea Research Part I: Oceanographic Research Papers* 42.9, pp. 1521–1543.

Brannigan, L (2016). "Intense submesoscale upwelling in anticyclonic eddies". In: *Geophysical Research Letters* 43.7. 2016GL067926, pp. 3360–3369. ISSN: 1944-8007. DOI: 10.1002/2016GL067926.

Brannigan, L, DP Marshall, AC Naveira Garabato, AJ George Nurser, and J Kaiser (2017). "Submesoscale instabilities in mesoscale eddies". In: *Journal of Physical Oceanography* 2017.

Brannigan, L, DP Marshall, A Naveira-Garabato, and AJ George Nurser (2015). "The seasonal cycle of submesoscale flows". In: *Ocean Modelling* 92, pp. 69–84. DOI: 10.1016/j.ocemod.2015.05.002.

Briggs, NT, MJ Perry, I Cetinić, CM Lee, E D'Asaro, AM Gray, and E Rehm (2011). "High-resolution observations of aggregate flux during a sub-polar North Atlantic spring bloom". In: *Deep Sea Research Part I: Oceanographic Research Papers* 58.10, pp. 1031–1039. ISSN: 0967-0637. DOI: https://doi.org/10.1016/j.dsr.2011.07.007.

Briggs, NT, WH Slade, E Boss, and MJ Perry (2013). "Method for estimating mean particle size from high-frequency fluctuations in beam attenuation or scattering measurements". In: *Applied Optics* 52.27, pp. 6710–6725.

Broecker, WS et al. (1998). "How much deep water is formed in the Southern Ocean?" In: *Journal of Geophysical Research: Oceans* 103.C8, pp. 15833–15843. ISSN: 2156-2202. DOI: 10.1029/98JC00248.

Buckingham, CE et al. (2016). "Seasonality of submesoscale flows in the ocean surface boundary layer". In: *Geophysical Research Letters* 43.5. 2016GL068009, pp. 2118–2126. ISSN: 1944-8007. DOI: 10.1002/2016GL068009.

Buesseler, KO, MP Bacon, JK Cochran, and HD Livingston (1992). "Carbon and nitrogen export during the JGOFS North Atlantic Bloom Experiment estimated from 234Th: 238U disequilibria". In: *Deep Sea Research Part A. Oceanographic Research Papers* 39.7-8, pp. 1115–1137.

Buesseler, KO, L Ball, J Andrews, C Benitez-Nelson, R Belastock, F Chai, and Y Chao (1998). "Upper ocean export of particulate organic carbon in the Arabian Sea derived from thorium-234". In: *Deep Sea Research Part II: Topical Studies in Oceanography* 45.10-11, pp. 2461–2487.

Buesseler, KO and PW Boyd (2009). "Shedding light on processes that control particle export and flux attenuation in the twilight zone of the open ocean". In: *Limnology and Oceanography* 54.4, pp. 1210–1232.

Buesseler, KO et al. (2007). "An assessment of the use of sediment traps for estimating upper ocean particle fluxes". In: *Journal of Marine Research* 65.3, pp. 345–416.

Burd, AB and GA Jackson (2009). “Particle aggregation”. In: *Annual Review of Marine Science* 1, pp. 65–90.

Callies, J and R Ferrari (2013). “Interpreting energy and tracer spectra of upper-ocean turbulence in the submesoscale range (1-200 km)”. In: *J. Phys. Oceanogr.* 43, pp. 2456–2474.

Callies, J, R Ferrari, JM Klymak, and J Gula (2015). “Seasonality in submesoscale turbulence”. In: *Nature Communications* 6, p. 6862.

Callies, J, G Flierl, R Ferrari, and B Fox-Kemper (2016). “The role of mixed-layer instabilities in submesoscale turbulence”. In: *Journal of Fluid Mechanics* 788, pp. 5–41.

Capet, X, JC McWilliams, MJ Molemaker, and AF Shchepetkin (2008). “Mesoscale to submesoscale transition in the California Current System. Part I: Flow structure, eddy flux, and observational tests”. In: *J. Phys. Oceanogr.* 38.1, pp. 29–43.

Carlson, CA, HW Ducklow, and AF Michaels (1994). “Annual flux of dissolved organic carbon from the euphotic zone in the northwestern Sargasso Sea”. In: *Nature* 371.6496, p. 405.

Carr, ME et al. (2006). “A comparison of global estimates of marine primary production from ocean color”. In: *Deep Sea Research Part II: Topical Studies in Oceanography* 53.5-7, pp. 741–770.

Cassar, N et al. (2011). “The influence of iron and light on net community production in the Subantarctic and Polar Frontal Zones”. In: *Biogeosciences* 8.2, pp. 227–237.

Cetinić, I, MJ Perry, EA D’Asaro, NT Briggs, N Poulton, ME Sieracki, and CM Lee (2015). “A simple optical index shows spatial and temporal heterogeneity in phytoplankton community composition during the 2008 North Atlantic Bloom Experiment”. In: *Biogeosciences* 12.7, pp. 2179–2194. DOI: 10.5194/bg-12-2179-2015.

Charney, JG (1971). “Geostrophic turbulence”. In: *Journal of the Atmospheric Sciences* 28.6, pp. 1087–1095.

Cole, ST and DL Rudnick (2012). “The spatial distribution and annual cycle of upper ocean thermohaline structure”. In: *J. Geophys. Res.* 115, p. C04012. DOI: 10.1029/2009JC005654.

Cullen, JJ (1982). “The deep chlorophyll maximum: comparing vertical profiles of chlorophyll a”. In: *Canadian Journal of Fisheries and Aquatic Sciences* 39.5, pp. 791–803.

– (2015). “Subsurface chlorophyll maximum layers: enduring enigma or mystery solved?” In:

Cullen, JJ and MR Lewis (1995). "Biological processes and optical measurements near the sea surface: Some issues relevant to remote sensing". In: *Journal of Geophysical Research: Oceans* 100.C7, pp. 13255–13266. ISSN: 2156-2202. DOI: 10.1029/95JC00454.

Daly, KL, RH Bryne, AG Dickson, SM Gallager, MJ Perry, and MK Tivey (2004). "Chemical and biological sensors for time-series research: Current status and new directions". In: *Mar. Tech. Soc. J.* 38, p. 121.

Damerell, GM, KJ Heywood, AF Thompson, U Binetti, and J Kaiser (2016). "The vertical structure of upper ocean variability at the Porcupine Abyssal Plain during 2012–2013". In: *J. Geophys. Res., Oc.* 121.5, pp. 3075–3089.

Danabasoglu, G et al. (2014). "North Atlantic simulations in coordinated ocean-ice reference experiments phase II (CORE-II). Part I: mean states". In: *Ocean Modelling* 73, pp. 76–107.

de Boyer Montégut, C, G Madec, AS Fischer, A Lazar, and D Iudicone (2004). "Mixed layer depth over the global ocean: An examination of profile data and a profile-based climatology". In: *Journal of Geophysical Research: Oceans* 109.C12.

Dekshenieks, MM, PL Donaghay, JM Sullivan, JEB Rines, TR Osborn, and MS Twardowski (2001). "Temporal and spatial occurrence of thin phytoplankton layers in relation to physical processes". In: *Marine Ecology Progress Series* 223, pp. 61–71.

Dong, S, J Sprintall, ST Gille, and L Talley (2008). "Southern Ocean mixed-layer depth from Argo float profiles". In: *Journal of Geophysical Research: Oceans* 113.C6.

du Plessis, M, S Swart, IJ Ansorge, and A Mahadevan (2017). "Submesoscale processes promote seasonal restratification in the s ubantarctic o cean". In: *Journal of Geophysical Research: Oceans* 122.4, pp. 2960–2975.

Ducklow, HW, DK Steinberg, and KO Buesseler (2001). "Upper ocean carbon export and the biological pump". In: *Oceanography* 14.4, pp. 50–58.

Dulaiova, H, MV Ardelan, PB Henderson, and MA Charette (2009). "Shelf-derived iron inputs drive biological productivity in the southern Drake Passage". In: *Global Biogeochemical Cycles* 23.4.

Dunne, JP, RA Armstrong, A Gnanadesikan, and JL Sarmiento (2005). "Empirical and mechanistic models for the particle export ratio". In: *Global Biogeochemical Cycles* 19.4.

Eppley, RW, E Stewart, MR Abbott, and U Heyman (1985). "Estimating ocean primary production from satellite chlorophyll. Introduction to regional differences and statistics for the Southern California Bight". In: *Journal of Plankton Research* 7.1, pp. 57–70.

Erickson, ZK and AF Thompson (2018). "The seasonality of physically driven export at submesoscales in the Northeast Atlantic Ocean". In: *Global Biogeochemical Cycles* 32.8, pp. 1144–1162. DOI: 10.1029/2018GB005927.

Erickson, ZK, AF Thompson, N Cassar, J Sprintall, and MR Mazloff (2016). "An advective mechanism for deep chlorophyll maxima formation in southern Drake Passage". In: *Geophysical Research Letters* 43.20, pp. 10–846. DOI: 10.1002/2016GL070565.

Eriksen, CC, TJ Osse, RD Light, T Wen, TW Lehman, PL Sabin, JW Ballard, and AM Chiodi (2001). "Seaglider: A long-range autonomous underwater vehicle for oceanographic research". In: *IEEE Journal of Oceanic Engineering* 26.4, pp. 424–436.

Estapa, ML, DA Siegel, KO Buesseler, RHR Stanley, MW Lomas, and NB Nelson (2015). "Decoupling of net community and export production on submesoscales in the Sargasso Sea". In: *Global Biogeochemical Cycles* 29.8, pp. 1266–1282.

Ferrari, R, ST Merrifield, and JR Taylor (2015). "Shutdown of convection triggers increase of surface chlorophyll". In: *Journal of Marine Systems* 147, pp. 116–122.

Ferrari, R and C Wunsch (2009). "Ocean circulation kinetic energy: Reservoirs, sources, and sinks". In: *Annual Review of Fluid Mechanics* 41.

Field, CB, MJ Behrenfeld, JT Randerson, and P Falkowski (1998). "Primary Production of the Biosphere: Integrating Terrestrial and Oceanic Components". In: *Science* 281.5374, pp. 237–240. ISSN: 0036-8075. DOI: 10.1126/science.281.5374.237.

Fox-Kemper, B, G Danabasoglu, R Ferrari, SM Griffies, RW Hallberg, MM Holland, ME Maltrud, S Peacock, and BL Samuels (2011). "Parameterization of mixed layer eddies. III: Implementation and impact in global ocean climate simulations". In: *Ocean Modelling* 39.1-2, pp. 61–78.

Fox-Kemper, B, R Ferrari, and R Hallberg (2008). "Parameterization of Mixed Layer Eddies. Part I: Theory and Diagnosis". In: *Journal of Physical Oceanography* 38.6, pp. 1145–1165. DOI: 10.1175/2007JPO3792.1.

Frajka-Williams, E, CC Eriksen, PB Rhines, and RR Harcourt (2011). "Determining vertical water velocities from Seaglider". In: *Journal of Atmospheric and Oceanic Technology* 28.12, pp. 1641–1656.

Frants, M, ST Gille, Ma Hatta, WT Hiscock, M Kahru, CI Measures, B Mitchell, and M Zhou (2013). "Analysis of horizontal and vertical processes contributing to natural iron supply in the mixed layer in southern Drake Passage". In: *Deep Sea Research Part II: Topical Studies in Oceanography* 90, pp. 68–76.

Frenger, I, M Münnich, N Gruber, and R Knutti (2015). "Southern Ocean eddy phenomenology". In: *Journal of Geophysical Research: Oceans* 120.11, pp. 7413–7449.

Garrett, C and W Munk (1975). “Space-time scales of internal waves: A progress report”. In: *J. Geophys. Res.* 80, pp. 291–297.

Gebbie, G and P Huybers (2011). “How is the ocean filled?” In: *Geophysical Research Letters* 38.6. L06604. ISSN: 1944-8007. DOI: 10.1029/2011GL046769.

Gent, PR et al. (2011). “The community climate system model version 4”. In: *Journal of Climate* 24.19, pp. 4973–4991.

Gordon, HR and WR McCluney (1975). “Estimation of the depth of sunlight penetration in the sea for remote sensing”. In: *Applied Optics* 14.2, pp. 413–416.

Gruber, N et al. (2009). “Oceanic sources, sinks, and transport of atmospheric CO2”. In: *Global Biogeochemical Cycles* 23.1.

Guidi, L, L Stemmann, GA Jackson, F Ibanez, H Claustre, L Legendre, M Picheral, and G Gorskya (2009). “Effects of phytoplankton community on production, size, and export of large aggregates: A world-ocean analysis”. In: *Limnology and Oceanography* 54.6, pp. 1951–1963.

Haine, TWN and J Marshall (1998). “Gravitational, symmetric, and baroclinic instability of the ocean mixed layer”. In: *Journal of Physical Oceanography* 28.4, pp. 634–658.

Hartman, SE, KE Larkin, RS Lampitt, M Lankhorst, and DJ Hydes (2010). “Seasonal and inter-annual biogeochemical variations in the Porcupine Abyssal Plain 2003-2005 associated with winter mixing and surface circulation”. In: *Deep-Sea Res. II* 57.15, pp. 1303–1312. ISSN: 0967-0645. DOI: 10.1016/j.dsr2.2010.01.007.

Hemsley, VS, TJ Smyth, AP Martin, E Frajka-Williams, AF Thompson, G Damerell, and SC Painter (2015). “Estimating Oceanic Primary Production Using Vertical Irradiance and Chlorophyll Profiles from Ocean Gliders in the North Atlantic”. In: *Environmental Science & Technology* 49.19, pp. 11612–11621. DOI: 10.1021/acs.est.5b00608.

Henson, SA, R Sanders, and E Madsen (2012). “Global patterns in efficiency of particulate organic carbon export and transfer to the deep ocean”. In: *Global Biogeochemical Cycles* 26.1.

Henson, SA and AC Thomas (2008). “A census of oceanic anticyclonic eddies in the Gulf of Alaska”. In: *Deep Sea Research Part I: Oceanographic Research Papers* 55.2, pp. 163–176.

Holm-Hansen, O and CD Hewes (2004). “Deep chlorophyll-a maxima (DCMs) in Antarctic waters”. In: *Polar Biology* 27.11, pp. 699–710.

Holm-Hansen, O, M Kahru, and CD Hewes (2005). “Deep chlorophyll a maxima (DCMs) in pelagic Antarctic waters. II. Relation to bathymetric features and dissolved iron concentrations”. In: *Marine Ecology Progress Series* 297, pp. 71–81.

Holm-Hansen, O and BG Mitchell (1991). “Spatial and temporal distribution of phytoplankton and primary production in the western Bransfield Strait region”. In: *Deep Sea Research Part A. Oceanographic Research Papers* 38.8-9, pp. 961–980.

Hood, RR, MR Abbott, and A Huyer (1991). “Phytoplankton and photosynthetic light response in the Coastal Transition Zone off northern California in June 1987”. In: *Journal of Geophysical Research: Oceans* 96.C8, pp. 14769–14780. ISSN: 2156-2202. DOI: 10.1029/91JC01208.

Hoskins, BJ (1974). “The role of potential vorticity in symmetric stability and instability”. In: *Quarterly Journal of the Royal Meteorological Society* 100.425, pp. 480–482.

Hua, BL, C Ménesguen, S le Gentil, R Schopp, B Marsset, and H Aiki (2013). “Layering and turbulence surrounding an anticyclonic oceanic vortex: in situ observations and quasi-geostrophic numerical simulations”. In: *Journal of Fluid Mechanics* 731, pp. 418–442.

Hurrell, JW et al. (2013). “The community earth system model: a framework for collaborative research”. In: *Bulletin of the American Meteorological Society* 94.9, pp. 1339–1360.

IPCC (2013). “Climate Change 2013: The Physical Science Basis. Contribution of Working Group I to the Fifth Assessment Report of the Intergovernmental Panel on Climate Change”. In:

Itoh, S and DL Rudnick (2017). “Fine-scale variability of isopycnal salinity in the California Current System”. In: *Journal of Geophysical Research: Oceans* 122.9, pp. 7066–7081.

Jacox, MG, CA Edwards, M Kahru, DL Rudnick, and RM Kudela (2015). “The potential for improving remote primary productivity estimates through subsurface chlorophyll and irradiance measurement”. In: *Deep Sea Research Part II: Topical Studies in Oceanography* 112.Supplement C, pp. 107–116. ISSN: 0967-0645. DOI: https://doi.org/10.1016/j.dsr2.2013.12.008.

Johnson, R, PG Strutton, SW Wright, A McMinn, and KM Meiners (2013). “Three improved satellite chlorophyll algorithms for the Southern Ocean”. In: *Journal of Geophysical Research: Oceans* 118.7, pp. 3694–3703.

Kadko, DC, L Washburn, and B Jones (1991). “Evidence of subduction within cold filaments of the northern California coastal transition zone”. In: *Journal of Geophysical Research: Oceans* 96.C8, pp. 14909–14926.

Kahru, M and BG Mitchell (2010). “Blending of ocean colour algorithms applied to the Southern Ocean”. In: *Remote Sensing Letters* 1.2, pp. 119–124.

Kautsky, H and A Hirsch (1931). “Neue versuche zur kohlensäureassimilation”. In: *Naturwissenschaften* 19.48, pp. 964–964.

Klein, P, BL Hua, G Lapeyre, X Capet, S le Gentil, and H Sasaki (2008). "Upper ocean turbulence from high-resolution 3D simulations". In: *J. Phys. Oceanogr.* 38.8, pp. 1748–1763.

Klein, P, AM Treguier, and BL Hua (1998). "Three-dimensional stirring of thermohaline fronts". In: *Journal of Marine Research* 56.3, pp. 589–612.

Klymak, JM, W Crawford, MH Alford, JA MacKinnon, and R Pinkel (2015). "Along-isopycnal variability of spice in the North Pacific". In: *J. Geophys. Res.* 120, pp. 2287–2307. DOI: 10.1002/2013JC009421.

Klymak, JM et al. (2016). "Submesoscale streamers exchange water on the north wall of the Gulf Stream". In: *Geophysical Research Letters* 43.3, pp. 1226–1233.

Kostadinov, TS, DA Siegel, and S Maritorena (2009). "Retrieval of the particle size distribution from satellite ocean color observations". In: *Journal of Geophysical Research: Oceans* 114.C9. ISSN: 2156-2202. DOI: 10.1029/2009JC005303.

Kunze, E, JM Klymak, RC Lien, R Ferrari, CM Lee, MA Sundermeyer, and L Goodman (2015). "Submesoscale water-mass spectra in the Sargasso Sea". In: *Journal of Physical Oceanography* 45.5, pp. 1325–1338.

Lacour, L, M Ardyna, KF Stec, H Claustre, L Prieur, A Poteau, MR D'Alcala, and D Iudicone (2017). "Unexpected winter phytoplankton blooms in the North Atlantic subpolar gyre". In: *Nat. Geosci.* 10. DOI: 10.1038/ngeo3035.

Lampitt, RS, I Salter, BA de Cuevas, SE Hartman, KE Larkin, and CA Pebody (2010). "Long-term variability of downward particle flux in the deep northeast Atlantic: Causes and trends". In: *Deep Sea Research Part II: Topical Studies in Oceanography* 57.15, pp. 1346–1361. ISSN: 0967-0645. DOI: https://doi.org/10.1016/j.dsr2.2010.01.011.

Lapeyre, G, P Klein, and BL Hua (2006). "Oceanic restratification forced by surface frontogenesis". In: *Journal of Physical Oceanography* 36.8, pp. 1577–1590.

Large, WG and SG Yeager (2009). "The global climatology of an interannually varying air–sea flux data set". In: *Climate Dynamics* 33.2-3, pp. 341–364.

Laws, EA, PG Falkowski, WO Smith, H Ducklow, and JJ McCarthy (2000). "Temperature effects on export production in the open ocean". In: *Global Biogeochemical Cycles* 14.4, pp. 1231–1246. ISSN: 1944-9224. DOI: 10.1029/1999GB001229.

le Quéré, C et al. (2018). "Global carbon budget 2018". In: *Earth System Science Data (Online)* 10.4.

Lévy, M, R Ferrari, PJS Franks, AP Martin, and P Rivière (2012). "Bringing physics to life at the submesoscale". In: *Geophys. Res. Lett.* 39.14.

Lévy, M, P Klein, and AM Treguier (2001). "Impact of sub-mesoscale physics on production and subduction of phytoplankton in an oligotrophic regime". In: *Journal of Marine Research* 59.4, pp. 535–565.

Longhurst, AR, AW Bedo, WG Harrison, EJH Head, and DD Sameoto (1990). "Vertical flux of respiratory carbon by oceanic diel migrant biota". In: *Deep Sea Research Part A. Oceanographic Research Papers* 37.4, pp. 685–694.

Longhurst, AR and WG Harrison (1989). "The biological pump: profiles of plankton production and consumption in the upper ocean". In: *Progress in Oceanography* 22.1, pp. 47–123.

Mahadevan, A (2016). "The impact of submesoscale physics on primary productivity of plankton". In: *Annual Review of Marine Science* 8, pp. 161–184.

Mahadevan, A and DE Archer (2000). "Modeling the impact of fronts and mesoscale circulation on the nutrient supply and biogeochemistry of the upper ocean". In: *Journal of Geophysical Research: Oceans* 105.C1, pp. 1209–1225. ISSN: 2156-2202. DOI: 10.1029/1999JC900216.

Mahadevan, A, EA D'Asaro, CM Lee, and MJ Perry (2012). "Eddy-driven stratification initiates North Atlantic spring phytoplankton blooms". In: *Science* 337.6090, pp. 54–58.

Mahadevan, A and A Tandon (2006). "An analysis of mechanisms for submesoscale vertical motion at ocean fronts". In: *Ocean Modelling* 14, pp. 241–256. DOI: 10.1016/j.ocemod.2006.05.006.

Marshall, J, A Adcroft, C Hill, L Perelman, and C Heisey (1997). "A finite-volume, incompressible Navier Stokes model for studies of the ocean on parallel computers". In: *Journal of Geophysical Research: Oceans* 102.C3, pp. 5753–5766.

Marshall, J, D Olbers, H Ross, and D Wolf-Gladrow (1993). "Potential vorticity constraints on the dynamics and hydrography of the Southern Ocean". In: *Journal of Physical Oceanography* 23.3, pp. 465–487.

Marshall, J and T Radko (2003). "Residual-mean solutions for the Antarctic Circumpolar Current and its associated overturning circulation". In: *Journal of Physical Oceanography* 33.11, pp. 2341–2354.

Martin, AP, MI Lucas, SC Painter, R Pidcock, H Prandke, Ho Prandke, and MC Stinchcombe (2010). "The supply of nutrients due to vertical turbulent mixing: A study at the Porcupine Abyssal Plain study site in the northeast Atlantic". In: *Deep Sea Research Part II: Topical Studies in Oceanography* 57.15, pp. 1293–1302. ISSN: 0967-0645. DOI: https://doi.org/10.1016/j.dsr2.2010.01.006.

Martin, JH (1990). "Glacial-interglacial CO2 change: The iron hypothesis". In: *Paleoceanography* 5.1, pp. 1–13.

Martin, JH, RM Gordon, and SE Fitzwater (1990). "Iron in Antarctic waters". In: *Nature* 345.6271, p. 156.

Martin, JH, GA Knauer, DM Karl, and WW Broenkow (1987). "VERTEX: carbon cycling in the northeast Pacific". In: *Deep Sea Research Part A. Oceanographic Research Papers* 34.2, pp. 267–285.

Mazloff, MR, P Heimbach, and C Wunsch (2010). "An eddy-permitting Southern Ocean state estimate". In: *Journal of Physical Oceanography* 40.5, pp. 880–899.

McCaffrey, K, B Fox-Kemper, and G Forget (2015). "Estimates of ocean macroturbulence: Structure function and spectral slope from Argo profiling floats". In: *J. Phys. Oceanogr.* 45, pp. 1773–1793. DOI: 10.1175/JPO-D-14-0023.1.

McCartney, MS and LD Talley (1982). "The subpolar mode water of the North Atlantic Ocean". In: *Journal of Physical Oceanography* 12.11, pp. 1169–1188.

McDougall, TJ and OA Krzysik (2015). "Spiciness". In: *Journal of Marine Research* 73.5, pp. 141–152.

McWilliams, JC (1985). "Submesoscale, coherent vortices in the ocean". In: *Reviews of Geophysics* 23.2, pp. 165–182.

– (2016). "Submesoscale currents in the ocean". In: *Proc. R. Soc. A*. Vol. 472. 2189. The Royal Society, p. 20160117.

Measures, CI, MT Brown, KE Selph, A Apprill, M Zhou, M Hatta, and WT Hiscock (2013). "The influence of shelf processes in delivering dissolved iron to the HNLC waters of the Drake Passage, Antarctica". In: *Deep Sea Research Part II: Topical Studies in Oceanography* 90, pp. 77–88.

Mendes, CRB, MS de Souza, VMT Garcia, MC Leal, V Brotas, and CAE Garcia (2012). "Dynamics of phytoplankton communities during late summer around the tip of the Antarctic Peninsula". In: *Deep Sea Research Part I: Oceanographic Research Papers* 65, pp. 1–14.

Menemenlis, D, J Campin, P Heimbach, C Hill, T Lee, A Nguyen, M Schodlok, and H Zhang (2008). "ECCO2: High resolution global ocean and sea ice data synthesis". In: *Mercator Ocean Quarterly Newsletter* 31, pp. 13–21.

Mensa, JA, Z Garraffo, A Griffa, TM Özgökmen, A Haza, and M Veneziani (2013). "Seasonality of the submesoscale dynamics in the Gulf Stream region". In: *Ocean Dynamics* 63.8, pp. 923–941.

Miles, JW (1961). "On the stability of heterogeneous shear flows". In: *Journal of Fluid Mechanics* 10.4, pp. 496–508.

Mitchell, BG, EA Brody, O Holm-Hansen, C McClain, and J Bishop (1991). "Light limitation of phytoplankton biomass and macronutrient utilization in the Southern Ocean". In: *Limnology and Oceanography* 36.8, pp. 1662–1677.

Mitchell, BG and O Holm-Hansen (1991). "Bio-optical properties of Antarctic Peninsula waters: Differentiation from temperate ocean models". In: *Deep Sea Research Part A. Oceanographic Research Papers* 38.8-9, pp. 1009–1028.

Molemaker, MJ, JC McWilliams, and WK Dewar (2015). "Submesoscale Instability and Generation of Mesoscale Anticyclones near a Separation of the California Undercurrent". In: *Journal of Physical Oceanography* 45.3, pp. 613–629. DOI: 10.1175/JPO-D-13-0225.1.

Morel, A and JF Berthon (1989). “Surface pigments, algal biomass profiles, and potential production of the euphotic layer: Relationships reinvestigated in view of remote-sensing applications”. In: *Limnology and Oceanography* 34.8, pp. 1545–1562.

Munk, W (1981). “Internal waves and small-scale processes”. In: *Evolution of Physical Oceanography*. Ed. by B. A. Warren and C. Wunsch. The MIT Press, pp. 264–291.

Neori, A, O Holm-Hansen, BG Mitchell, and DA Kiefer (1984). “Photoadaptation in marine phytoplankton”. In: *Plant Physiology* 76.2, pp. 518–524.

Omand, MM, EA D’Asaro, CM Lee, MJ Perry, NT Briggs, I Cetinić, and A Mahadevan (2015). “Eddy-driven subduction exports particulate organic carbon from the spring bloom”. In: *Science* 348, pp. 222–225.

Orsi, AH, T Whitworth III, and WD Nowlin Jr. (1995). “On the meridional extent and fronts of the Antarctic Circumpolar Current”. In: *Deep Sea Research Part I: Oceanographic Research Papers* 42.5, pp. 641–673.

Painter, SC, MI Lucas, MC Stinchcombe, TS Bibby, and AJ Poulton (2010). “Summertime trends in pelagic biogeochemistry at the Porcupine Abyssal Plain study site in the northeast Atlantic”. In: *Deep Sea Research Part II: Topical Studies in Oceanography* 57.15, pp. 1313–1323.

Passow, U and CA Carlson (2012). “The biological pump in a high CO2 world”. In: *Marine Ecology Progress Series* 470, pp. 249–271.

Prézelin, BB, EE Hofmann, C Mengelt, and JM Klinck (2000). “The linkage between Upper Circumpolar Deep Water (UCDW) and phytoplankton assemblages on the west Antarctic Peninsula continental shelf”. In: *Journal of Marine Research* 58.2, pp. 165–202.

Price, JF, RA Weller, and R Pinkel (1986). “Diurnal cycling: Observations and models of the upper ocean response to diurnal heating, cooling, and wind mixing”. In: *Journal of Geophysical Research: Oceans* 91.C7, pp. 8411–8427.

Qiu, B, S Chen, P Klein, J Wang, H Torres, LL Fu, and D Menemenlis (2018). “Seasonality in Transition Scale from Balanced to Unbalanced Motions in the World Ocean”. In: *Journal of Physical Oceanography* 48.3, pp. 591–605.

Ralston, DK, DJ McGillicuddy Jr., and DW Townsend (2007). “Asynchronous vertical migration and bimodal distribution of motile phytoplankton”. In: *Journal of Plankton Research* 29.9, pp. 803–821.

Richardson, TL and JJ Cullen (1995). “Changes in buoyancy and chemical composition during growth of a coastal marine diatom: ecological and biogeochemical consequences”. In: *Marine Ecology Progress Series* 128, pp. 77–90.

Richardson, TL and GA Jackson (2007). “Small phytoplankton and carbon export from the surface ocean”. In: *Science* 315.5813, pp. 838–840.

Rieck, JK, CW Böning, RJ Greatbatch, and M Scheinert (2015). "Seasonal variability of eddy kinetic energy in a global high-resolution ocean model". In: *Geophys. Res. Lett.* 42, pp. 9379–9386. DOI: 10.1002/2015GL066152.

Rocha, CB, TK Chereskin, ST Gille, and D Menemenlis (2016a). "Mesoscale to submesoscale wavenumber spectra in Drake Passage". In: *J. Phys. Oceanogr.* 46, pp. 601–620. DOI: 10.1175/JPO-D-15-0087.1.

Rocha, CB, ST Gille, TK Chereskin, and D Menemenlis (2016b). "Seasonality of submesoscale dynamics in the Kuroshio Extension". In: *Geophys. Res. Lett.* 43. DOI: 10.1002/2016GL071349.

Roesler, C et al. (2017). "Recommendations for obtaining unbiased chlorophyll estimates from in situ chlorophyll fluorometers: A global analysis of WET Labs ECO sensors". In: *Limnology and Oceanography: Methods* 15.6, pp. 572–585. ISSN: 1541-5856. DOI: 10.1002/lom3.10185.

Rosso, I, AC Hogg, AE Kiss, and B Gayen (2015). "Topographic influence on submesoscale dynamics in the Southern Ocean". In: *Geophysical Research Letters* 42.4, pp. 1139–1147.

Rosso, I, AC Hogg, PG Strutton, AE Kiss, R Matear, A Klocker, and E van Sebille (2014). "Vertical transport in the ocean due to sub-mesoscale structures: Impacts in the Kerguelen region". In: *Oc. Modell.* 80, pp. 10–23. DOI: 10.1016/j.ocemod.2014.05.001.

Roullet, G, X Capet, and G Maze (2014). "Global interior eddy available potential energy diagnosed from Argo floats". In: *Geophys. Res. Lett.* 41, pp. 1651–1656. DOI: 10.1002/2013GL059004.

Rudnick, DL (2001). "On the skewness of vorticity in the upper ocean". In: *Geophysical Research Letters* 28.10, pp. 2045–2048.

– (2016). "Ocean research enabled by underwater gliders". In: *Annual Review of Marine Science* 8, pp. 519–541.

Rumyantseva, A, N Lucas, T Rippeth, A Martin, SC Painter, TJ Boyd, and S Henson (2015). "Ocean nutrient pathways associated with the passage of a storm". In: *Global Biogeochemical Cycles* 29.8, pp. 1179–1189. ISSN: 1944-9224. DOI: 10.1002/2015GB005097.

Ryther, JH (1956). "Photosynthesis in the Ocean as a Function of Light Intensity 1". In: *Limnology and Oceanography* 1.1, pp. 61–70.

Sarmiento, JL (1983). "A tritium box model of the North Atlantic thermocline". In: *Journal of Physical Oceanography* 13.7, pp. 1269–1274.

Sarmiento, JL, G Thiele, RM Key, and WS Moore (1990). "Oxygen and nitrate new production and remineralization in the North Atlantic subtropical gyre". In: *Journal of Geophysical Research: Oceans* 95.C10, pp. 18303–18315.

Sarmiento, JL and JR Toggweiler (1984). "A new model for the role of the oceans in determining atmospheric pCO2". In: *Nature* 308.5960, p. 621.

Sasaki, H, P Klein, B Qiu, and Y Sasai (2014). "Impact of oceanic-scale interactions on the seasonal modulation of ocean dynamics by the atmosphere". In: *Nat. Comm.* 5. DOI: 10.1038/ncomms6636.

Schönau, MC and DL Rudnick (2015). "Glider observations of the North Equatorial Current in the western tropical Pacific". In: *Journal of Geophysical Research: Oceans* 120.5, pp. 3586–3605.

Siegel, DA, KO Buesseler, SC Doney, SF Sailley, MJ Behrenfeld, and PW Boyd (2014). "Global assessment of ocean carbon export by combining satellite observations and food-web models". In: *Global Biogeochemical Cycles* 28.3, pp. 181–196.

Siegel, DA et al. (2016). "Prediction of the export and fate of global ocean net primary production: the EXPORTS science plan". In: *Frontiers in Marine Science* 3, p. 22.

Slovacek, RE and PJ Hannan (1977). "In vivo fluorescence determinations of phytoplankton chlorophyll a". In: *Limnology and Oceanography* 22.5, pp. 919–925.

Smith, KS and R Ferrari (2009). "The production and dissipation of compensated thermohaline variance by mesoscale stirring". In: *J. Phys. Oceanogr.* 39.10, pp. 2477–2501.

Sokolov, S and SR Rintoul (2009). "Circumpolar structure and distribution of the Antarctic Circumpolar Current fronts: 1. Mean circumpolar paths". In: *Journal of Geophysical Research: Oceans* 114.C11.

Stacey, MT, MA McManus, and JV Steinbuck (2007). "Convergences and divergences and thin layer formation and maintenance". In: *Limnology and Oceanography* 52.4, pp. 1523–1532.

Steinberg, DK, CA Carlson, NR Bates, SA Goldthwait, LP Madin, and AF Michaels (2000). "Zooplankton vertical migration and the active transport of dissolved organic and inorganic carbon in the Sargasso Sea". In: *Deep Sea Research Part I: Oceanographic Research Papers* 47.1, pp. 137–158.

Stemmann, L, GA Jackson, and D Ianson (2004). "A vertical model of particle size distributions and fluxes in the midwater column that includes biological and physical processes—Part I: model formulation". In: *Deep Sea Research Part I: Oceanographic Research Papers* 51.7, pp. 865–884.

Stommel, H (1979). "Determination of water mass properties of water pumped down from the Ekman layer to the geostrophic flow below". In: *Proceedings of the National Academy of Sciences* 76.7, pp. 3051–3055.

Stone, PH (1972). "On non-geostrophic baroclinic stability: Part III. The momentum and heat transports". In: *Journal of the Atmospheric Sciences* 29.3, pp. 419–426.

Stramski, D et al. (2008). “Relationships between the surface concentration of particulate organic carbon and optical properties in the eastern South Pacific and eastern Atlantic Oceans”. In: *Biogeosciences* 5.1, pp. 171–201.

Stukel, MR, E Asher, N Couto, O Schofield, S Strebel, P Tortell, and HW Ducklow (2015). “The imbalance of new and export production in the Western Antarctic Peninsula, a potentially “leaky” ecosystem”. In: *Global Biogeochemical Cycles* 29.9, pp. 1400–1420.

Stukel, MR et al. (2017). “Mesoscale ocean fronts enhance carbon export due to gravitational sinking and subduction”. In: *Proceedings of the National Academy of Sciences* 114.6, pp. 1252–1257.

Su, Z, J Wang, P Klein, AF Thompson, and D Menemenlis (2018). “Ocean submesoscales as a key component of the global heat budget”. In: *Nature Communications* 9.1, p. 775.

Sverdrup, HU (1953). “On Conditions for the Vernal Blooming of Phytoplankton”. In: *ICES Journal of Marine Science* 18.3, pp. 287–295. DOI: 10.1093/icesjms/18.3.287.

Takahashi, K, A Kuwata, H Sugisaki, K Uchikawa, and H Saito (2009). “Downward carbon transport by diel vertical migration of the copepods Metridia pacifica and Metridia okhotensis in the Oyashio region of the western subarctic Pacific Ocean”. In: *Deep Sea Research Part I: Oceanographic Research Papers* 56.10, pp. 1777–1791.

Taylor, JR (2018). “Accumulation and subduction of buoyant material at submesoscale fronts”. In: *Journal of Physical Oceanography* 48.6, pp. 1233–1241.

Taylor, JR and R Ferrari (2009). “On the equilibration of a symmetrically unstable front via a secondary shear instability”. In: *Journal of Fluid Mechanics* 622, pp. 103–113. DOI: 10.1017/S0022112008005272.

– (2010). “Buoyancy and wind-driven convection at mixed layer density fronts”. In: *Journal of Physical Oceanography* 40.6, pp. 1222–1242.

– (2011). “Shutdown of turbulent convection as a new criterion for the onset of spring phytoplankton blooms”. In: *Limnology and Oceanography* 56.6, pp. 2293–2307. ISSN: 1939-5590. DOI: 10.4319/lo.2011.56.6.2293. URL: http://dx.doi.org/10.4319/lo.2011.56.6.2293.

Thomas, LN (2005). “Destruction of potential vorticity by winds”. In: *Journal of Physical Oceanography* 35.12, pp. 2457–2466.

Thomas, LN and CM Lee (2005). “Intensification of ocean fronts by down-front winds”. In: *Journal of Physical Oceanography* 35.6, pp. 1086–1102.

Thomas, LN, JR Taylor, EA D’Asaro, CM Lee, JM Klymak, and A Shcherbina (2016). “Symmetric instability, inertial oscillations, and turbulence at the Gulf Stream front”. In: *J. Phys. Oceanogr.* 46.1, pp. 197–217.

Thomas, LN, JR Taylor, R Ferrari, and TM Joyce (2013). "Symmetric instability in the Gulf Stream". In: *Deep-Sea. Res. II* 91, pp. 96–110.

Thompson, AF, PH Haynes, C Wilson, and KJ Richards (2010). "Rapid Southern Ocean front transitions in an eddy-resolving ocean GCM". In: *Geophysical Research Letters* 37.23.

Thompson, AF, A Lazar, C Buckingham, AC Naveira Garabato, GM Damerell, and KJ Heywood (2016). "Open-ocean submesoscale motions: A full seasonal cycle of mixed layer instabilities from gliders". In: *J. Phys. Oceanogr.* 46.4, pp. 1285–1307.

Tjiputra, JF, C Roelandt, M Bentsen, DM Lawrence, T Lorentzen, J Schwinger, O Seland, and C Heinze (2013). "Evaluation of the carbon cycle components in the Norwegian Earth System Model (NorESM)". In: *Geoscientific Model Development* 6.2, p. 301.

Torres, HS, P Klein, D Menemenlis, B Qiu, Z Su, J Wang, S Chen, and LL Fu (2018). "Partitioning ocean motions into balanced motions and internal gravity waves: A modeling study in anticipation of future space missions". In: *Journal of Geophysical Research: Oceans*.

Umberto, B (2016). "Dissolved oxygen-based annual biological production from glider observations at the Porcupine Abyssal Plain (North Atlantic)". PhD thesis. U. East Anglia.

Vallis, GK (2006). *Atmospheric and Oceanic Fluid Dynamics: Fundamentals and Large-Scale Circulation (Cambridge*.

Veronis, G (1972). "Properties of seawater defined by temperature, salinity, and pressure". In: *J. Mar. Res.* 30.2, p. 227.

Viglione, GA, AF Thompson, MM Flexas, J Sprintall, and S Swart (2018). "Abrupt Transitions in Submesoscale Structure in Southern Drake Passage Maybe: Glider Observations and Model Results". In: *J. Phys. Oceanogr.*

Wang, J, LL Fu, B Qiu, D Menemenlis, JT Farrar, Y Chao, AF Thompson, and MM Flexas (2018). "An Observing System Simulation Experiment for the Calibration and Validation of the Surface Water Ocean Topography Sea Surface Height Measurement Using In Situ Platforms". In: *Journal of Atmospheric and Oceanic Technology* 35.2, pp. 281–297.

Washburn, L, DC Kadko, BH Jones, T Hayward, PM Kosro, TP Stanton, S Ramp, and T Cowles (1991). "Water mass subduction and the transport of phytoplankton in a coastal upwelling system". In: *Journal of Geophysical Research: Oceans* 96.C8, pp. 14927–14945. ISSN: 2156-2202. DOI: 10.1029/91JC01145.

Webb, EK (1964). "Ratio of spectrum and structure-function constants in the inertial subrange". In: *Quarterly Journal of the Royal Meteorological Society* 90.385, pp. 344–346.

Weston, K, L Fernand, DK Mills, R Delahunty, and J Brown (2005). "Primary production in the deep chlorophyll maximum of the central North Sea". In: *Journal of Plankton Research* 27.9, pp. 909–922.

Whitt, DB, JR Taylor, and M Lévy (2017). "Synoptic-to-planetary scale wind variability enhances phytoplankton biomass at ocean fronts". In: *Journal of Geophysical Research: Oceans*.

Xing, X, NT Briggs, E Boss, and H Claustre (2018). "Improved correction for non-photochemical quenching of in situ chlorophyll fluorescence based on a synchronous irradiance profile". In: *Optics Express* 26.19, pp. 24734–24751.

Xing, X, A Morel, H Claustre, D Antoine, F D'Ortenzio, A Poteau, and A Mignot (2011). "Combined processing and mutual interpretation of radiometry and fluorimetry from autonomous profiling Bio-Argo floats: Chlorophyll a retrieval". In: *Journal of Geophysical Research: Oceans* 116.C6. ISSN: 2156-2202. DOI: 10.1029/2010JC006899.

Yu, X, AC Naveira Garabato, AP Martin, CE Buckingham, L Brannigan, and Z Su (2019). "An Annual Cycle of Submesoscale Vertical Flow and Restratification in the Upper Ocean". In: *Journal of Physical Oceanography* 2019.

Zhou, M, Y Zhu, RD Dorland, and CI Measures (2010). "Dynamics of the current system in the southern Drake Passage". In: *Deep Sea Research Part I: Oceanographic Research Papers* 57.9, pp. 1039–1048.